OPTICAL FIBER SENSING WITH DEEP LEARNING FOR BIOMEDICAL APPLICATION

CHEN SHUYANG

PhD

The Hong Kong Polytechnic University

2022

The Hong Kong Polytechnic University

Department of Electronic and Information Engineering

Optical fiber sensing with deep learning for biomedical application

Chen Shuyang

A thesis submitted in partial fulfillment of the requirements for the degree of Doctor of Philosophy

June 2022

Certificate of Originality

I hereby declare that this thesis is my own work and that, to the best of my knowledge and belief, it reproduces no material previously published or written, nor material that has been accepted for the award of any other degree or diploma, except where due acknowledgment has been made in the text.

.....(Signed)

CHEN Shuyang (Name of student)

Abstract

In the modern aging society, health care has been a major concern among people. Ballistocardiography (BCG) is a vibration signal related to cardiac activity, which can be obtained in a non-invasive way by optical fiber sensors. In this work, an optical fiber interferometer-based BCG monitoring system has been developed. Several deep learning models are explored to optimize this monitoring system.

Firstly, a BCG monitoring system based on the optical fiber sensor is proposed. A moving-coil transducer-based new phase modulation method is developed to address the signal fading problem in the optical fiber interferometer, which can keep the output of the system in quadrature by a closed-loop controller. As a result, a BCG signal without baseline drift can be obtained. This optical fiber interferometer-based BCG monitoring system offers the benefits of being tiny, low-cost, portable, and user-friendly.

Secondly, we study the individual heartbeat waveform detection algorithm based on BCG signals. A convolutional neural network (CNN) is first built to classify the IJK-complex, background, and body movement signals. Since this CNN model needs a series of time-consuming pre-processing works, we propose an end-to-end modified U-net to improve the individual heartbeat waveform detection algorithm. This network has demonstrated its capacity to segment the IJK complex and body movement in the BCG signal with great accuracy.

Then, a modified generative adversarial network (GAN) is presented to reconstruct BCG signals in an optical fiber interferometer with the intensity interrogation mode. This method eliminates the need for extra modulators and

demodulators in the interferometer, lowering costs and simplifying the hardware. The results show that the algorithm can reconstruct the BCG signal successfully. To further test the model performance, we have analyzed the reconstruction results based on the collected data on sinus arrhythmia and post-exercise cardiac activities. In conclusion, this signal reconstruction algorithm simplifies the BCG monitoring system by solving the signal fading problem in the optical fiber interferometer in a novel way.

Finally, a compressed sensing (CS) framework is built for the BCG signal based on the optical fiber sensing system. Four types of CS reconstruction algorithms, Basis Pursuit (BP), orthogonal matching pursuit (OMP), and two block sparse Bayesian learning (BSBL) algorithms are used to verify the reconstruction performance in BCG signals under different CRs. The performance of two BSBL algorithms outperforms the other two algorithms. Traditional reconstruction algorithms perform poorly when CR is greater than 90%. Therefore, an end-to-end deep learning model is developed to reconstruct BCG. The performance of the model is good when CR increases from 50% to 90%. For the high CR over 90%, though the performance is slightly degraded, the IJK complex in the BCG can be recovered, and the MAE of the HR is low than 1 bpm when the CR is below 95%.

Acknowledgments

At this point, I realize that I am practically done with my Ph.D. study. I have a long list of persons to whom I wish to express my heartfelt gratitude. First and foremost, I would like to express my gratitude to Prof. YU Changyuan, my supervisor. He gave me the opportunity to study at Hong Kong Polytechnic University and invited me to participate in his research group. He has been big assistance to me in my study and life during the exceptional and challenging COVID-19 era. Prof. YU, as a good mentor and friend, has taught me a lot, not only in terms of professional knowledge and abilities but also in terms of research zeal and rigor. I am lucky and glad to be able to work under Prof. YU's guidance.

Furthermore, at PolyU, I have made a lot of good friends who have helped me a lot with my Ph.D. study and daily life. Without them, I wouldn't be able to complete my research as efficiently as I would like. I want to express my gratitude to Dr. Tan Fengze, who was really helpful to me at the start of my Ph.D. study. I want to thank Dr. WANG Biwei, Dr. WANG Zhuo, Dr. YUAN Weihao, Mr. LUO Huaijian, Mr. Abdullah Al Noman, Mr. YANG Zongru, Miss. QU Jiaqi, Mr. LIU Yifan, Mr. LYU Weimin, Mr. LIU Zhongxu, Mr. Li Yujian, Mr. CHEN Jiajian, Mr. YU Jianxun, Mr. ZHOU Jing, Mr. CHENG Zhi, Mr. CUI Mingjie, Dr. HUANG Zhuili, Dr. XUE Min, and Dr. ZHOU Ji.

Finally, I want to thank my parents. They give me great help and encouragement in my life and study. I would not be able to finish my Ph.D. without their entire support.

June 2022

Publications

Journal:

1. ***S. Chen***, F. Tan, W. Lyu, H. Luo, J. Yu, J. Qu, and Yu, C, "Deep learning-based ballistocardiography reconstruction algorithm on the optical fiber sensor," Opt. Express, 30(8), 13121-13133 (2022).
2. ***S. Chen***, F. Tan, W. Lyu, and C. Yu, "Ballistocardiography monitoring system based on optical fiber interferometer aided with heartbeat segmentation algorithm," Biomed. Opt. Express, 11(10), 5458-5469, (2020).
3. ***S. Chen***, W. Lyu, J. Yu, H. Luo, J. Qu, and Yu, C, "Compressed sensing framework for ballistocardiography monitoring based on the optical sensor," (Submitted to Biomedical Optics Express).
4. W. Lyu, ***S. Chen***, F. Tan, and C. Yu, "Vital Signs Monitoring Based on Interferometric Fiber Optic Sensors," Photonics, 9(2), 50 (2022).
5. W. Lyu, W. Xu, F. Yang, ***S. Chen***, F. Tan, and C. Yu, "Non-invasive Measurement for Cardiac Variations Using a Fiber Optic Sensor", IEEE Photon. Technol. Lett. 33(18), 990-993, (2021).
6. F. Tan, W. Lyu, ***S. Chen***, Z. Liu, and C. Yu, "Non-invasive human vital signs monitoring based on twin-core optical fiber sensors," Opto-Electron. Adv. 3(5), 190034, (2020).
7. F. Tan, ***S. Chen***, W. Lyu, Z. Liu, C. Yu, C. Lu, and H. Y. Tam, "Non-invasive human vital signs monitoring based on twin-core optical fiber sensors," Biomed. Opt. Express, 10(11), 5940-5952 (2019).

Conference paper:

1. **S. Chen**, F. Tan, W. Lyu, and C. Yu, "Ballistocardiography reconstruction based on optical fiber sensor using deep learning algorithm," in 2021 Opto-Electronics and Communications Conference (OECC), 1-3 (2021).
2. **S. Chen**, F. Tan, W. Lyu, and C. Yu, "A ballistocardiography monitor based on optical fiber interferometer," in 2020 Photonics Asia, 1-6 (2020).
3. **S. Chen**, Z. Huang, F. Tan, T. Yang, J. Tu, and C. Yu, "Non-invasive smart monitoring system based on multi-core fiber optic interferometers," in Asia Communications and Photonics Conference and Exhibition (ACP) 2018, 1-3 (2018) (**Best Poster Award**).
4. **S. Chen**, Z. Huang, F. Tan, T. Yang, J. Tu, and C. Yu, "Vital signs monitoring using Few-mode fiber-based sensors," in Photonics Asia 2018, 1-7 (2018).
5. W. Lyu, **S. Chen**, F. Tan, and C. Yu, "Non-invasive heart rate variability measurement during sleep based on fiber optic sensor," in Opto-Electronics and Communications Conference (OECC) 2021, Paper JS3F. 2 (2021).
6. J. Zhang, Y. He, F. Tan, **S. Chen**, W. Lyu, F. Yang, and C. Yu, "IJK complex detection within BCG signal based on multicore fiber sensors," in Asia Communications and Photonics Conference and Exhibition (ACP) 2020, 1-3 (2020).
7. F. Yang, W. Lyu, C. Pan, S. Yang, F. Tan, **S. Chen**, and C. Yu, "Contactless vital signs monitoring based on optical fiber Mach-Zehnder interferometer aided with passive homodyne demodulation methods," in Asia

Communications and Photonics Conference and Exhibition (ACP) 2020, 1-3 (2020).

8. C. Yu, F. Tan, **S. Chen**, W. Lyu, X. Zhu, and J. Luo, "Bionic palpation based on optical fiber sensor," in Optoelectronic Global Conference (OGC) 2020, 1 (2020) (**Invited**).
9. W. Lyu, F. Tan, **S. Chen**, and C. Yu, "Myocardial contractility assessment using fiber optic sensors," in Asia Communications and Photonics Conference and Exhibition (ACP) 2019, 1-3 (2019).
10. C. Yu, F. Tan, Z. Liu, **S. Chen**, and Z. Huang, "Application of seven core fiber-based sensor on torsion angle measurement and vital signs monitoring," in International Conference on Transparent Optical Networks (ICTON) 2019, 1-4 (2019). (**Invited**).
11. F. Tan, Z. Liu, **S. Chen**, and C. Yu, "Vital signs monitoring using twin core fiber-based sensor", in Opto-Electronics and Communications Conference (OECC) 2019, 1-3 (2019).

Content

Certificate of Originality III

Abstract IV

Acknowledgments VI

Publications VII

Content X

List of Abbreviations XIV

List of Figures XIX

List of Tables XXIII

Chapter 1 1

1.1 Overview and research motivations 1

1.2 Ballistocardiography 5

1.2.1 Overview 5

1.2.2 Measurement methods 7

1.3 Optical fibers and optical fiber sensors 9

1.3.1 Optical fibers 9

1.3.2 Optical fiber sensors 12

1.4 Deep learning models 15

1.4.1 Overview 15

1.4.2 Multilayer perceptron 16

1.4.3 Convolutional neural network 19

1.4.4 Recurrent neural network..... 22

1.5 The application of deep learning in the 1-D biomedical signal.....24

1.6 Research objectives 27

1.7 Organization of the thesis.....28

Chapter 2 31

2.1 Introduction 31

2.2 Optical fiber interferometers-based BCG monitoring.....32

2.3 Traditional phase interrogation schemes 39

2.4 An MZI-based BCG monitor with phase compensation system 42

2.4.1 Experiment setup 42

2.4.2 Phase shifter based on moving-coil transducer 45

2.4.3 Compensation method 46

2.4.3 Result and discussion..... 49

2.5 Summary 51

Chapter 3 53

3.1 Introduction 53

3.2 Heartbeat detection based on convolutional neural network.....55

3.2.1 Method..... 55

3.2.2 Result and discussion..... 58

3.3 End-to-end heartbeat detection algorithm based on U-net 59

3.3.1 Method 59

3.3.2 Evaluation metrics 62

3.3.3 Result and discussion 63

3.5 Summary 66

Chapter 4 67

4.1 Introduction 67

4.2 Principle 69

4.3 Modified algorithm 72

4.4 Experiment setup and evaluation methods 75

4.5 Result and discussion 78

4.6 Special cases 84

4.7 Summary 87

Chapter 5 88

5.1 Introduction 88

5.2 Compressed sensing 90

5.2.1 Principle 90

5.2.2 Sparse representation 93

5.2.3 Measurement matrices 94

5.2.4 Reconstruction algorithms 96

5.3 Performance evaluation of traditional reconstruction algorithms in BCG signals 99

5.3.1 Method 99

5.3.1 Evaluation method 101

5.3.2 Result and discussion 101

5.4 Deep learning model-based reconstruction algorithms for BCG reconstruction with a high CR 104

5.4.1 Method 104

5.4.2 Result and discussion 106

5.5 Summary 110

Chapter 6 111

6.1 Conclusion 111

6.2 Future works 114

Bibliography 116

List of Abbreviations

B	
BCG	Ballistocardiography
BP	Basis pursuit
BSBL	Block sparse Bayesian learning
BR	Breath rate
BSBL-BO	BSBL based on bound-optimization method
BSBL-EM	BSBL based on expectation-maximization method
BSBL-FM	BSBL based on fast marginalized likelihood maximization method
BSBL-l1	BSBL based on group-lasso type algorithms
C	
CRC	Cardiorespiratory coupling
CVDs	Cardiovascular diseases
CH1	Channel 1
CH2	Channel 2
CR	Compressed ratio
CS	Compressed sensing
cGAN	Conditional generative adversarial network
CV	Control variable
CNN	Convolutional neural network
C-point	Critical point

D

DAQ card	Data acquisition card
DBN	Deep belief network
DCGAN	Deep convolutional generative adversarial network
DGMs	Deep generative models
DCM	Differential cross multiplication
DC	Direct current
DCT	Discrete cosine transform
D	Discriminator
DFB laser	Distributed feedback laser

E

EDR	ECG-derived respiration
ECG	Electrocardiography
EMFi	Electromechanical film
EMG	Electromyography
EOG	Electro-oculogram
ELM	Extreme learning machine

F

FPI	Fabry-Perot interferometer
FMF	Few-mode fibers
FB	Fiber Bragg grating
FMCW	Frequency modulated continuous wave
FCL	Fully connected layer

G

GAN	Generative adversarial network
G	Generator

H

HRV	Heart rate variability
HR	Heartbeat rate

I

IBI	Inter-beat interval
IoMT	Internet of medical thing
IoT	Internet of thing

L

LED	Light-emitting diode
LPF	Low-pass filter

M

MZI	Mach-Zehnder interferometer
MRI	Magnetic resonance imaging
MP	Matching pursuit
MCP	McCulloch–Pitts
MAE	Mean absolute error
MIOU	Mean intersection over union
MPA	Mean pixel accuracy
MSE	Mean squared error
MI	Michelson interferometer
MCF	Multi-core fibers

MLP	Multi-layer perceptron
MMF	Multi-mode fiber
N	
NREM	Non-rapid eye movement
O	
OMP	Orthogonal matching pursuit
P	
PCC	Pearson correlation coefficient
PRD	Percent root mean square difference
PG	Phase generated carrier
PD	Photodetector
PPG	Photoplethysmography
PZT	Piezoelectric transducer-based
pix2pix	GAN pix2pix generative adversarial network
PA	Pixel accuracy
PMF	Polarization maintaining fiber
PSG	Polysomnogram
PV	Process variable
PID	Proportional-integral-derivative
Q	
Q-point	Quadrature point
R	
REM	Rapid eye movement
RNN	Recurrent neural network

ResNet	Residual Network
RSA	Respiratory sinus arrhythmia signal
RBM	Restricted Boltzmann machine
S	
SP	Set point
SCF	Seven-core fiber
SNR	Signal-to-noise ratio
SMF	Single-mode fiber
SVM	Support vector machine
V	
VCSEL	Vertical-cavity surface-emitting laser

List of Figures

Fig. 1.1. A BCG waveform. 7

Fig. 1.2. The cross section (a) and the corresponding index profile (b) of a single-mode fiber. 11

Fig. 1.3. (a) Fiber-optic displacement sensor. (b) Micro-bend fiber-optic sensor. (c) Liquid level detector. 13

Fig. 1.4. (a) Temperature probe used in black body-based optical fiber sensor. (b) FBG sensors. 14

Fig. 1.5. (a) Fiber-optic Michelson interferometer. (b) Fiber-optic Mach-Zehnder interferometer. (c) Fiber-optic Fabry-Perot interferometer. (d) Microcavity. 15

Fig. 1.6. The architecture of multilayer neural network. 18

Fig. 1.7. The structure of a CNN. 20

Fig. 1.8. The calculation rule of convolution. 21

Fig. 1.9. The calculation rules of max pooling and average pooling. 21

Fig. 1.10. The structures of an RNN. 23

Fig. 1.11. The structure of a typical RNN cell. 24

Fig. 2.1. Vital signs signals detected by optical fiber interferometers: (a) raw signal; (b) extracted heartbeat signal; (c) extracted respiration signal. 34

Fig. 2.2. The structure of optical fiber MZI. 35

Fig. 2.3. The structure of optical fiber MI. 35

Fig. 2.4. The structure of optical fiber SI based on PMF. 36

Fig. 2.5. The mode field distributions of (a) LP_{01}, (b) LP_{11}, (c) LP_{21} and (d) LP_{02}. 38

Fig. 2.6. The mode field distributions of (a) MMF and (b) SCF. 39
Fig. 2.7. The structure of an MZI based on 3×3 coupler interrogation scheme.....40
Fig. 2.8. The structure of an MZI based on the PGC demodulation method. 42
Fig. 2.9. The BCG monitoring system. 43
Fig. 2.10. (a) Integrated MZI with a transducer. (b) Sketch of the moving-coil transducer. 46
Fig. 2.11. The relationship between resultant output cosine signal in the MZI (a) and driven current (b). 46
Fig. 2.12. (a) Principle of the closed-loop control system with PID controller. (b) Variation of optical intensity toward driven current. (c) Electrical signals in the time domain. 47
Fig. 2.13. Raw data of BCG signals. 50
Fig. 2.14. Raw BCG signal from 7 subjects. 51
Fig. 3.1. A BCG segment. 53
Fig. 3.2. The architecture of a proposed CNN. 56
Fig. 3.3 A detailed BCG signal segment (a) and training samples of IJK complex segment (b), background segment (c) and body movement segment (d). 57
Fig. 3.4. The workflow of the heartbeat detection algorithm based on CNN. 59
Fig. 3.5. BCG data with the prediction from CNN: (a) BCG signal of subject 1. (b) BCG signal of subject 2. (c) BCG signal with sinus arrhythmia from subject 3. (d) BCG signal with the noise of system reset from subject 3. 59
Fig. 3.6. The architecture of modified U-net. nf is the number of filters in 1-D convolution layer. 61
Fig. 3.7. A BCG segment (a) with corresponding label (b). 62

Fig. 3.8. (a) Confusion matrix of test set. (b) The scatterplot of predicted versus actual I-K interval. 64
Fig. 3.9. BCG segmentation results based on modified U-net: (a) BCG signal with HR of 82 bpm; (b) BCG signal with HR of 67 bpm; (c) BCG signal with HR of 97 bpm; (d) BCG signal with occasional sinus arrhythmia; (e) BCG signal with body movement. 65
Fig. 4.1. The optical systems of (a) the BCG monitor and (b) the reference BCG monitor with a phase compensation system. (c) The overview of the reconstruction method. 71
Fig. 4.2. (a) Training process of GAN. (b) Architecture of the BCG reconstruction algorithm. 74
Fig. 4.3. The experiment setup. 76
Fig. 4.4. I, J, K waves in the BCG signal. 78
Fig. 4.5. (a) Scatterplot of reconstructed J'-J' intervals versus reference J-J intervals. (b) Box plot of absolute errors of time delay between I, J, K waves and I', J', K' waves. 81
Fig. 4.6. Reconstructed BCG waveforms with different operating points in (a) to (d). 82
Fig. 4.7. Reconstructed BCG waveforms with poor quality of raw signals..... 83
Fig. 4.8. Reconstructed BCG waveforms with different HRs: (a) HR is 97 bpm and (b) HR is 66 bpm. 83
Fig. 4.9. Reconstructed BCG, reference BCG, and ECG segments with sinus arrhythmia. 85

Fig. 4.10. The reconstructed post-exercise BCG segments during 3 minutes. (b) The post-exercise IBI variation of BCG and ECG during 5 minutes. 86
Fig. 5.1. Measurement matrices with CR of 50% and 80%. 99
Fig. 5.2. The workflow of CS. 100
Fig. 5.3. The average (a) PRD, (b) PCC, and (c) MSE based on four types of reconstruction algorithms under different CRs. 102
Fig. 5.4. Reconstruction results by (a) BP and (b) OMP under CR of 80%. 103
Fig. 5.5. Reconstruction results by (a) BSBL-BO and (b) BSBL-FM under CR of 80%. 104
Fig. 5.6. Reconstruction results by (a) BSBL-BO and (b) BSBL-FM under CR of 93%. 104
Fig. 5.7. The architecture of the CS reconstruction algorithm. 106
Fig. 5.8. The average PRD, PCC, and MSE in the test data by three types of reconstruction algorithms under different CRs. 107
Fig. 5.9. The reconstruction results of deep learning model under different CRs: (a) 91%, (b) 92%, (c) 93%, (d) 94%, (e) 95%, and (f) 96%. 109

List of Tables

Table. 4.1. Mean PCC, PRD, bx, and MAE in the test set with the combination of different numbers of blocks in G and D networks. 80

Table. 5.1. The average PRD, PCC, and MSE of reconstruction results in the test set using the deep learning model with the CR exceeding 90%. 108

Table. 5.2. The average PRD, PCC, and MSE of reconstruction results in the test set using BSBL-BO and BSBL-FM with the CR exceeding 90%. 108

Table. 5.3. The MAE of HR in the test data with CR increasing from 91% to 96%. 110

Chapter 1

Introduction

1.1 Overview and research motivations

In the modern aging society, health care has always been a major concern, especially in some developed countries. Vital signs, such as respiration, heartbeat, temperature, blood pressure, and blood glucose, are the main health indications of the human body. Vital signs monitoring can help to assess the health condition of the human body, which is significant in many healthcare applications. Due to rising concerns about health problems, researchers are interested in the development of user-friendly and convenient vital signs monitoring methods. Among them, heartbeat monitoring is particularly important as cardiovascular diseases (CVDs) have become the leading death cause among various fatal diseases in the world [1]. For heartbeat monitoring, long-term service is essential no matter in the clinic or at home.

Electrocardiography (ECG) and photoplethysmography (PPG) are the mainstream methods to detect heartbeat signals. ECG signal is the record of the electrical activity of the heart pumping blood, and it has been widely accepted as the main method to diagnose CVDs. During ECG monitoring,

multiple electrodes are required to attach to specific positions of the body, and each pair of electrodes is called the lead. The 12-lead ECG is widely used in clinics [2]. Other than ECG, PPG is the biological signal measured via the optic method, which can obtain the plethysmography of organs by placing a pulse oximeter on the finger [3]. PPG signal is based on the blood flow change and thus can be collected from the variation in the intensity of transmitted light (or reflected light) on the skin. Both PPG and ECG signal collections require skin contact, and they are developed as wearable devices. The wearable devices will inevitably discomfort the users, especially for heartbeat monitoring in the long-term way. For long-term heartbeat monitoring, non-invasive and non-wearable heartbeat monitors will be preferred and may become popular in near future. Therefore, various new technologies have been investigated in the field of vital signs monitoring to replace traditional measurements.

Ballistocardiography (BCG) is a biomedical signal reflecting the body recoils in reaction to heart ejection during each cardiac cycle, in which the body recoils refer to global movements of the body. It is a combination of multiple forces including blood flow within the heart, blood flow within arteries (mainly the aorta), and heart movement. BCG signals can be detected in a non-invasive and non-wearable way [4]. Many research groups have explored various sensing schemes to track the BCG waveform. Among them, electronic sensors are the most common type adopted to fabricate the BCG monitor. O. T. Inan et al. developed a standing heartbeat monitoring based on a modified bathroom scale in 2009 [5]. Users could obtain their

ballistocardiography (BCG) signal by standing on the scale and keeping still. In addition, J. Alametsa et al. proposed a sitting position heartbeat monitor that utilized an electromechanical film (EMFi) sensor [6]. They embedded the EMFi sensor into the cushion and users could obtain the heartbeat signal when they sat on the cushion. More than that, M. Liu et al. demonstrated a heartbeat monitor based on a low-power piezoelectric film sensor, which could track the BCG signal in both sitting and standing positions [7]. In addition, remote vital signs monitoring based on video or radar technologies has also caused a lot of concern in recent years. M. A. Hassan et al. developed a remote health monitoring system through a video-based signal processing method. They obtained the approximative BCG signals by estimating the microscopic color change or rigid motion in the face [8]. O. Postolache et al. proposed to utilize 24GHz microwave FMCW (frequency modulated continuous wave) Doppler radar to monitor radar ballistocardiography of people [9]. Though these technologies provide feasible schemes to monitor heartbeat or breath, some drawbacks will greatly reduce the performance of sensors. For example, the limited sensitivity could result in the loss of details in biomedical signals, and electromagnetic interference can also affect performance. In addition, for video or radar technologies-based remote health monitoring, motion artifacts will introduce large errors into the monitoring systems.

Optical fiber-based sensors as a novel sensing technology own many merits including low cost, high sensitivity, electrical isolation, and immune to electromagnetic interference, which is intrinsically safe and reliable.

Optical fiber-based sensing technologies have been widely used in strain [10], temperature [11], acceleration [12], and refractive index [13] measurements. In addition, there are several vital signs monitors based on different types of optical fiber sensors. For example, X. Yang et al. built a wearable textile fiber optic micro-bend sensor to monitor heartbeat and respiration according to the principle of micro-bend loss [14]. Ł. Dziuda et al. developed a fiber Bragg grating (FBG) strain sensor to acquire the heartbeat and respiration signals of the user during the magnetic resonance imaging (MRI) survey [15]. However, mentioned optical fiber sensor-based technologies have some defects: the sensitivity of the micro-bend loss-based sensing method is limited and the demodulation technology of FBG is expensive. To address these problems, our group focuses on phase-based optical fiber sensors.

For optical fiber interferometers, the signal fading effect makes the sensor unsuitable for long-term monitoring. Although numerous modulation and demodulation technologies, including 3x3 coupler-based signal demodulation [16] and piezoelectric transducer-based (PZT) phase modulation [17], can be used to solve the signal fading problem, they have significant limitations for BCG monitoring. Piezoelectric cylinders, for example, are large and cannot be integrated into a compact BCG monitoring system. The first task of this thesis is to solve this problem and obtain long-term, real-time and stable BCG signals.

Deep learning algorithms have advanced quickly in recent years and are now widely used in a variety of fields. Many academics have used deep learning algorithms to solve both image and sequence signal issues in

biomedical applications in recent years. For 1-D biomedical signals, such as ECG, electroencephalogram (EEG), electromyography (EMG), and electrooculogram (EOG), several topics have drawn great attention and been widely investigated, including detection of cardiovascular diseases [18], classification of sleep stages [19], and analysis of mental stress [20]. Since the BCG signals can be interfered and distorted easily by the motion artifact and ambient noise during the measurement, deep learning models are suitable to solve various issues in the BCG-related signal processing tasks, such as individual heartbeat detection, heart rate (HR) calculations, and CVDs detection. The second tasks of this thesis are to explore the application of deep learning models in the BCG signals.

In general, the research motivations of this thesis are to study the BCG monitoring system based on optical fiber interferometers and solve the signal fading problem. At the same time, this thesis is aimed to explore the possibility of using deep learning to optimize monitoring systems. This long-term and real-time BCG monitoring system has tremendous potential in future healthcare applications.

1.2 Ballistocardiography

1.2.1 Overview

BCG is the measurement of body recoils produced by heart ejection during every cardiac cycle, which can be used to monitor cardiac activities in an unobtrusive way. The BCG signal was firstly observed by Gordon in 1877 [21], and Isaac Starr et al. developed an instrument to measure this signal in

a scientific manner in 1939 [22]. However, due to some limitations on measurement methods, the BCG-related technology was not developed further and was gradually replaced by ECG. Nowadays, BCG regains the spotlight with evolved sensing techniques and signal processing methods.

The blood travels along the vascular tree with each heartbeat, which causes changes in the body's center of mass. Then, body micromovements caused by recoil forces can maintain the overall momentum. BCG is a recording of these movements, and it can be obtained as a displacement, velocity, or acceleration signal. BCG can be divided into longitudinal and transverse BCG depending on the movements in different axes. The longitudinal BCG represents the head-to-foot vibration of the body while the transverse BCG is the dorso-ventral direction. The longitudinal BCG is the largest projection of 3-D forces caused by cardiac ejection. In particular, for some measurement ways, the head-to-foot and dorsoventral forces are mixed unavoidably. Though BCG owns a 3-D nature, only the longitudinal BCG was investigated by researchers for a long time in past. The main measurements of longitudinal BCGs were based on the force sensor placed on a weighing scale or a chair, and thus the subject could be in a vertical position to detect the change of head-to-foot force. Subsequently, lots of bed-based sensors were widely studied to detect transverse BCG successfully.

BCG waveform is generated with each cardiac contraction, and each waveform owns several peaks and valleys. As shown in Fig. 1.1, a completed BCG signal is composed of multiple peaks including H, I, J, K, and L peaks, and these peaks have corresponding physiological significance. For instance,

the amplitude of the major wave J peak, or IJK complex, is related to the aortic pulse pressure [23]. BCG can be used to calculate the HR and heart rate variability (HRV) of the subject, which has great potential in cardiac health care.

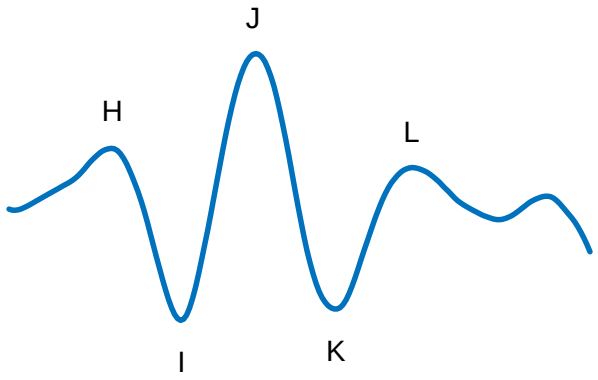

Fig. 1.1. A BCG waveform.

1.2.2 Measurement methods

There are three methods to detect BCG signals, which can be divided into weighing-scale-based BCG systems, bed-based BCG systems, and chair-based BCG systems.

The weighing-scale-based BCG system was first proposed by Jim Williams in 1990, which was based on an electronic scale [24]. Williams built a high-precision electronic scale (4.5 g resolution up to 136 kg) and then found the motion artifacts during the measuring process, which is mainly composed of the BCG signal. The standing posture of the subject in the weighing-scale-based BCG system guarantees the measurement is purely longitudinal, which is the main advantage of this type of measurement. Moreover, since weighing scales are a common household device, it is easy

to popularize this heartbeat monitoring system by enhancing the capabilities of the traditional weighing scale. Therefore, many researchers have investigated this BCG measurement. O. T. Inan et al. proposed a standing BCG monitor based on a modified commercial bathroom scale in 2009 [5]. The obtained BCG recording matched well with the synchronously measured Doppler echocardiography. Gonzalez-Landaeta et al. [25] and Shin et al [26] have also successfully built BCG monitors based on weighing scales. In all studies, the BCG signals have a similar shape and amplitude to the traditional recordings detected by Starr et al. At the same time, however, this kind of measurement also exists the issue of being susceptible to motion artifacts and floor vibrations. In addition, the weighing-scale-based BCG system also limits the duration of the measurement since it is uncomfortable for the subject to stand still on the scale for a long time, especially for a patient.

Bed-based BCG systems can access the BCG signals during sleep, which can be used in the evaluation of sleep stages and sleep-related disorders. Since the BCG devices do not need to attach electrodes to the skin of subjects, they will not disturb the sleep behaviors of subjects compared to ECGs during the data collection stage. Bed-based BCG systems can be integrated with the sleeping environment based on different types of sensors. For example, Alihanka et al. proposed a static charge-sensitive bed in 1981, which was the first time such a bed-based BCG sensor has been proposed [27]. Subsequently, film-type force sensors [28], EMFi sensors [29], piezoelectric film sensors [30], polyvinylidene fluoride sensors [31], and hydraulic sensors [32] have been proposed to detect BCG on the bed. In addition, sensor arrays have been

developed to replace the single sensor to improve performance [33]. These sensors can not only detect heartbeat signals, but also other physiological information such as respiration signals and body movements, which can be used to improve the accuracy of sleep analysis.

Chair-based BCG systems can obtain the BCG in the sitting position. Walter et al. proposed an EMFi sensors-based BCG monitor embedded in the driver's seat in the car, which could be used to monitor the fitness of the driver [34]. J. Alametsa et al. also built a sitting position monitor based on an EMFi sensor to measure BCG signals and demonstrated its better performance than acceleration sensors [35]. In general, chair-based BCG monitors provide a heartbeat monitoring way during the day, and they can work with bed-based BCG monitors to realize a sound cardiac health monitoring system in daily life. However, chair-based BCG signals own less signal amplitude compared to bed-based BCG and weighing-scale-based BCG signals, which need more sensitive sensors to detect.

1.3 Optical fibers and optical fiber sensors

1.3.1 Optical fibers

Optical fibers were firstly invented by K. C. Kao in 1966, which is a dielectric waveguide operating in the optical band [36]. The refractive index of the fiber core is higher than its surrounding region in a dielectric fiber, which enables the transmission of energies at optical frequencies to travel in optical fibers according to the total internal reflection phenomenon. Optical fibers have

been extensively studied since then, and single-mode fibers (SMFs) have been produced for use in practical communication systems.

An optical fiber consists of core, cladding, and jacket. The cylindrical core of silica glass is surrounded by the cladding, in which the refractive index of the core is slightly larger than that of the cladding. According to the variation of refractive index, there are two types of optical fibers: step-index fibers and graded-index fibers. Step-index fibers have an abrupt refractive index change at the core-cladding interface while the refractive index of the core reduces gradually and then is equal to that of the cladding at the interface in graded-index fibers. The cross section and the corresponding index profile of a step-index SMF are shown in Fig. 1.2, where a and b are radii of the core and the cladding, and n_1 and n_2 are the refractive indexes of the core and the cladding. Generally, a and b are 8 μm and 125 μm in the SMF. Other than the common SMF, several structures of optical fibers are designed and fabricated based on various requirements, such as few-mode fibers (FMFs) [37], multi-mode fibers (MMFs) [38], multi-core fibers (MCFs) [39], and photonic crystal fibers [40].

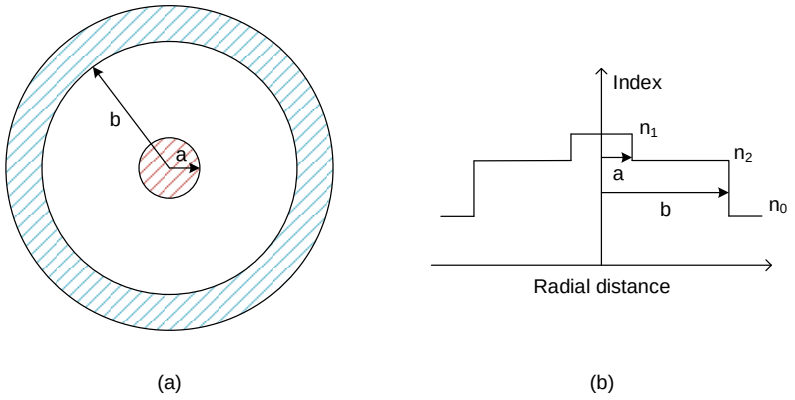

Fig. 1.2. The cross section (a) and the corresponding index profile (b) of a single-mode fiber.

Optical fibers have been widely used in communications due to the intrinsic merits of long transmission distance, large information capacity, lightweight, immune to electromagnetic interference, and safety. In recent years, optical fibers have also been investigated and utilized in the application of sensing. Optical fiber sensors have been demonstrated to be available for strain, temperature, acceleration, and refractive index sensing. The principle of optical fiber sensors is that the light from a laser or light-emitting diode (LED) propagates through the optical fiber and interacts with measured parameters in the sensing area. The optical properties of light, such as optical intensity, wavelength, frequency, phase, and polarization state, will be changed. The formed modulated signal can be delivered to the demodulation system to obtain the measured parameter. At present, fiber optic sensors have been widely used in the field of structure health monitoring [41], well logging technology [42], and medical applications [43]. Furthermore, a fiber-optic sensor can be utilized in many extreme conditions, such as high temperature [44] and intensity magnetic field [45], owing to its remarkable properties of which.

As mentioned, variational measured parameters can change the optical properties of light. Therefore, there are several types of optical sensors based on different principles including intensity-based, wavelength-based, and phase-based, which will be introduced briefly in the following part.

1.3.2 Optical fiber sensors

For intensity-based optical fiber sensors, the optical intensity will change with the measured parameter, and variation of the transformed electrical signal from the photodetector (PD) is related to the measured parameter. There are several types of intensity-based sensors. The first type is based on the transmission/reflection light. The example shown in Fig. 1.3(a) is a fiber-optic displacement sensor [46] based on transmission light. The light intensity can change with the lateral displacement between the sensing arm and the reference arm. The second type is utilizing the principle of bending loss. Figure. 1.3(b) is a micro-bend fiber-optic sensor [47]. Cyclic bending of optical fiber resulting from comb deformer with fixed spatial period can convert part of guided modes to radiation modes, which changes the light intensity. The third type is based on the varying refraction index. Figure. 1.3(c) is a liquid-level detector [48] using an optical fiber and a prism. When the probe enters the liquid, the light intensity can change with the variational critical angle. The device is used to detect the refractive index of the liquid.

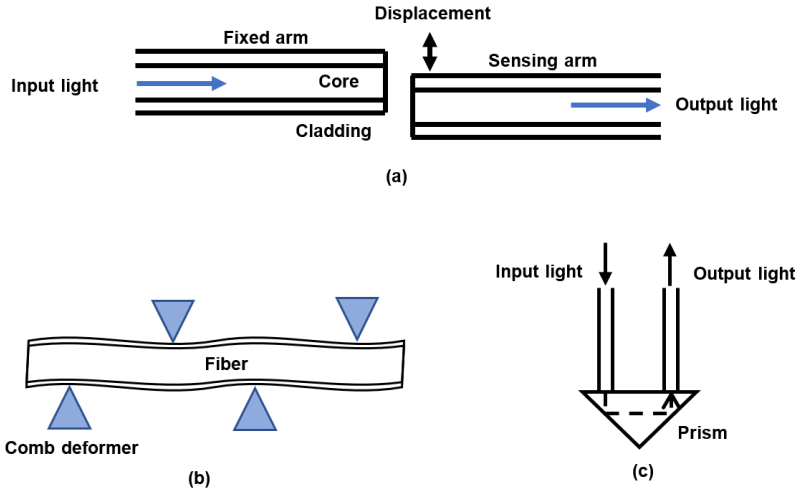

Fig. 1.3. (a) Fiber-optic displacement sensor. (b) Micro-bend fiber-optic sensor. (c) Liquid level detector.

For wavelength-based optical fiber sensors, the spectrum can be modulated by the measured parameters. An optical fiber-based sensor based on the black body radiation principle can realize high-temperature measurements [49]. As shown in Fig. 1.4(a), the temperature probe, the black body cavity, is fabricated by covering a thin metal film on the sapphire fiber. The optical radiation spectrum of the black body cavity can change at different temperatures. Another example is an FBG sensor [50]. FBG distributed sensors are widely utilized in structure health monitoring, which can monitor the internal strain in a long range. The structure of FBG is fabricated by etching a grating pattern in the core of the optical fiber, as shown in Fig. 1.4(b). The measurement principle of the FBG sensor is that a certain wavelength will be reflected by the fiber grating according to the grating period Λ. The value Λ can change with measured parameters, such as strain and temperature.

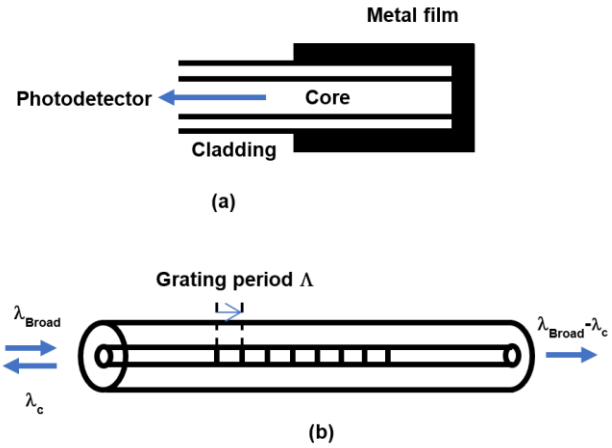

Fig. 1.4. (a) Temperature probe used in black body-based optical fiber sensor. (b) FBG sensors.

For phase-based optical fiber sensors, phase variation cannot be obtained directly by PD. Therefore, interferometers are utilized to convert phase change into optical intensity variation. There are several typical types of interferometers. The first one is a fiber-optic Michelson interferometer (MI) [51], as shown in Fig. 1.5(a). There are two reflective mirrors placed at the end of the sensing and reference arm, respectively. The phase of sensing light can change with measured parameters. Two reflected light form interference at the coupler and the varying light beam can propagate back to PD. The second type is a fiber-optic Mach-Zehnder interferometer (MZI) [52], as shown in Fig. 1.5(b). The light beam is split into two paths by the first coupler, which work as sensing and reference arms, respectively. Similarly, the modulated sensing light and reference light are coupled at the second coupler, and the interference light can be obtained by PD. The third type is a fiber-optic Fabry-Perot interferometer (FPI) [53], which is shown in Fig. 1.5(c). A microcavity is fabricated by coating two high reflection films in the fiber, as shown in Fig. 1.5(d), and then multiple reflective lights generate interference

in the optical fiber. The length of microcavity changes with the measured parameter and the variational light intensity can be obtained in the PD.

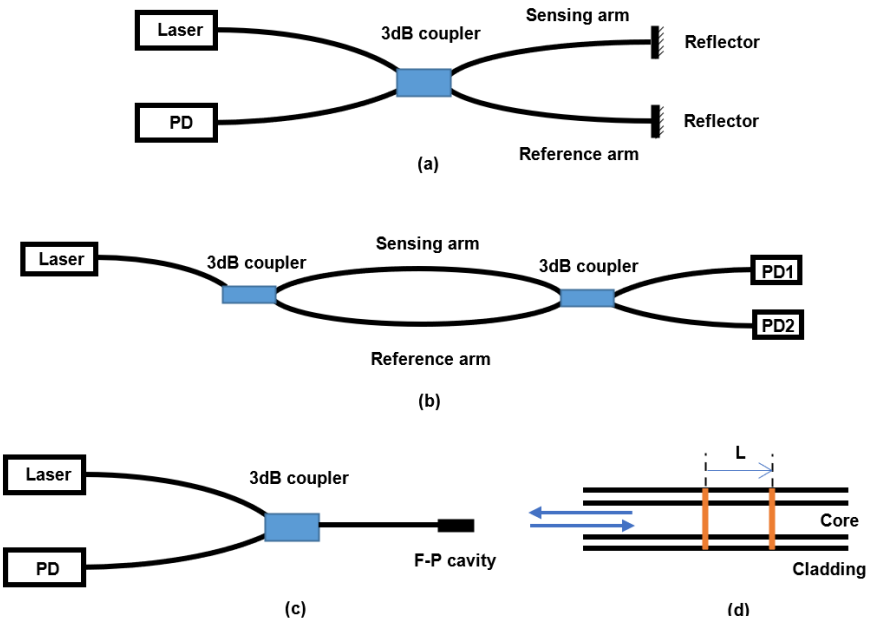

Fig. 1.5. (a) Fiber-optic Michelson interferometer. (b) Fiber-optic Mach-Zehnder interferometer. (c) Fiber-optic Fabry-Perot interferometer. (d) Microcavity.

1.4 Deep learning models

1.4.1 Overview

Deep learning is an extension type of neural network that has two or more hidden layers. Many applications of deep learning have proven to be successful, such as image and speech recognition. McCulloch and Pitts presented the McCulloch–Pitts (MCP) neuron, which is the first artificial neuron model in 1943 [54]. At the time, researchers aimed to use computers to imitate the response process of human neurons. Rosenblatt built a perceptron using the MCP neuron in 1958, which was the first application of artificial neurons in machine learning [55]. The perceptron could divide

multidimensional input samples into two classes and update the weights using a gradient descent approach. In 1962, the approach was shown to be convergent, and the good performance drew a lot of attention from researchers. However, in 1969, Minsky demonstrated that the perceptron is a linear model that can only be used to solve linear classification problems. As a result, the neural network has remained unchanged for nearly two decades.

Hinton developed a multi-layer perceptron (MLP) in 1986 that performed nonlinear mapping using the Sigmoid activation function rather than hard thresholding [56]. This approach was able to solve the nonlinear classification problem, which has received a lot of attention again. However, the vanishing gradient problem was discovered in the backpropagation algorithm adopted in the MLP in 1991. The issue is that during backpropagation, the gradient may become tiny, preventing the weight from changing its value. In 2006, Hinton used a restricted Boltzmann machine (RBM) to create a deep belief network (DBN) to solve the vanishing gradient problem [57]. Subsequently, the ReLU activation function was developed in 2011 to replace the Sigmoid activation function, which can also address the problem of vanishing and explosive gradients [58]. Hinton and his team participated in the ImageNet in 2012 to demonstrate the potency of deep learning, and the convolutional neural network (CNN), AlexNet, proposed by them won the first prize [59]. Deep learning drew a lot of interest from researchers after that.

1.4.2 Multilayer perceptron

The MLP is a feedforward fully connected network including multiple artificial neural networks. An MLP consists of several layers, including an input layer, several hidden layers, and an output layer, the architecture of which is shown in Fig. 1.6. The layer refers to one column of neurons in the network. The input layer serves as a distribution point, and hence there is no input summation. Except for the input layer, the output of a neuron is the sum of neurons from the previous layer. As a result, each neuron has only one output, which is connected to the next layer as an input to create a fully connected network. The output of neuron *i* in layer *l* is shown as

$$a_i(l) = h\big(z_i(l)\big), \tag{1.1}$$

$$z_i(l) = \sum_{j=1}^{n_{l-1}} w_{ij}(l)a_j(l-1) + b_i(l), \tag{1.2}$$

where $i = 1, 2, \ldots, n_l$, and n_l is the number of neurons in layer l. $j = 1, 2, \ldots, n_{l-1}$, and n_{l-1} is the number of neurons in layer $l-1$. a_i and a_j are the output of neuron i in layer l and neuron j in layer $l-1$ passing through the activation function, respectively. w_{ij} are the weights between neuron i in layer l and neuron j in layer $l-1$, and b_i is the bias of neuron i in layer l. h is the activation function of neuron i in layer l. The class of the input vector is determined by the output layer values, which can be determined by

$$a_i(L) = h_L\big(z_i(L)\big), \tag{1.3}$$

where i = 1, 2, 3, …, n_L, and n_L is the number of neurons in the output layer. h_L is the activation function of the output layer, such as Sigmoid for the binary classification and SoftMax for multi-class classification.

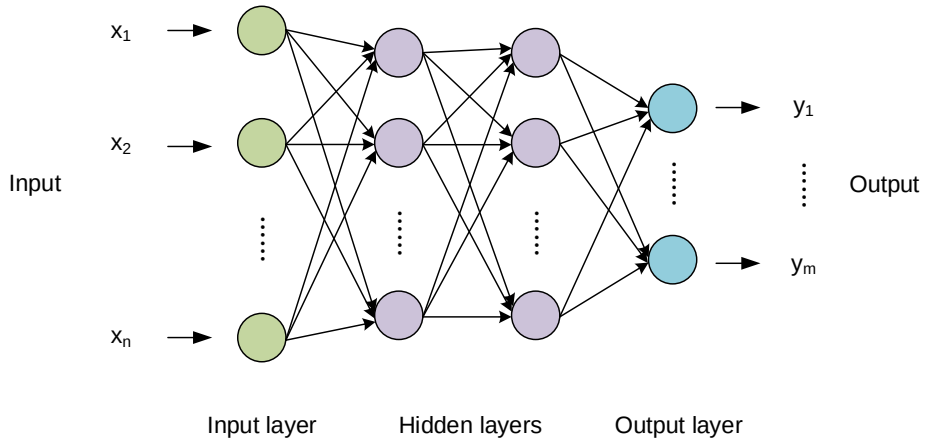

Fig. 1.6. The architecture of multilayer neural network.

The weights, biases, and activation function of a neural network characterize it completely. To minimize the error, the network is trained using labeled training samples and the loss function. The sum of squared error can be used to calculate the error of neuron j in the output layer, which is given by

$$E_j = \frac{1}{2}\left(r_j - a_j(L)\right)^2, \tag{1.4}$$

where $j = 1, 2, 3, \ldots, n_L$, and $r_j = 1$ if the input is of class j. $a_j(L)$ is the output of neuron j. The output error is the sum of errors from all output neurons, which can be calculated using

$$E = \sum_{j=1}^{n_L} E_j \,. \tag{1.5}$$

The total network output error of all training samples can be obtained by the sum of errors from each sample. The backpropagation and gradient descent algorithms are adopted to minimize total error and update the weights and biases. First, the sensitivity of neuron j in the output layer is defined as

$$\delta_j(L) = \frac{\partial E}{\partial z_j(L)}. \tag{1.6}$$

The backpropagation begins from the output layer and works backward. In hidden layer *l*, the sensitivity of neuron *j* is given by

$$\delta_j(l) = \frac{\partial E}{\partial z_j(l)}. \tag{1.7}$$

After expressing the above two equations, we can get two equations shown as

$$\delta_j(L) = h_L\left(z_j(L)\right)\left[1 - h_L\left(z_j(L)\right)\right]\left[a_j(L) - r_j\right], \tag{1.8}$$

$$\delta_j(l) = h'\left(z_j(l)\right)\sum_i w_{ij}(l+1)\delta_i(l+1). \tag{1.9}$$

Finally, $\frac{\partial E}{\partial w_{ij}(l)}$ and $\frac{\partial E}{\partial b_i(l)}$ are obtained by $\delta_j(l) = \frac{\partial E}{\partial z_j(l)}$. Weights and biases are updated by gradient descent, and they can be given by

$$w_{ij}(l) = w_{ij}(l) - \alpha\delta_i(l)a_j(l-1), \tag{1.10}$$

$$b_i(l) = b_i(l) - \alpha b_i(l), \tag{1.11}$$

where l = L-1, L-2, L-3, …, 2. a_j is the result computed in the forward propagation and δ_i is obtained during the backpropagation.

1.4.3 Convolutional neural network

As mentioned, the MLP adopts the full connection strategy, which treats all the inputs equally. However, this fully connected network ignores the local features of images. For a real image, nearby pixels have a stronger correlation than distant pixels. In addition, the full connection produces a large number of parameters, which is easy to lead to overfitting. Therefore, a CNN with the properties of local connection and weight sharing was proposed by LeCun et

al. in 1989, which was used for handwritten digit recognition [60]. In 1998. LeCun et al. have proposed LeNet-5, which is one of the most simplified and commonly used CNN architectures [61]. Currently, CNN is widely applied in the field of computer vision and achieves great success.

The structure of a typical CNN is shown in Fig. 1.7, which is a 7-layer convolutional network. During the training phase, the filter moves over the picture in a fixed stride to calculate the convolution. The convolution is computed as the sum of the products of the kernel weights and the pixels in the receptive field, the calculation rule of which is shown in Fig. 1.8. Each convolution result has a bias applied to it before passing through the activation function. As a consequence, convolution can extract features from the input picture such as edges, points, and blobs, which are then stored in feature maps. A convolutional layer is made up of various kernels that can create diverse feature maps.

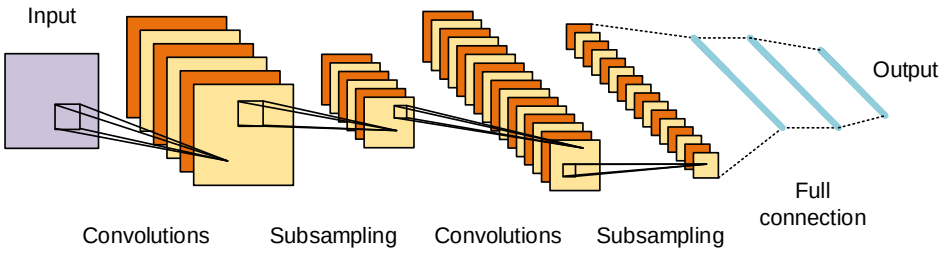

Fig. 1.7. The structure of a CNN.

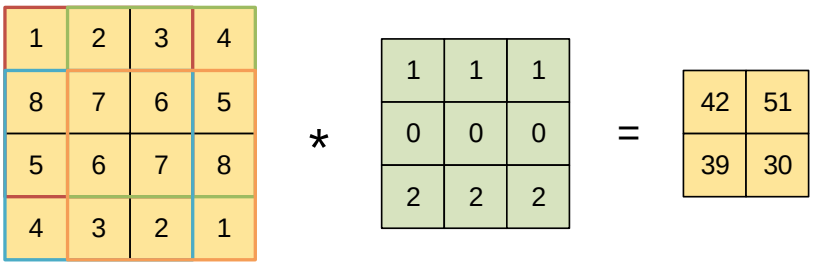

Fig. 1.8. The calculation rule of convolution.

The spatial resolution of feature maps will be decreased by a pooling layer after going through the convolution layer. Max pooling and average pooling are two typical pooling methods. In Fig. 1.9, the calculation rules for max pooling and average pooling are given, with max pooling producing the highest value of the receptive field and average pooling producing the mean value. The pooling layer is a significant part of the feature extraction. The pooling layer can suppress noise, and reduce the dimension together with information redundancy. In addition, it can also realize the translation invariance, rotation invariance, and scale invariance for the input data.

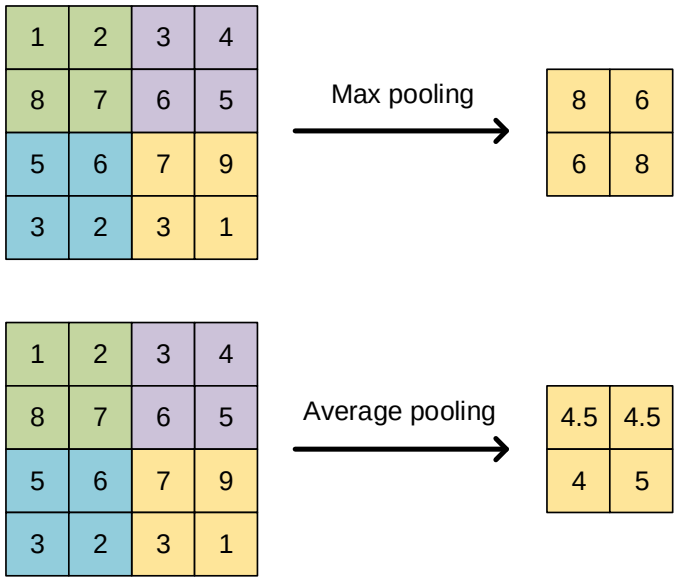

Fig. 1.9. The calculation rules of max pooling and average pooling.

In the second convolutional layer, different kernels are applied to each pooled feature map and then subsampled by the second pooling layer. The 2-D feature maps are flattened and connected with a fully connected layer (FCL). Finally, the output layer gives predicted results, and the model can be trained by the backpropagation strategy.

1.4.4 Recurrent neural network

The recurrent neural network (RNN) is a temporal sequence model, which can exhibit temporal dynamic behavior. RNNs have been widely used in the field of speech recognition [62], machine translation [63], and video activity [64]. The structures of an RNN are shown in Fig. 1.10, which are a compressed type (left) and an unfolded type (right), respectively. The sequence sample $x_1, x_2, x_3, \dots, x_{T_x}$ with the length of T_x can be fed into the network in a timed sequence. Compared to the MLP, the RNN has a hidden state a_t, which is also referred as a hidden variable. a_t stores the sequence information before time step t. Therefore, the hidden state at time step $t+1$, a_{t+1}, can be calculated based on the current input x_{t+1} and the previous hidden state a_t, which can be defined as

$$a_{t+1} = f(x_{t+1}, a_t). \tag{1.12}$$

It is noteworthy that hidden states in RNN are different from hidden layers in the MLP. The hidden state a_t can store the previous sequence information, which is crucial for the prediction of the next output.

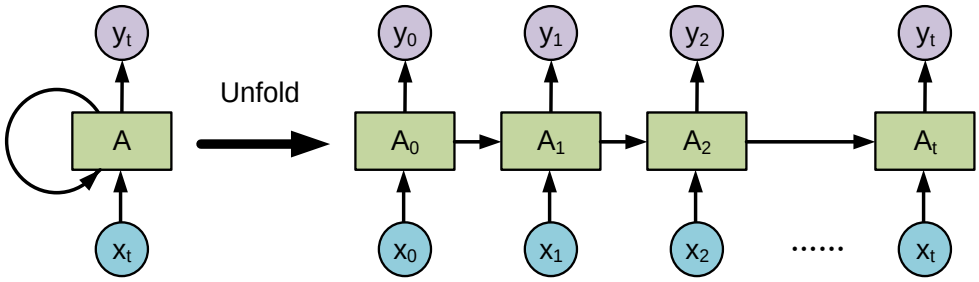

Fig. 1.10. The structures of an RNN.

The structure of a neuron in a typical RNN is shown in Fig. 1.11. In a forward propagation process, the hidden state at time step t, $a^{\langle t \rangle}$, will update first, which can be defined as

$$a^{\langle t \rangle} = h_a\left(W_{aa} \cdot a^{\langle t-1 \rangle} + W_{ax} \cdot x^{\langle t \rangle} + b_a\right). \tag{1.13}$$

where W_{aa} and W_{ax} are weights related to the previous hidden state $a^{\langle t-1 \rangle}$ and the current input $x^{\langle t \rangle}$. h_a is the activation function of the hidden state, in which tanh and ReLU are common choices. b_a is the bias. Then, the output at time step t, $y^{\langle t \rangle}$, can be expressed as

$$y^{\langle t \rangle} = h_y\left(W_{ya} \cdot a^{\langle t \rangle} + b_y\right). \tag{1.14}$$

where W_{ya} and b_y are the weight and the bias relevant to the output. h_y is the activation function, which is determined by the task type, such as SoftMax for the multi-classification task. Finally, the RNN can be updated based on the backpropagation through time.

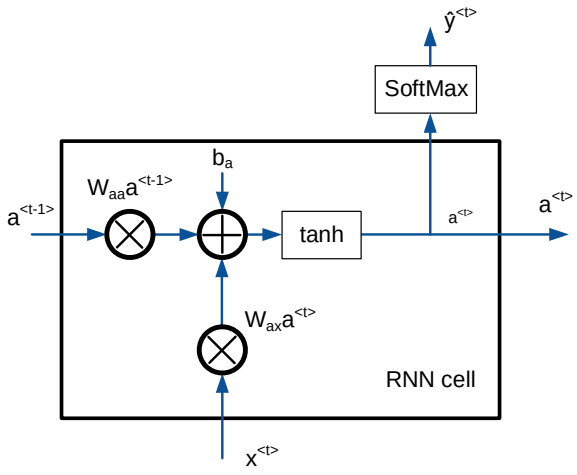

Fig. 1.11. The structure of a typical RNN cell.

1.5 The application of deep learning in the 1-D biomedical signal

In recent years, many researchers have applied deep learning algorithms to solve various issues in the biomedical field. For 1-D biomedical signals, such as ECG, EEG, EMG, and EOG, several topics have attracted great attention, including detection of cardiovascular diseases, classification of sleep stages, and analysis of mental stress, which are introduced in the following.

1. Detection of cardiovascular diseases

CVDs have been the leading death cause among various fatal diseases around the world. Every year, around 300 million ECGs are used to identify various types of CVDs. CVDs are usually diagnosed by a medical expert according to the ECGs of patients. Recently, a variety of deep learning models have been adopted and investigated to realize automatic CVDs detection in the ECG.

Hannun et al. suggested a cardiologist-level arrhythmia classification system based on the residual network (ResNet), which consists of 33

convolutional neural networks [65]. They gathered almost 90,000 ECG recordings from 53,549 individuals, which is 500 times more than the prior research. The network can classify 10 different forms of arrhythmias, sinus rhythm, and noise, with 12 outputs in total. In addition, Xu et al. proposed an end-to-end ECG classification system based on the deep learning model, in which the input is raw ECG data and the output is beat-by-beat classification decisions [66]. The new preprocessing methods involving heartbeat segmentation and alignment are innovative and vital to improving performance. The model can learn the features from both time-domain ECG signals and R-peak positions of each heartbeat and realizes the end-to-end prediction.

2. Classification of sleeping stages

Sleep disorder is a symptom of various neurological diseases, which is common among people and may affect the quality of daily life. Sleep stages classification is a typical method to help detect neurological disorders accurately, which has been widely investigated. The sleep stage consists of three classes, including wake, rapid eye movement (REM) sleep, and non-rapid eye movement (NREM) sleep. Among them, NREM can be further divided into three sub-stages, including stage N1, stage N2, and stage N3.

Polysomnogram (PSG) is a traditional method to access the sleep stages, which is conducted by attaching several sensors to the body in a laboratory environment [67]. PSG contains a series of vital sign recordings, such as EEG, ECG, EMG, and EOG. However, PSG is time-consuming, onerous, costly, and also needs manual scoring. Many researchers are devoted to classifying

the sleep stage based on a deep learning model using fewer channels of vital signs recording. For example, Yildirim et al. proposed a 19-layer CNN to classify the sleep stage based on the EEG and EOG [68]. It is noteworthy that the model owns the end-to-end complete architecture, which combines the extraction/selection and classification stages. The results show that the model can achieve the classification accuracies for two to six sleep classes as 98.06%, 94.64%, 92.36%, 91.22%, and 91.00%, respectively.

In addition, many studies are focused on classifying the sleep stage based on the ECG and respiratory, since the ECG signal is easier to access compared to other recordings. For example, Li et al. proposed a CNN model and a support vector machine (SVM) to classify sleep stages based on ECG signals [69]. First, ECG-derived respiration (EDR) signals and HRV time series are extracted from ECG through robust algorithms. In the following, the coherence and cross-spectrogram of EDR and HRV signals are calculated in a 5-min window, which is the cardiopulmonary coupling (CPC). Finally, the CNN model can be trained to classify the sleep stages including wake, REM sleep, NREM light sleep, and NREM deep sleep from the corresponding CPC spectrograms, and the SVM is adopted to combine the above features and give a final decision of sleep stages.

3. Analysis of mental stress

In recent years, besides physical health, mental health has been considered a matter of concern. EEG is a kind of small-size, low-cost and high temporal resolution signal containing several hundred channels, which is widely used in the study of brain disorders such as depression. In addition,

EEG is also a common method to evaluate mental stress. Recently, deep learning models have been adopted to analyze mental health based on EEG.

Acharya et al. used a CNN to analyze the EEG signals of depressed and normal subjects [70]. Through the study, they found that the EEG signals from the right hemisphere of the brain are more distinctive than that of the left hemisphere for depression detection. It provides some evidence that depression is related to the hyperactivity of the right hemisphere. Mohan et al. used an MLP to distinguish the EEG of depressed patients from normal subjects [71]. The results show that the performance of the model is better when the signals from central regions (electrodes C3 and C4) are used as input. Zhang et al. proposed a concatenated structure of RNN and 3D CNN to learn the spatial-spectral-temporal features of EEG. Among them, 3D CNN is used to obtain spatial and spectral representations while RNN is adopted to extract the temporal characteristics. The network outperforms the traditional machine learning model based on hand-crafted features in the task of mental workload assessment.

1.6 Research objectives

The research objectives of this study are to develop the cardiac health monitoring system based on the optical fiber sensor and investigate the application of deep learning algorithms in the BCG signal processing and the optimization of sensing systems, which can be summarized as follows:

- To fabricate a long-term and real-time BCG monitoring system based on the optical fiber interferometer. To solve the signal fading problem

that affects the signal quality greatly in the optical fiber interferometer through phase compensation methods.

- To develop an individual heartbeat detection algorithm based on the deep learning model. To solve the issue about extraction of the individual heartbeat from dirty BCG signals, such as body movements signals
- To solve the signal fading problem based on the mapping model, in which the hardware of phase modulation and demodulation is replaced by a reconstruction algorithm based on the deep learning model.
- To develop a compressed sensing framework for BCG monitoring based on the optical sensor, which can be applied to the practical cardiac health monitoring scenario.

1.7 Organization of the thesis

The research contributions of this thesis are composed of 6 chapters.

Chapter 1 gives an overview of this thesis first. Then four sections BCG, optical fiber sensors, deep learning, and its applications are introduced detailly, respectively. In section 1.2, the types and waveform features of BCG are described first, followed by the different measurement methods. Section 1.3 reviews the common types of optical fiber sensors including the intensity-based, wavelength-based, and phase-based optical fiber sensors. Sections 1.4 and 1.5 introduce the theories of the MLP, the CNN, and the RNN, and also

the application of deep learning in the 1-D biomedical signal. Finally, the research objectives and organization of this thesis are presented.

Chapter 2 introduces a novel BCG monitor based on an optical fiber interferometer. The problem of signal fading in the intensity interrogation mode-based optical fiber interferometers is described first. And then, the traditional phase modulation and demodulation schemes including the 3×3 coupler interrogation scheme and the phase generated carrier interrogation scheme followed by drawbacks of these interrogation methods are presented. Subsequently, a novel phase compensation method based on a moving-coil transducer is presented. Details about the working principle of the moving-coil transducer, and the compensation strategy of the proportional-integral-derivative (PID) controller are shown. Finally, the performances of BCG monitoring toward several subjects with different HRs are presented.

Chapter 3 presents two individual heartbeat detection algorithms based on deep learning algorithms. First, a heartbeat detection algorithm based on a 10-weight-layers CNN is proposed. To further improve the algorithm, an end-to-end heartbeat detection algorithm based on U-net is developed. The detailed parameters of the network are described, and the performance of the model is evaluated by three metrics. BCG signals from several subjects together with body movement signals are analyzed based on the proposed end-to-end heartbeat detection algorithm.

Chapter 4 introduces a BCG reconstruction algorithm based on the generative adversarial network (GAN) in the optical fiber interferometer. A brief overview of the background and the GAN is presented first, followed by

the principle of the proposed mapping method. Then, the experiment setup and the process of data collection are presented. The structure of the modified GAN together with the evaluation metrics are described. Parameters in the model are optimized and the reconstruction results of BCG signals with different deformed degrees are analyzed. Finally, two special cases including sinus arrhythmia data and post-exercise data are adopted to further test the model.

Chapter 5 is related to a CS framework for BCG monitoring based on the optical fiber sensor, which can be applied in the practical healthcare scenario. The principle of CS and three crucial parts including the sparse representation, measurement matrices, and reconstruction algorithms are introduced. Subsequently, several traditional reconstruction algorithms including basis pursuit (BP), orthogonal matching pursuit (OMP), and block sparse Bayesian learning (BSBL) algorithms are used to verify the reconstruction performance in the BCG signals under different compression ratios (CR). Finally, a deep learning-based reconstruction algorithm is proposed to reconstruct BCG under the high CR (over 90%).

Chapter 6 gives a summary of works in this thesis and possible suggestions for the following work. Two future directions for the application of deep learning models in BCG monitoring and BCG signal processing are presented, including a new mapping model to reconstruct BCG signals, a combined algorithm of CS and phase demodulation, and sleep stages classification based on BCG signals.

Chapter 2

Ballistocardiography monitoring based on an optical fiber interferometer with phase compensation system

2.1 Introduction

In recent years, various BCG detection methods have been proposed, as mentioned in section 1.2. Most BCG detection approaches are based on electronic sensing technologies, which own the intrinsic disadvantages of low sensitivity and incapability for some applications, such as vital signs monitoring in the MRI. Therefore, new sensing schemes are investigated to detect BCG signals.

Optical fiber sensors-based vital signs monitors have attracted much attention among researchers due to their intrinsic merits such as high sensitivity, immunity to electromagnetic interference, and low cost. For example, an FBG strain sensor was proposed to acquire BCG and respiration signals of patients during the MRI survey and the high accuracy was proved by the Bland-Altman analysis [45]. A micro-bend optical fiber sensor was demonstrated to measure breath rate (BR), HR, and BCG waveform [72]. However, the demodulation devices of FBG sensors are bulky and quite

expensive, which is not suitable for practical applications. The sensitivity of micro bending-based sensors is limited, which may lose the BCG details.

To overcome these drawbacks, our group adopts the phase-sensitive optical fiber interferometer schemes, and several vital signs monitors have been demonstrated [73-75]. However, optical fiber interferometers are subject to the signal fading effect, which also makes the sensor unsuitable for long-term monitoring. Although many modulation and demodulation technologies can be utilized to address the signal fading problem, such as 3x3 coupler-based signal demodulation and PZT-based phase modulation, they are also exposed to some limitations for specific BCG monitoring. For example, piezoelectric cylinders are bulky and cannot be integrated into a compact BCG monitoring system.

Therefore, in this chapter, several types of optical fiber interferometers-based vital signs monitoring are introduced first. Subsequently, two kinds of phase demodulation methods adopted in the MZI-based vital signs sensors are demonstrated. In the last part, a BCG monitoring system utilizing a new phase compensation method based on the moving-coil transducer is proposed to realize long-term and stable heartbeat monitoring. The proposed transducer is compact and low-cost, which can be easily integrated into the sensing system without any bulk component. The phase compensation method can keep the interferometric output signal in quadrature by the closed-loop controller and transducer.

2.2 Optical fiber interferometers-based BCG monitoring

For the optical fiber interferometer, any change of phase difference between light through two arms can be transformed into light intensity variation in the output end, which enables the interferometer to detect weak signals. To achieve vital signs measurement in a comfortable way, the optical fiber interferometers are packaged into the mattress and cushion-type sensors for signal monitoring under different positions. When the subject lays or sits on the sensing area, the body recoils resulting from the activity of the heart and lung will introduce a phase shift in the interferometer, which can be transformed into a variation of intensity. Based on this principle, the vital signs signals obtained by optical fiber interferometers are shown in Fig. 2.1(a). The heartbeat and respiration information can be observed in the raw BCG signal. Through signal processing such as filters, the heartbeat and respiration signals can be extracted for further processing and analysis, as shown in Fig. 2.1(b) and Fig. 2.1(c). To achieve vital signs monitoring with high-performance, different types of optical fiber interferometers are investigated, which are shown in the following.

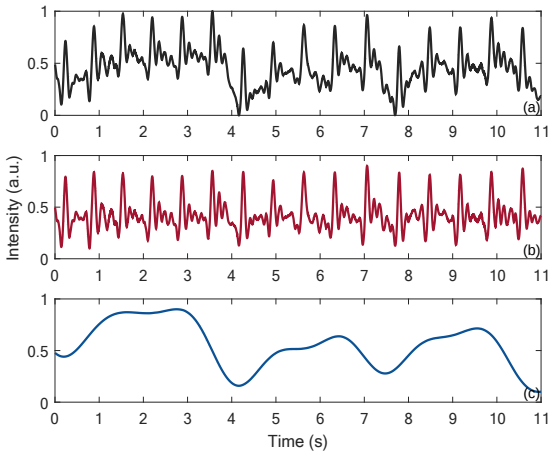

Fig. 2.1. Vital signs signals detected by optical fiber interferometers: (a) raw signal; (b) extracted heartbeat signal; (c) extracted respiration signal.

1. Mach-Zehnder interferometers

An optical fiber MZI is used to fabricate the vital signs monitor by Yu et al. [73]. The MZI can be integrated into a mattress or a cushion for different position measurements such as lying and sitting positions. The optical fiber MZI consists of two 3dB couplers, which are used as the light splitter and coupler, as shown in Fig. 2.2. The incident light from the laser diode is divided into two beams by the lead-in 3dB coupler, and then enters the reference and sensing arms. Since there is a slight difference between the length of two arms, the phase difference is introduced. The two beams recombine and form interference at the lead-out 3dB coupler. The low-speed PD placed at the end of the sensor can convert the variational optical signal into an electrical signal. Thus, the vibration signal derived from the subject sitting or laying on the sensing arm can introduce phase changes in the interferometer and be detected by PD, which is the BCG signal.

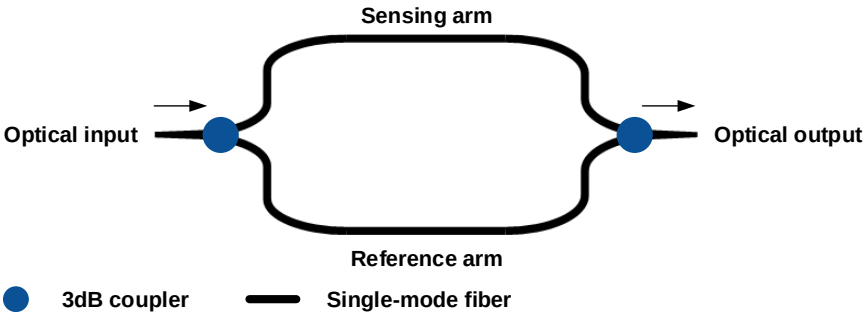

Fig. 2.2. The structure of optical fiber MZI.

2. Michelson interferometers

There are also some studies using MI to fabricate the BCG monitor, such as works from Šprager et al. [76]. The structure of a MI is shown in Fig. 2.3, which contains a 2×2 coupler, two mirrors, and SMFs. The 2×2 coupler in the MI can divide the light from the laser source into two beams and enter the reference and sensing arms, respectively. The two lights will be reflected by the mirror placed at the end faces of two arms, and then coupled by the 2×2 coupler. The interference light can be detected by the PD. Similar to MZI, the phase changes introduced in the MI by BCG signals can be detected.

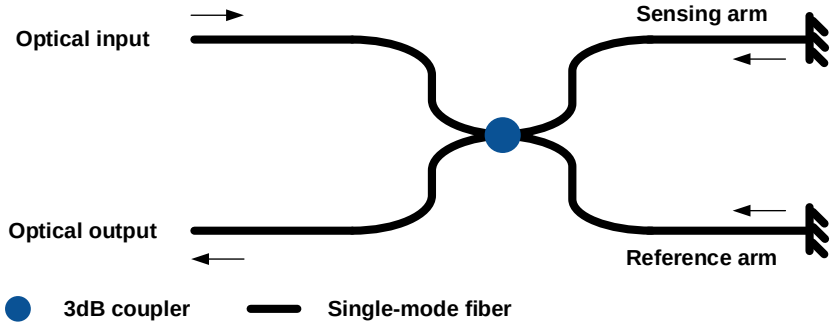

Fig. 2.3. The structure of optical fiber MI.

3. Sagnac interferometer

An optical fiber Sagnac interferometer (SI) is also investigated in vital signs monitoring by Qu et al. [77]. In the experiment, a section of single-mode polarization maintaining fiber (PMF) is inserted in the Sagnac loop, as shown in Fig. 2.4. Due to the specific structure of PMFs such as panda and elliptical-clad types, these fibers own two polarization modes including vertical and horizontal polarization modes. These two modes have slightly different phase velocities and thus the phase difference is introduced. Inside the interferometer, the incident light from the laser diode is split into two counter light beams by the 3dB coupler and propagates in the Sagnac loop. After passing through the PMF, the phase difference of two light beams is formed. Finally, they interfere with each other within the 3dB coupler. According to this principle, the PD placed in the lead-out single-mode fiber can detect the heartbeat and respiration signals from the subject laying on the mattress with a Sagnac loop.

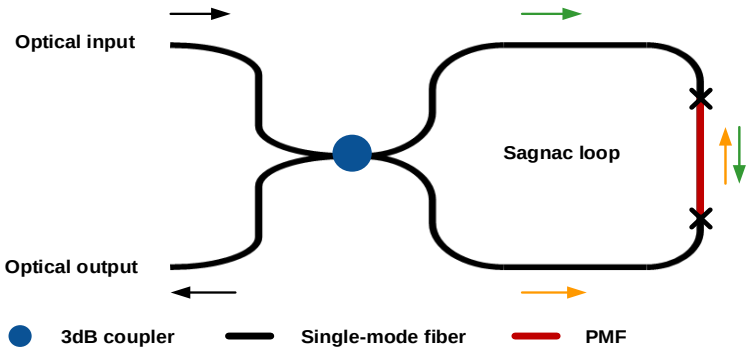

Fig. 2.4. The structure of optical fiber SI based on PMF.

4. In-line interferometer

In recent years, in-line MZI based on modal interference has been widely investigated and developed for the application of sensing due to the compact

structure. Various special optical fibers-based in-line MZIs are also used to detect BCG signals. For example, FMF-based in-line MZIs have been demonstrated for vital signs monitoring, in which two types of FMF, dual-mode fibers and four-mode fibers are adopted. FMF can support a few high-order modes propagating in the fiber and thus the interference can be formed between different modes in the single fiber. The core offset is a common method to excite different modes in the FMF and fabricate the in-line MZI. An SMF-FMF-SMF with a single core-offset structure is adopted to fabricate an in-line MZI-based BCG monitor [78].

Dual-mode fiber is a type of FMF, which can support the first two modes, LP_{01} and LP_{11} modes, in the fiber. Misaligning a fused cross section between lead-in SMF and dual-mode fiber can excite the LP_{11} mode. The excitation ratio of LP_{01} and LP_{11} will change at different core-offset distances. LP_{11} mode will have the highest excitation ratio at a suitable distance, and the excitation ratio of LP_{01} and LP_{11} modes are equal at this distance. LP_{01} and LP_{11} modes will form modal interference and the light can be collected at the second junction between dual-mode fiber and lead-out SMF without another core-offset structure. Four-mode fiber is another kind of FMF that can support the first four modes, LP_{01}, LP_{11}, $LP_{21,}$ and LP_{02} modes in the fiber. The SMF-FMF-SMF structure with an optimized core-offset distance can also excite high order modes and form modal interference in the four-mode fiber. The mode field distributions of LP_{01}, LP_{11}, $LP_{21,}$ and LP_{02} are shown in Fig. 2.5(a) to (d).

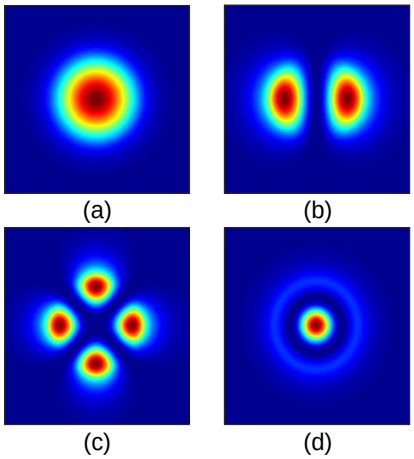

Fig. 2.5. The mode field distributions of (a) LP_{01}, (b) LP_{11}, (c) LP_{21} and (d) LP_{02}.

MCF has several cores arranged in different ways in a single fiber, which aims to improve communication capacity. An in-line MZI based on the seven-core fiber is proposed to monitor BCG signals [79]. To excite seven cores in the fiber, MMF is utilized. The mode field distributions of MMF and seven-core fiber (SCF) are shown in Fig. 2.6(a) and (b). SMF-MMF-SCF-MMF-SMF structure, MSM for short, is adopted to fabricate the in-line MZI. The MMF at the first junction between lead-in SMF and SCF works as a light beam splitter and coupler, which can enlarge the light beam. The propagating light from SMF can be better coupled to seven cores in the SCF. Moreover, the MMF at the second junction between SCF and lead-out SMF is to collect the interference light from SCF. Therefore, each core can be excited, and then lights will form interference in the optical fiber.

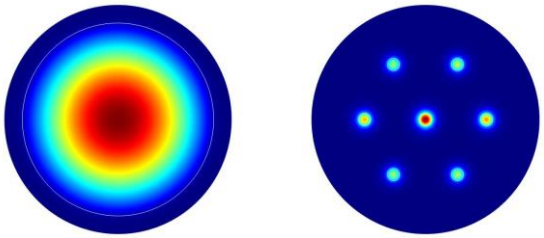

Fig. 2.6. The mode field distributions of (a) MMF and (b) SCF.

2.3 Traditional phase interrogation schemes

Though the optical fiber interferometer owns many merits, the problem of signal fading will also degrade the signal quality, which results in unsatisfied performance in long-term vital signs monitoring. Many demodulation schemes including homodyne and heterodyne methods are applied to address the signal fading problem. However, there are also some limitations on demodulating the vital signs signals from optical fiber interferometers with special structures. Some signal demodulation methods such as the PZT-based phase demodulation cannot be integrated into the compact vital signs monitor due to its bulky size. There are two feasible methods to solve the signal fading problem, which achieve desirable results.

1. 3×3 coupler interrogation scheme

3×3 coupler interrogation scheme is a common method to demodulate the phase information in the interferometer. It can also be used in the interferometer-based BCG monitoring system to reconstruct BCG signals and solve the signal fading problem [80]. The structure of an MZI based on a 3×3 coupler interrogation scheme is shown in Fig. 2.7, in which the system consisted of a distributed feedback laser (DFB laser), an MZI, and three PDs.

In this interrogation scheme, the lead-out coupler has three outputs with a phase difference of 120° between any two PDs, and the output optical intensities from three PDs can be measured as

$$I_1 = D + I_0 \cos\left[\varphi(t) - \frac{2\pi}{3}\right],$$
$$I_2 = D + I_0 \cos[\varphi(t)], \tag{2.1}$$
$$I_3 = D + I_0 \cos\left[\varphi(t) + \frac{2\pi}{3}\right],$$

where $\varphi(t)$ contains the initial phase difference and phase difference variation introduced by vital signs and environmental noise. D and I_0 are constants related to optical intensities. I_1, I_2, and I_3 are the optical intensities of PD1, PD2, and PD3, respectively. Through the differentiate and cross-multiplying demodulation algorithm, $\varphi(t)$ can be extracted.

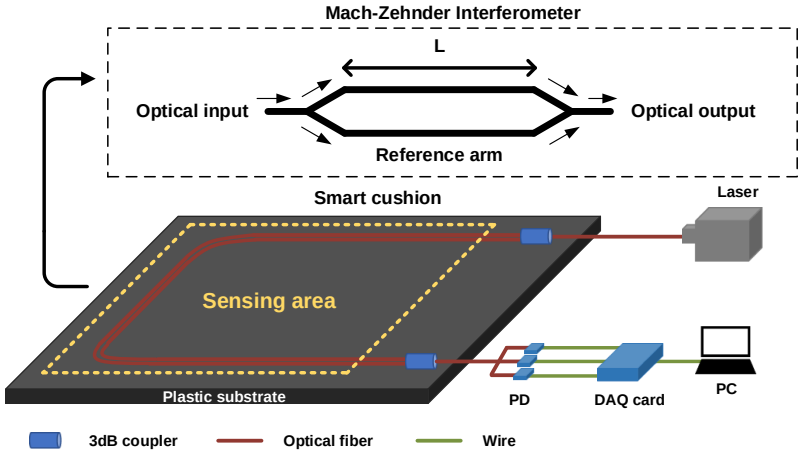

Fig. 2.7. The structure of an MZI based on 3×3 coupler interrogation scheme.

2. Phase generated carrier interrogation scheme

In addition to the 3×3 coupler interrogation scheme, the phase generated carrier (PGC) interrogation scheme is also applied to demodulate the BCG

signal [81]. The PGC interrogation scheme is a widely used passive demodulation method, which owns the merits of high resolution, large dynamic range, and good linearity [82]. In principle, the PGC demodulation method introduces a high-frequency signal in the interferometer and the measurand is modulated to the sideband of the carrier signal. Thus, the measurand can be free from low-frequency noise and then interrogated by the demodulation algorithm such as differential cross multiplication (DCM) and arctangent. There are two modulation methods in the PGC scheme, including internal and external modulation. The internal modulation generates the carrier signal by modulating the frequency of the laser while the external modulation completes it by driving the PZT wrapped with one arm of the interferometer. As the large size of PZT is difficult to be integrated into the cushion or mattress-type sensing system, the internal modulation is adopted in the experiment.

The structure of a PGC demodulation method-based vital signs monitor is shown in Fig. 2.8. The light source is a vertical-cavity surface-emitting laser (VCSEL). The wavelength of this laser can be modulated by driven voltage and thus a high-frequency carrier signal can be introduced in the interferometer. The modulated interference signal detected by PD is described as

$$I = A + B\,cos[C\,cos(\omega_0 t) + \varphi(t)]\,, \tag{2.2}$$

where constant A and B are the direct current component and the mixing efficiency of the interferometer. C and w_0 are the amplitude and frequency of

the modulation signal. $\varphi(t)$ contain the intended signal and phase drift. After signal processing, heartbeat and respiration signals can be obtained.

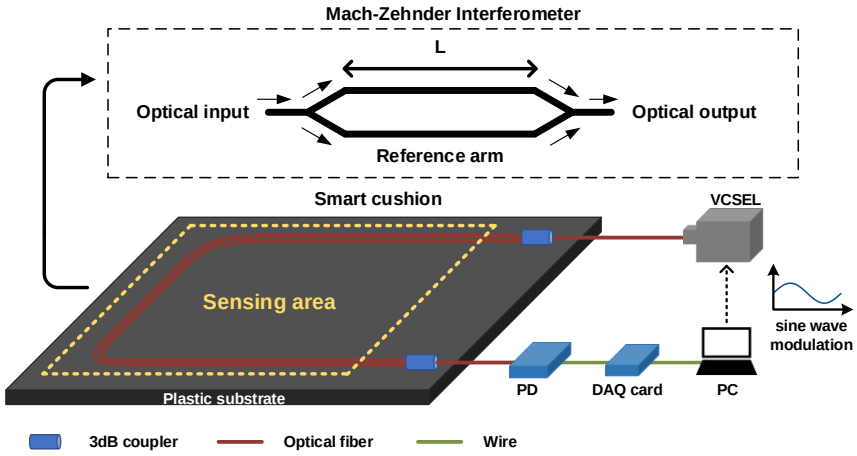

Fig. 2.8. The structure of an MZI based on the PGC demodulation method.

Though these traditional phase interrogation schemes can solve the problem of signal fading in the BCG monitoring system, they greatly increase the cost and complexity of hardware in the system. Therefore, we proposed a new phase compensation method based on the closed-loop system.

2.4 An MZI-based BCG monitor with phase compensation system

2.4.1 Experiment setup

The BCG monitoring system is shown in Fig. 2.9. It consists of the MZI-based BCG monitor, phase shifter, and PID controller, the detailed introduction of which is presented in the subsequent section. The MZI and phase shifter are fixed on a plastic substrate, which can be packaged as a smart cushion to achieve non-invasive BCG monitoring. The sensing area for BCG

signal detection of sitting subjects is highlighted as the yellow dotted box. The light source is a DFB laser operating at 1550 nm while the receiver is a low-speed PD. The arms of MZI, including the sensing arm and reference arm, are fixed in parallel form. The phase shifter is placed outside the sensing area, which is used to maintain the interferometer system in quadrature by a PID controller. The received signal in the PD will be divided into two channels. Channel 1 (CH1) is the raw data and channel 2 (CH2) is obtained results through a low-pass filter (LPF), which will be fed into the PID controller. The controller can compensate for the phase drift to make sure the system works at the quadrature point (Q-point) through the phase shifter. The raw data from CH1 is collected by a data acquisition (DAQ) card (National Instrument, USB6001).

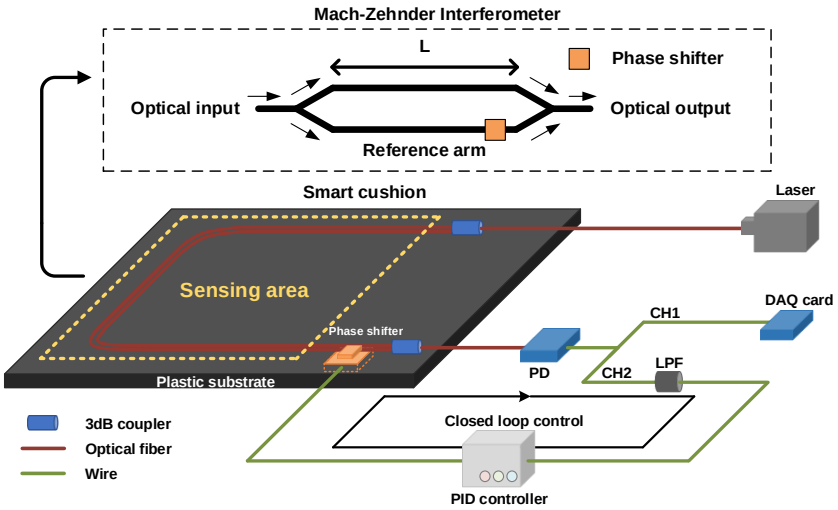

Fig. 2.9. The BCG monitoring system.

The BCG monitor is based on the highly sensitive optical fiber MZI. The optical fiber MZI contains two 3dB couplers, which work as optical splitter and optical coupler to form interference. A PD is used to convert the BCG-

related variational optical intensity signal to the electrical signal. The output optical intensity I can be expressed by

$$I = I_1 + I_2 + 2\sqrt{I_1 I_2}\, cos(\varphi)\,, \tag{2.3}$$

where I_1 and I_2 are output optical intensities from two arms and φ is the optical phase difference within these two arms, which can be given by

$$\varphi = \frac{2\pi n}{\lambda}(L_1 - L_2) = \frac{2\pi n}{\lambda}\delta L, \tag{2.4}$$

where λ is the central wavelength of the laser and n is the refractive index of standard optical fiber. L_1 and L_2 are the lengths of two arms while δL is their length difference. The effective length difference between the sensing and reference arms can be adjusted to improve the sensitivity and dynamic range of the system. In MZI design, the two arms of the interferometer are about 40 cm long and their length difference is 5 mm. These two arms are bent side by side without overlap in a semicircle form and packaged on a plastic substrate integrated into a cushion. When the subject sits on the cushion, the body recoils resulting from heartbeats introducing phase difference in the interferometer, and the corresponding intensity variation can be used for BCG signal extraction.

For MZI, the signal fading effect is a common problem, in which the bias point will shift, and the sensitivity will change accordingly. Finally, it can lead to BCG signal distortion. There are many phase modulation methods to solve this problem, such as active homodyne and passive homodyne. Our proposed phase modulation method is based on the active homodyne method, in which a moving-coil transducer is used as the phase shifter to keep the

system in quadrature ($\varphi = \pi/2$). The phase shifter with a compact size can be easily integrated into the smart cushion without any bulk component.

2.4.2 Phase shifter based on moving-coil transducer

In the BCG monitoring system, we use a compact moving-coil transducer as the phase shifter, the size of which is 18(Length)×12(Width)×3(Height) mm. It is an off-the-shelf component with low cost. Compared with bulky PZT, the moving-coil transducer can be easily integrated into the cushion-type BCG monitor. In addition, unlike the PZT-based method, additional bending loss will not be introduced by the transducer since the optical fiber is directly fixed on the transducer instead of coiling. As shown in Fig. 2.10(a), the transducer is embedded in the plastic substrate and the reference arm of MZI is tightly fixed on the surface of the transducer. Figure. 2.10(b) is the sketch of the moving-coil transducer, in which the coil is placed in the magnetic field. When the driven current changes, a tiny displacement, which is perpendicular to the fixed optical fiber, is introduced by the transducer resulting from the electromagnetic induction, as shown in Fig. 2.10(b). The relationship between the displacement x and driven current *I* can be given by

$$x = \frac{BILN}{k}, \tag{2.5}$$

where *B*, *L*, *N*, and *k* are magnetic field intensity, length of the coil in the magnetic field, number of turns in the coil, and the elastic coefficient of spring, respectively. Therefore, the strain will be introduced in the optical fiber by the tiny displacement derived from the transducer, and thus the phase can be modulated and controlled by the transducer.

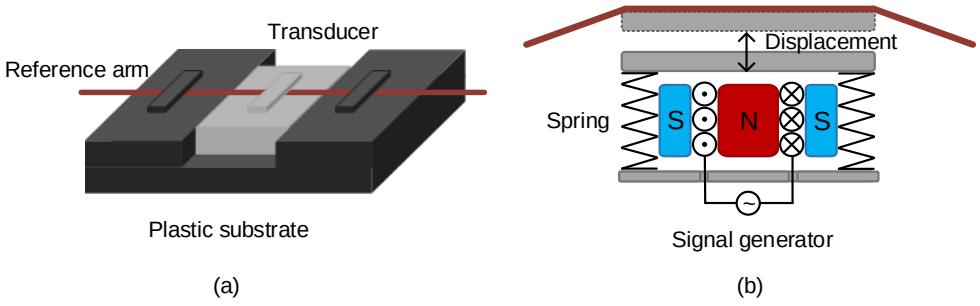

Fig. 2.10. (a) Integrated MZI with a transducer. (b) Sketch of the moving-coil transducer.

The output intensity of MZI presents a cosine waveform with the increasing driven current from -100 mA to 100 mA on the transducer, as shown in Fig. 2.11. Then, the induced phase change under the driven current can be calculated as 0.22 rad/mA. Therefore, by altering the driven current of the transducer, the phase drift will be compensated, and the system can be kept in quadrature.

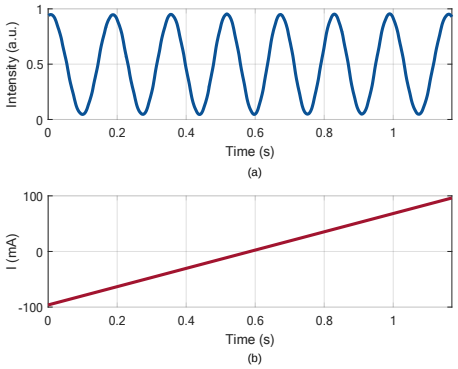

Fig. 2.11. The relationship between resultant output cosine signal in the MZI (a) and driven current (b).

2.4.3 Compensation method

To maintain the MZI system in quadrature, we use a PID controller to control the moving-coil transducer-based phase shifter. The MZI, phase shifter, and PID controller form a closed-loop control system. The PID controller consists

of the proportional, integral, and derivative terms. The detailed principle is described in Fig. 2.12(a). The set point (SP) and process variable (PV) are the desired value and the feedback value, respectively. Error is the difference between SP and PV. Based on the error obtained from the subtractor, the PID controller outputs the control variable (CV) according to the following equation:

$$U(t) = K_P\left(e(t) + \frac{1}{T_I}\int e(t)dt + T_D\frac{de(t)}{dt}\right), \tag{2.6}$$

where $U(t)$ and $e(t)$ represent CV and error at time t, and K_P, T_I and T_D are the coefficients of proportional, integral, and derivative controller [83]. The phase shifter will work to compensate for the phase drift and output PV accordingly, and the PID controller will work after receiving PV and calculate the error to update the CV in the closed-loop control system according to Eq. (2.6).

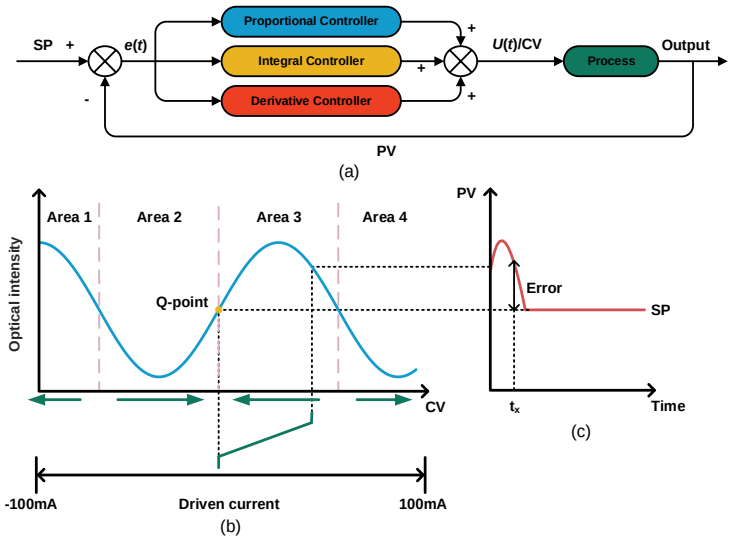

Fig. 2.12. (a) Principle of the closed-loop control system with PID controller. (b) Variation of optical intensity toward driven current. (c) Electrical signals in the time domain.

The detailed compensation process is shown in Fig. 2.12(b) and (c). Figure. 2.12(b) represents the variation of output optical intensity toward driven current and Fig. 2.12(c) is the electrical signals from PD in the time domain. In our BCG monitoring system, SP is the desired value (Q-point, $\varphi = \pi/2$), which is set as half of the peak-to-peak value in the output waveform. PV is the filtered signal in CH2, and CV is the driven current of the phase shifter. The error at time t_x is the value of SP minus PV, as shown in Fig. 2.12(c), which can be obtained by the PID controller. Based on the calculated error and Eq. (2.6), the PID controller will adjust the phase shifter, in which the moving-coil transducer works based on Eq. (2.5) to eventually keep the MZI system in quadrature. When the error is less than 0, as shown in area 1 and area 3 of Fig. 2.12(b), CV will decline accordingly to keep the system in quadrature. Inversely, in area 2 and area 4 of Fig. 2.12(b), the error is large than 0, and CV will increase to pull the bias point back to the Q-point. The time constant of PID is 5 ms. In consequence, the bias point will be kept in the Q-point of the rising edge. Prior to data collection, the system needs calibration. A manual mode is set in the system, in which the phase shifter is triggered to generate cosine waves, and SP is obtained as half of the peak-to-peak value. As presented before, the dynamic range of the phase shifter is 44 rad. In addition, to keep the system up, a CV reset method is introduced and the driven current will be reset to 0 mA when the driven current reaches the limit of ±100 mA. Therefore, according to this compensation way, the BCG monitoring system can always work in the Q-point of a rising edge with stable performance and the BCG signal can be obtained with the desired waveform.

2.4.3 Result and discussion

The experiment setup is shown in Fig. 2.13. When the subject sits on the smart cushion, vibration signals from the body recoils in reaction to the heartbeat can be caught, and the BCG signal is recorded by the DAQ card. Since the sensor does not directly attach to the skin surface, it belongs to non-invasive and non-attached heartbeat monitoring. To compare the results with and without the proposed phase modulation method, we directly collect the signal from CH1 first and then activate the closed-loop control system for continuous new data collection. The summarized results are shown in Fig. 2.14. In the first 7-second duration marked with the red background, only part of BCG can be obtained due to the aforementioned signal fading effect, and these signals are distorted as the result of bias point deviation. In contrast, when the closed-loop control system is activated, the signal fading effect is mitigated and the system keeps working on the Q-point. The collected new BCG signal is shown in the last 13 seconds. It can be seen that the baseline drift introduced by ambient noise is removed and desired BCG signal with specific peaks, including I, J, and K peaks, can be obtained successfully and continuously. In BCG-related healthcare applications, I, J, and K peaks play important roles in specific vital signs measurement and even disease diagnosis. The result demonstrates that our proposed phase modulation and compensation method can realize long-term BCG monitoring.

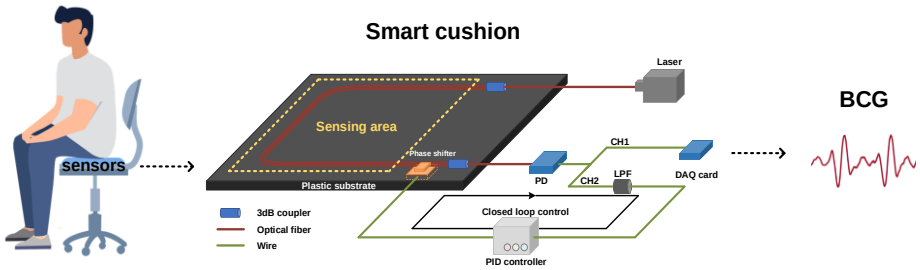

Fig. 2.13. The experiment setup.

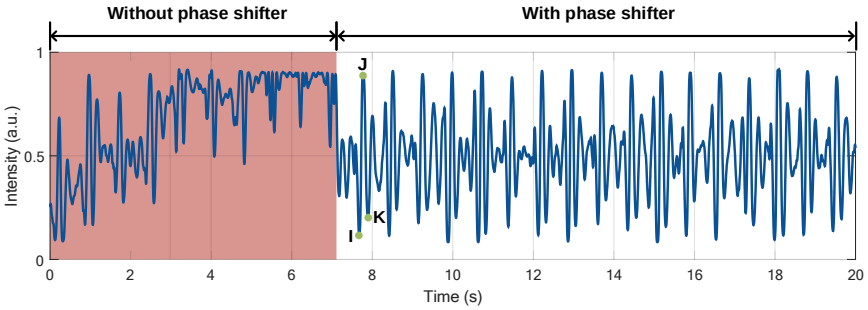

Fig. 2.14. Raw data of BCG signals.

Since the BCG waveform changes from person to person, we collected signals from 7 subjects in health conditions to evaluate the performance of our sensor, of which three are male and four are female. Figure. 2.15 shows the raw BCG signals from these subjects based on the MZI with phase compensation, and each data lasts for 10 seconds. It can be seen that the baseline introduced by breath and ambient noise can be eliminated by the phase compensation method for 7 subjects. Most J peaks of subjects with different HRs can be detected clearly by the sensor. The results show that the proposed BCG monitor has good adaptability for different subjects.

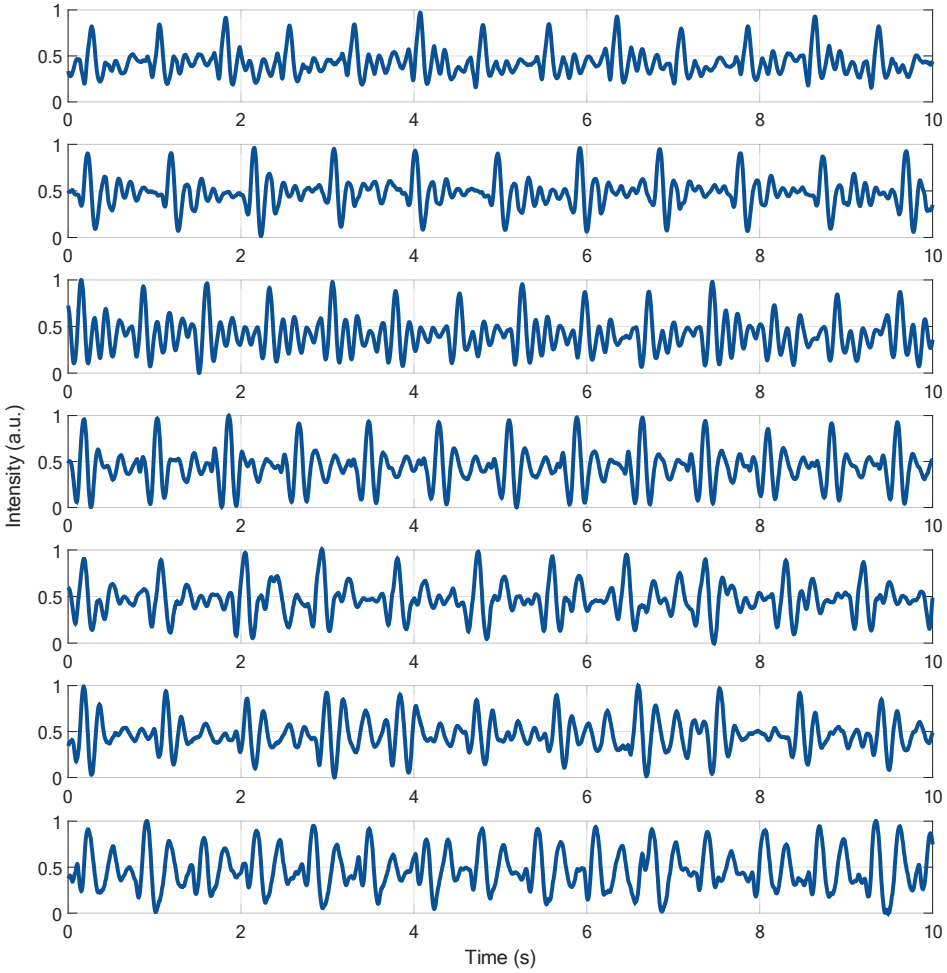

Fig. 2.15. Raw BCG signal from 7 subjects.

2.5 Summary

In this chapter, the optical fiber interferometer-based vital signs monitor and traditional phase interrogation schemes are introduced first. Then, we propose a BCG monitoring system based on an optical fiber interferometer with a low-cost and easily integrated phase shifter. The proposed moving-coil transducer-based phase shifter can maintain the optical fiber interferometer system in quadrature by the PID controller. The signal fading problem can be solved successfully and a BCG signal with good quality can be obtained. The proposed BCG monitoring system can implement long-term and stable BCG

monitoring for users, which has tremendous potential in future healthcare applications.

Chapter 3

Individual heartbeat detection algorithms

3.1 Introduction

A complete BCG consists of H, I, J, K, and L waves, as described in chapter 1. The J peak is the most obvious in the BCG and it is usually used to calculate the HR. Since BCG is related to the body recoils of the subject, it can be interfered and distorted by the motion artifact and ambient noise during the measurement. A segment of BCG is shown in Fig. 3.1, which contains the IJK complex and body movement noise. To calculate the HR and further analyze the IJK complex, the individual heartbeat detection algorithm is crucial for BCG signal processing.

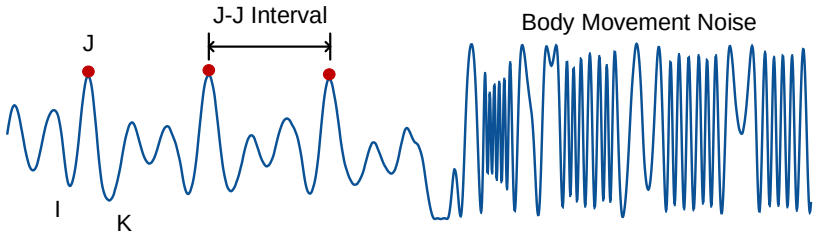

Fig. 3.1. A BCG segment.

Currently, many signal processing methods are proposed to locate the J peak or IJK complex in the BCG signals. Among them, template matching is a common method based on the correlation between a fixed heartbeat

template and the obtained signal [84]. Other than that, the dispersion-maximum algorithm is also adopted to detect the J peak and calculate the HR [85]. In addition, machine learning algorithms, such as k-means clustering [86] and SVM [87], are proposed to classify different peaks and thus extract J peaks from BCG signals. Also, a composite method consisting of CNN and an extreme learning machine (ELM) is used to detect the IJK complex [88]. However, these methods are limited on some points. For example, the template matching method depends heavily on the fixed individual heartbeat template while the waveforms of BCG signal are variable, which results in low robustness. Traditional machine learning algorithms, which are commonly used in classification tasks, need to design and extract features. The process is time-consuming and largely depends on expert knowledge. Although the deep learning algorithm, which can directly extract features, is used in [88], the ECG is necessary to assist in the segmentation of the BCG signal to find the approximate location of J peaks.

In this chapter, we first present a CNN model to recognize the induvial heartbeat IJK-complex from background and body movement data based on the collected signal. The accuracy of the test set is 98.3%, indicating that the network performs well in this classification task. Though the accuracy of the model is high, this algorithm needs a series of pre-processing works, which are time-consuming and unrealistic in a real-time system. Therefore, we propose an end-to-end deep learning algorithm based on a modified U-net to segment the IJK complex and body movement signal in high resolution from the BCG. The features can be learned by the network during training without

other features engineering. More importantly, the BCG signal can be directly fed into the network without much processing, such as removing the body movement signal, which largely simplifies the signal processing.

3.2 Heartbeat detection based on convolutional neural network

3.2.1 Method

CNN is one of the most popular algorithms in deep learning, which is widely used in the task of image processing [89-90]. The CNN is well suited for the classification tasks and thus many researchers utilize CNN to identify different types of individual heartbeat segments. Whiting et al. proposed an RNN model to identify waveforms with cardiac abnormalities in the PGG signals [91]. Kachuee et al. built a 13 weight layers CNN to classify five different arrhythmias based on ECG signals [92]. Inspired by this research, we develop a 10-layer CNN to identify the IJK complex in the BCG signal.

The obtained BCG signals are used as inputs and fed into the proposed CNN model for the J peak detection task, the network architecture of which is shown in Fig. 3.2. The network consists of 1-D convolutional layers, max pooling layers, an FCL, and an output layer. Each 1-D convolutional layer in the network has 16 filters, the size of which is 5. ReLU activation function is used in each convolutional layer. In addition, the size and stride of max pooling layer are both 2. We use a global max pooling followed by an FCL with 64 neurons instead of directly flattening the last convolution layer, which is less prone to overfitting [93]. Finally, the output layer with SoftMax

activation function can generate a distribution over 3 types of classes, including IJK complex, background, and body movement signals. In total, the network has 10 weight layers.

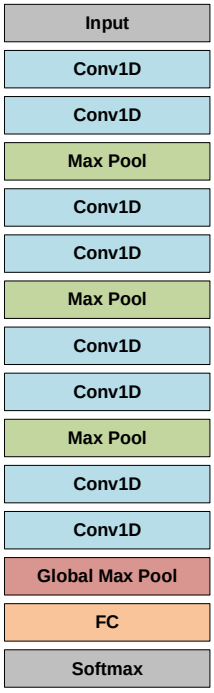

Fig. 3.2. The architecture of a proposed CNN.

The raw data is collected from different subjects in healthy conditions and the sampling rate is 1000 Hz. During data collection, the subjects are required to sit on the smart cushion and remain still for several minutes. To collect uniform body movement data, subjects are asked to move multiple times. In the collected data, baseline drift is removed by the phase compensation system and the signal is normalized to the range of 0 to 1. A segment of raw BCG data lasting for 1000 ms is shown in Fig. 3.3(a). The 200 ms data before and after the J peak in the red dashed box is selected as the IJK complex segment, which contains useful information including I, J,

and K peaks for further study. The 400 ms data segment followed by the extracted IJK complex segments in the yellow dashed box is selected as the background signal segment. In addition, the collected body movement signals are divided into 2250 data segments, each lasting 400 ms. Due to the intensity of the BCG signal varying among different subjects, IJK complex segments will be zoomed into different intensity scales and fed into the network to enhance the performance of the model. Three types of samples including IJK complex segments, background segments, and body movement segments are shown in Fig. 3.3(b) to (d). In total, 11664 samples are fed into the network to train the model, and the ratio between the training set and the validation set is 8 to 2.

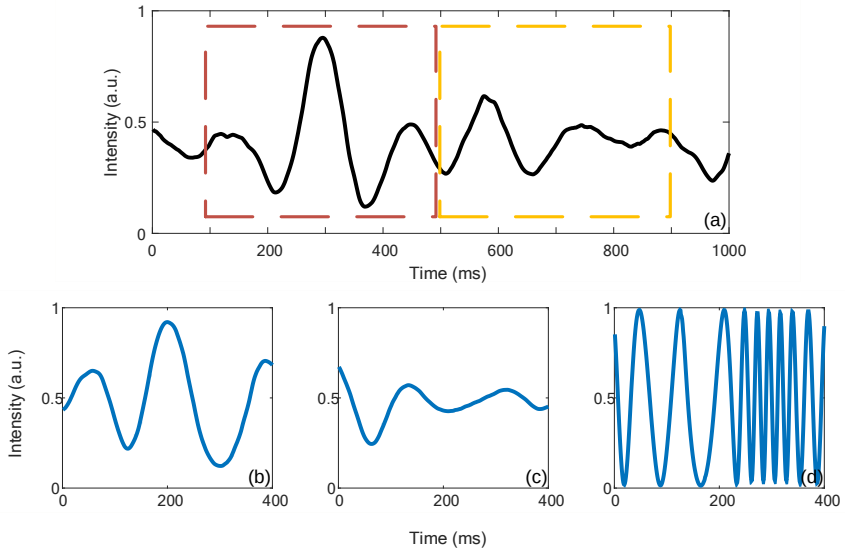

Fig. 3.3 A detailed BCG signal segment (a) and training samples of IJK complex segment (b), background segment (c) and body movement segment (d).

3.2.2 Result and discussion

In the experiment, the Adam optimization method [94] with default parameters (learning rate: 0.001, beta-1: 0.9, beta-2: 0.99) and cross entropy loss are used as the optimizer and the loss function to train the network. During the training process, the best parameters of the network are saved when the highest accuracy of the validation set is obtained. To test the performance of the network, we use 3293 samples including IJK complex segments, background segments, and body movement segments as the test set. Finally, the accuracy result of the test set is 98.3%, which shows the network performs well on the task of identifying the IJK complex in the BCG signals.

The workflow of the heartbeat detection algorithm is shown in Fig. 3.4. The candidate J peaks are first selected by the local maxima method. Then, the 200 ms data before and after the candidate J peak is segmented as the candidate IJK complex segment. Finally, the CNN model can give a prediction of the input segment. Figure. 3.5 shows four groups of BCG data lasting for 10 seconds from three subjects in the test set. The red, yellow, and green dots in the figure represent IJK complex, background, and body movement signals respectively based on the prediction of the network. It can be clearly seen that the correct positions of the IJK complex can be detected in the BCG signal. In addition, the BCG data including sinus arrhythmia can be detected, as shown in Fig. 3.5(c). The sinus arrhythmia signal includes a J peak segment followed by a background segment, which is different from the common noise signal such as disruption of system reset shown in Fig. 3.5(d).

Though the accuracy of the test data is high, the proposed CNN-based heartbeat detection scheme needs to select and segment candidate J peaks in advance, which is time-consuming and unrealistic in a real-time system. As a result, we present an end-to-end algorithm based on the modified U-net to improve the heartbeat detection algorithm.

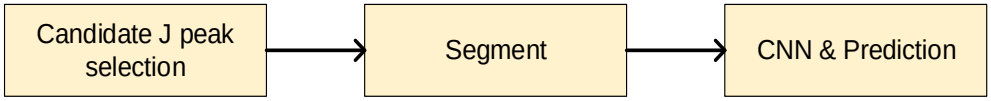

Fig. 3.4. The workflow of the heartbeat detection algorithm based on CNN.

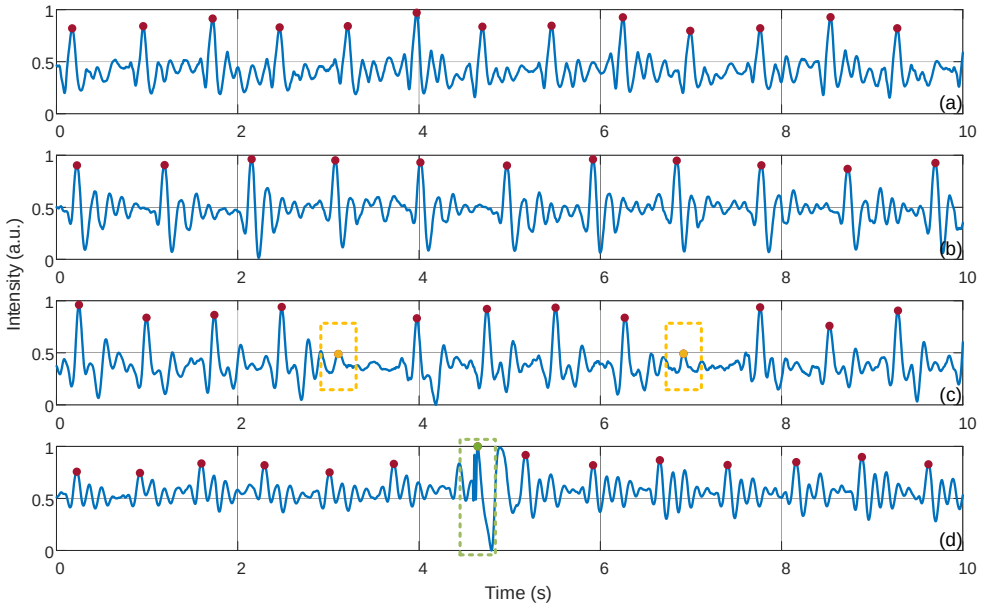

Fig. 3.5. BCG data with the prediction from CNN: (a) BCG signal of subject 1. (b) BCG signal of subject 2. (c) BCG signal with sinus arrhythmia from subject 3. (d) BCG signal with the noise of system reset from subject 3.

3.3 End-to-end heartbeat detection algorithm based on U-net

3.3.1 Method

U-net [95] is a widely used high-resolution segmentation algorithm and it has

been demonstrated with excellent performance in the task of biomedical image segmentation. U-net can perform pixel-wise classification, which means each pixel is assigned to one type of class. U-net is based on the CNN, consisting of the contracting path and expansive path. In the contracting path, the size of the feature map will be reduced by the pooling operation, and in contrast, the output resolution can be increased by the upsampling operation in the expansive path. Therefore, the segmentation map in the output layer will have the same size as the input segment, and it can give the prediction of the input segment at the pixel level, which is a pixel-to-pixel mapping.

BCG is a flexible signal and varies from person to person. The U-net is modified to extract the location information of the IJK complex and body movement signal, which can be used for beat-wise BCG analysis. The architecture of the modified U-net is shown in Fig. 3.6, in which three contracting and expansive stages are included. The left part is the contracting path, each stage in which consists of repeated two 15×1 1-D convolutional layers with ReLU activation function followed by a 2×1 max pooling layer with stride 2 to halve the size of feature maps. The number of filters (nf) in the convolutional layer doubles at each downsampling stage. The right part is the expansive path, and at each stage, an upsampling layer followed by a 2×1 convolutional layer is used to double the size of the feature map and halve the number of feature channels. The feature map in the corresponding contracting stage is directly duplicated and combined with the upsampled feature map in the expansive path. The combined feature map is followed by two 15×1 1-D convolutional layers with ReLU and the filter number of convolutional layers

is halved at each upsampling stage. Compared with the conventional U-net, since we use the same padding instead of valid padding in the convolutional layer, cropping is not needed in the concatenation process. Finally, a convolutional layer with a SoftMax activation function, the kernel size and filter number of which are 1×1 and 3, is used in the output layer to predict the class of each sampling point, including IJK complex, body movement signal, and background. In total, the network consists of 18 convolutional layers.

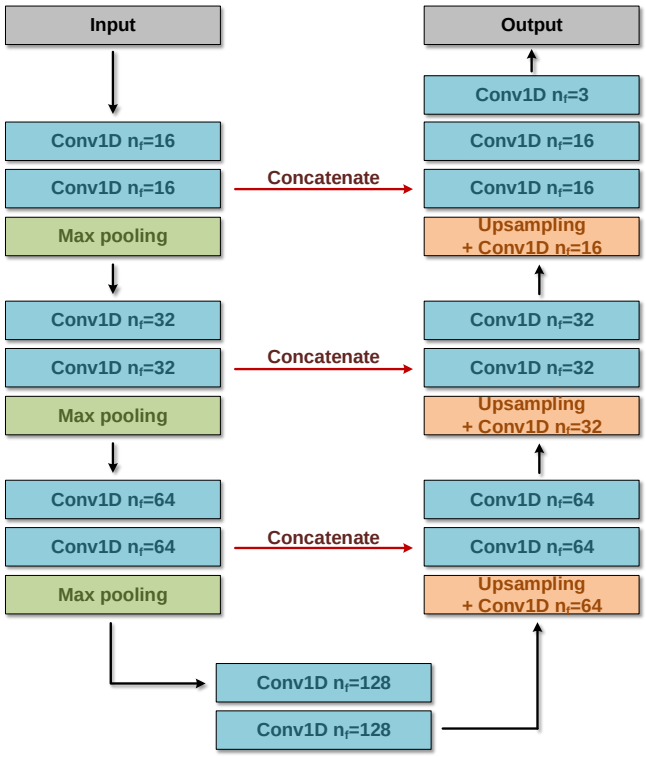

Fig. 3.6. The architecture of modified U-net. nf is the number of filters in 1-D convolution layer.

Compared to the previous CNN-based heartbeat detection algorithm, the raw data are downsampled from 1000 Hz to 500 Hz to reduce the size of the modified U-net. All the raw data are segmented with the same data length of 2048 and one of these segments lasting for 4.096 seconds with both heartbeat

and body movement signals is shown in Fig. 3.7(a), in which the intensity is normalized. The background, IJK complex, and body movement signal are labeled as 0, 1, and 2 in the corresponding sampling point and we can get the label with the same size as input data, as shown in Fig. 3.7(b).

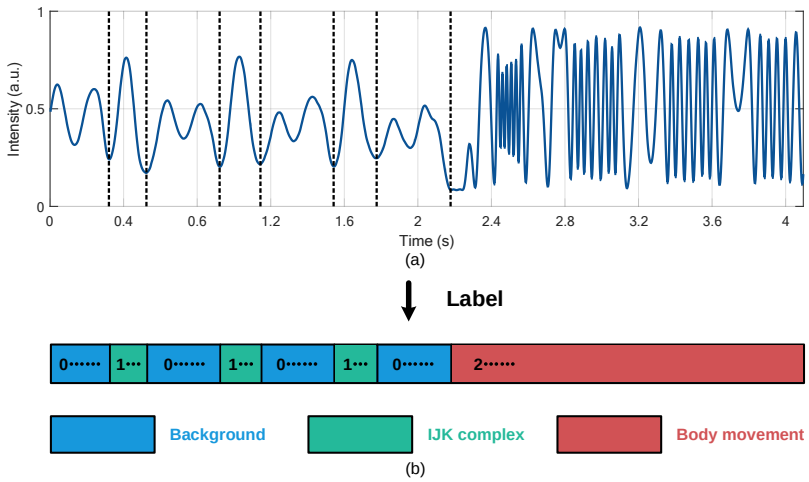

Fig. 3.7. A BCG segment (a) with corresponding label (b).

To train the network, we totally collect 1147 segments, in which 4948 individual heartbeat (IJK complex) and body movement signals are included. The ratio between the training set and validation set is 8 to 2. Adam optimization method with default parameters (learning rate: 0.001, beta-1: 0.9, beta-2: 0.99) is used as the optimizer. The cross-entropy loss is adopted as the loss function. In addition, mini-batch gradient descent is adopted and the batch size of which is 16. During the training stage, when higher accuracy of the validation set is achieved, the parameters of the network will be saved.

3.3.2 Evaluation metrics

To evaluate the segmentation performance of the network, three metrics including pixel accuracy (PA), mean pixel accuracy (MPA) and mean

intersection over union (MIOU) are adopted [96]. PA is the percentage of the correctly labeled pixels to the total pixel, which can be given by

$$PA = \frac{\sum_i n_{ii}}{\sum_i \sum_j n_{ij}}, \tag{3.1}$$

where n_{ij} means the number of pixels in class i are assigned to class j. MPA represents the mean of pixel accuracy in each class, which can be described as

$$MPA = \frac{1}{n_{cl}} \sum_i \frac{n_{ii}}{\sum_j n_{ij}}, \tag{3.2}$$

where n_{cl} is the number of different classes. MIOU is a commonly used metric in the task of segmentation, which represents the similarity between the predicted region and the actual region. MIOU can be given by

$$MIOU = \frac{1}{n_{cl}} \sum_i \frac{n_{ii}}{\sum_j n_{ij} + \sum_j n_{ji} - n_{ii}}. \tag{3.3}$$

Since the BCG signal is one-dimension data, the number of pixels in the above equation can be replaced by the number of sampling points in the data.

3.3.3 Result and discussion

To test the modified U-net, we use 511 BCG segments from 7 subjects as a test set, including 2107 individual heartbeat (IJK complex) and body movement signals. These test data were collected on different days and 3 subjects did not participate in the data collection of the training set. Figure. 3.8(a) shows the confusion matrix of the test set in the pixel-wise classification task. We can calculate the PA, MPA, and MIOU through the confusion matrix, which is 99.66%, 99.59%, and 99.18%, respectively. In addition, to verify the accuracy of I-K intervals in the predicted IJK complex,

we calculate the mean absolute error (MAE) between predicted and actual I-K intervals in the test set and the result of which is 1.75 ms. The scatterplot of predicted versus actual I-K intervals is shown in Fig. 3.8(b). The results show the modified U-net performs well on the task of IJK complex and body movement segmentation in the BCG data.

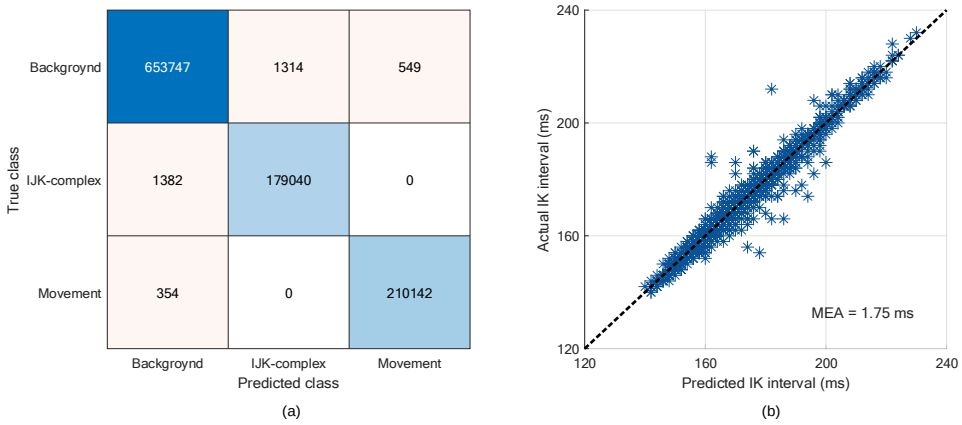

Fig. 3.8. (a) Confusion matrix of test set. (b) The scatterplot of predicted versus actual I-K interval.

Figure. 3.9 shows five kinds of segmentation results of BCG signal, the red line of which is the classification result. Figure. 3.9(a) is a BCG segment from one of the subjects, in which we can find that there are six heartbeats during 4.096 seconds (82 bpm) and the position of each IJK complex can be predicted by the network accurately. Also, to confirm the feasibility of IJK complex detection for subjects with different HRs, we select two sets of BCG segments from another two subjects with the lower HR (67 bpm) and the higher HR (97 bpm) shown in Fig. 3.9(b) and (c), respectively. In addition, though the 7 subjects in the experiment are all in healthy condition, we also find some BCG segments with occasional sinus arrhythmia from one subject,

which may be caused by nervous, as shown in Fig. 3.9(d), and the IJK complex can also be segmented accurately. Apart from the IJK complex, the network can also implement the segmentation of body movement signals. A BCG segment recording the body movement on the chair is shown in Fig. 3.9(e), and the IJK complex and body movement signal can be segmented perfectly by the network. In summary, compared with many existing algorithms, our modified U-net is an end-to-end algorithm, and it can accurately detect the location information of the IJK complex and body movement in the BCG signal without much processing, which is time-saving for BCG signal analysis.

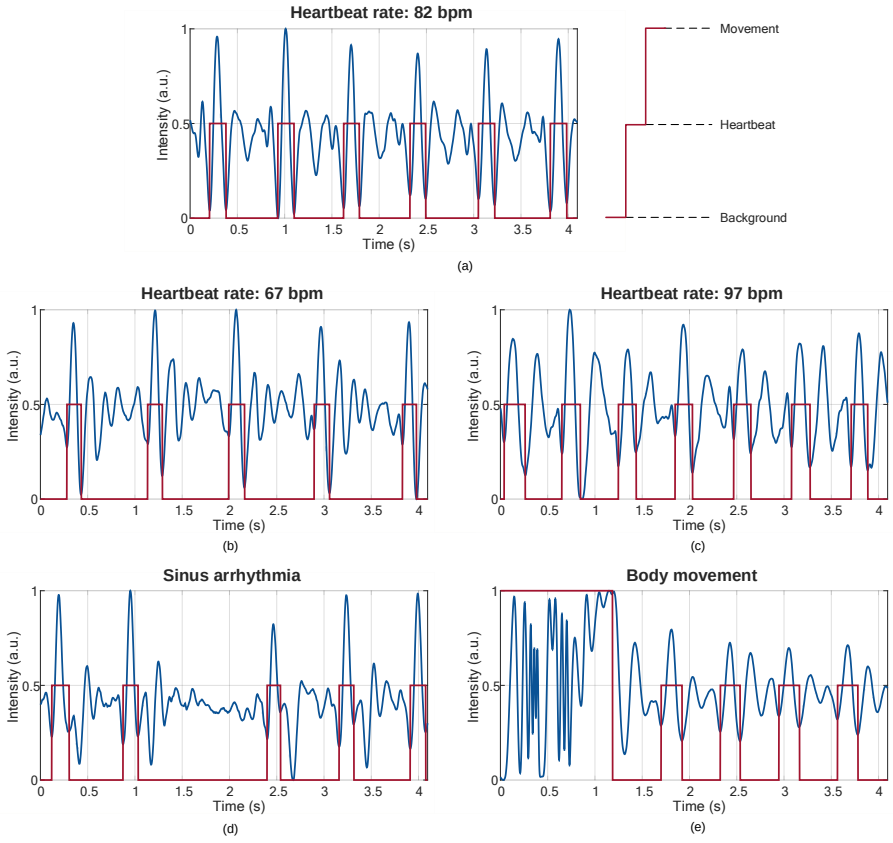

Fig. 3.9. BCG segmentation results based on modified U-net: (a) BCG signal with HR of 82 bpm; (b) BCG signal with HR of 67 bpm; (c) BCG signal with HR of 97 bpm; (d) BCG signal with occasional sinus arrhythmia; (e) BCG signal with body movement.

3.5 Summary

An accurate individual heartbeat signal extraction algorithm in the BCG signal is critical for subsequent HR analysis and CVD diagnosis since motion artifacts and ambient noise can interfere with the BCG signal during measurement. In this chapter, we first propose a CNN model to identify the induvial heartbeat IJK-complex from the background and body movement signals. The accuracy result of the test set is 98.3%, and it shows that the network performs well on this classification task. However, this model needs a series of pre-processing works, which is time-consuming and not realistic in the real-time system. Therefore, we develop an end-to-end IJK detection algorithm based on the modified U-net to replace it. The PA, MPA, and MIOU of the network in the test set are 99.66%, 99.59%, and 99.18%. The MAE of the predicted IK interval in the test set is 1.75 ms. The results reveal that our proposed network performs well in the job of segmenting IJK complex and body movement signals.

Chapter 4

Ballistocardiography reconstruction algorithm based on the pix2pix Generative Adversarial Network

4.1 Introduction

To solve the signal fading problem in optical fiber interferometers and obtain good-quality BCG recording with I, J, K waves, many modulation and demodulation technologies are adopted and investigated. For example, traditional schemes, such as 3 × 3 coupler-based demodulation and phase generated carrier technique, are introduced to reconstruct the heartbeat and breath signals. Furthermore, we adopt the phase compensation method based on a close loop control system to address this problem in the previous work [97]. The mentioned schemes need additional hardware in the system. Therefore, we intend to reduce the complexity and cost of the hardware by replacing the modulator and demodulator with a reconstruction algorithm. In theory, the detected intensity signal is linear with BCG when the operating point is biased at the Q-point in the interferometer. In practice, however, the

operating point will deviate from Q-point due to the ambient noise, which results in the nonlinear problem in the detected signals. Because of the complex mathematical model caused by the dynamic drift of the operating point, it is difficult to develop a traditional algorithm to reconstruct BCG signals detected from an interferometer based on the intensity interrogation mode.

Deep learning algorithms have evolved rapidly recently and been widely employed in various fields [98]. Many deep learning models are successfully applied to BCG signal processing, such as BR and HR calculation [99] and individual heartbeat detection [100]. In addition, reconstruction algorithms have also been extensively investigated based on the deep learning model. Among them, various models are applied in the research of optical fiber devices to replace traditional solutions. For example, deep neural networks [101], U-net [102], and GAN [103] are adopted in image reconstruction through multi-mode fibers. Convolutional neural networks are used for mode decomposition in the few-mode fibers [104] and multi-mode fibers [105-106]. Inspired by these studies, we propose to adopt the GAN to build a reconstruction model. GANs are the common generative models, which can generate the desired distribution and improve the generative results through an adversarial process between generator and discriminator models [107]. pix2pix generative adversarial network (pix2pix GAN) is a variant of GAN [108]. Its generator has a structure of the encoder-decoder network, which can learn the mapping function and be used to build the reconstruction model. Although pix2pix GAN is a powerful model for two-dimension image

processing, it cannot be directly applied to analyze the time-series signals, such as BCG.

Therefore, the present study is conducted to reconstruct signals from an optical fiber interferometer based on the intensity interrogation mode. A BCG reconstruction algorithm inspired by pix2pix GAN is proposed based on this purpose. To our knowledge, it is the first time to utilize an algorithm to solve the signal fading problem in the optical fiber interferometer-based BCG monitoring system. It means that additional phase modulators and demodulators are no longer needed in the interferometer. In our work, parameters of the neural network architecture are investigated and optimized, and several metrics are adopted to evaluate the accuracy of reconstructed BCG signals and I, J, and K waves. Moreover, we test the performance of the BCG reconstruction algorithm with two special BCG signals, which are sinus arrhythmia data with specific heartbeat patterns and post-exercise data owning variational inter-beat intervals (IBIs), respectively. In conclusion, the proposed BCG reconstruction algorithm can solve the signal fading problem in optical fiber interferometers innovatively, which could be further applied in related applications, such as pulse wave reconstruction in the interferometer.

4.2 Principle

Our BCG monitoring system is an optical fiber MZI based on the intensity interrogation mode. As shown in Fig. 4.1(a), the optical system contains a DFB laser, an MZI-based BCG monitor, a PD, and a DAQ card. The optical

fibers in the system are SMFs. BCG is a vibration signal that comes from body recoils resulting from cardiac activities. When subjects sit on the sensor, the phase change introduced by body recoils in the MZI can be detected by the optical intensity, which is referred to as raw BCG signals. Since the operating point deviates from the Q-point affected by the ambient noise, the obtained I, J, and K waves in the BCG will be distorted. It makes the subsequent signal processing tasks difficult, such as HR calculation and HRV analysis. Instead of using complex modulation and demodulation devices to solve the problem, we propose to reconstruct BCG signals based on an algorithm by building a mapping model. The model can map raw signals to the BCG signal with standard I, J, and K waves, which is called the reference BCG signal. As shown in Fig. 4.1(b), reference BCG signals can be collected by the reference system [97] and work as the ground truth. In addition to the MZI-based BCG monitor, the reference system has a phase compensation system to keep the operating point at Q-point.

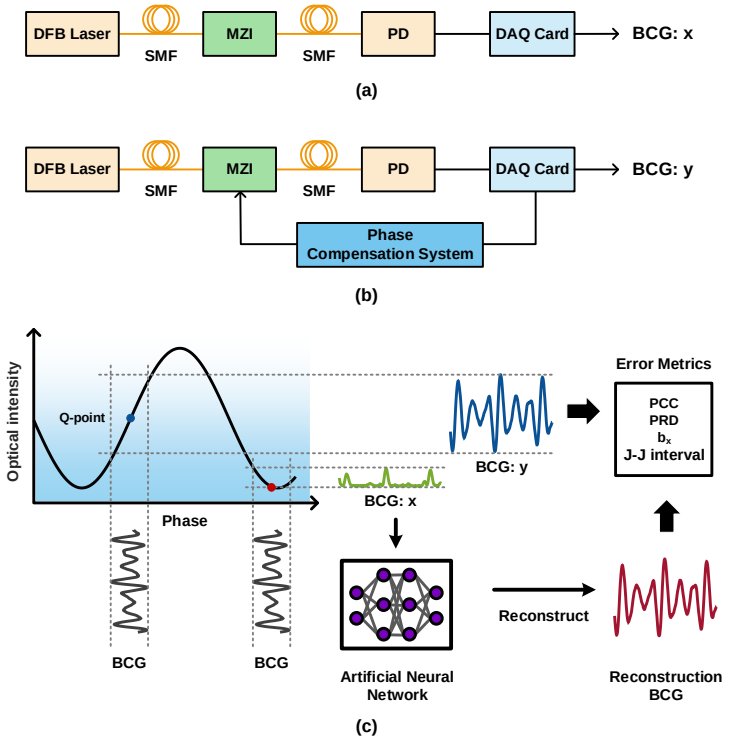

Fig. 4.1. The optical systems of (a) the BCG monitor and (b) the reference BCG monitor with a phase compensation system. (c) The overview of the reconstruction method.

The overview of the reconstruction method is shown in Fig. 4.1(c). We assume that the operating point of the raw BCG signal drifts to the red point in the change curve of optical intensity with phase. Meanwhile, the operating point of the reference system is kept at Q-point, which is the blue point in the curve. The output optical intensity of the MZI can be given as $I = A + B\cos(\varphi)$, where constants A and B are related to the light intensities of two arms in the MZI. We use x and y to represent the optical intensities of the raw BCG signal and the reference BCG signal, respectively. Therefore, x and y can be simplified to

$$x = cos[\varphi_{BCG}(t) + \varphi_n(t)], \tag{4.1}$$

$$y = cos\left[\varphi_{BCG}(t) + \varphi_n(t) + \varphi_{comp}(t)\right], \tag{4.2}$$

where $\varphi_{BCG}(t)$ and $\varphi_n(t)$ are phases introduced in the MZI by cardiac activities and ambient noise. $\varphi_{comp}(t) = 3\pi / 2 + 2n\pi - \varphi_n(t)$ is the phase introduced by the real-time phase compensation system, which keeps the operating point at the Q-point of the rising edge by eliminating $\varphi_n(t)$. Since the change curve of optical intensity with phase is approximately linear in the reference system, y can be obtained as $y \approx C\varphi_{BCG}(t)$, where C is a constant. The waveforms of x and y are shown in the green and blue lines in Fig. 4.1(c). We want to obtain y based on x but it is hard to be solved directly. Therefore, we propose to build the mapping model between x and y based on the deep learning method, which can be briefly described as

$$\hat{y} = f_\theta(x) \approx y, \tag{4.3}$$

where $f_\theta: \mathbb{R}^N \to \mathbb{R}^N$ is the mapping function and $\boldsymbol{\theta}$ contains the parameters in the mapping model, such as weights in the neural network. x and y are discretized by the DAQ card, and $\hat{y}$ is the reconstructed result based on x. The goal of the deep learning algorithm is to optimize $\boldsymbol{\theta}$ that minimizes the error between $\hat{y}$ and y.

4.3 Modified algorithm

The proposed deep learning-based BCG reconstruction algorithm is modified from pix2pix GAN. The pix2pix GAN is a kind of conditional generative adversarial network (conditional GAN) whose generator and discriminator are conditioned on the given information [109]. Compared to the typical conditional GAN which generates data based on some simple features, the generator structure in the pix2pix GAN is an encoder-decoder network and it

can predict from pixels to pixels. Therefore, it can be used to build the mapping model between raw and reference BCG signals. However, pix2pix GAN is optimized in the image processing and it cannot be directly applied in the time domain signals. To cope with this, we modify the pix2pix GAN into a 1-D model to fit the BCG reconstruction.

The modified model consists of a generator (G) and a discriminator (D). In our case, G learns the mapping between raw and reference BCG signals, and its input is raw BCG data and output is the reconstructed BCG result. D helps improve G's performance through the adversarial process. The training process of GAN is shown in Fig. 4.2(a) and there are three steps involved at each iteration. In step 1, D is trained to distinguish the true data with the input of reference data *y*. The label of *y* is 1, which means D is told that the input data are true. In step 2, D is trained to distinguish the fake data by feeding the generative data *G*(*x*). *G*(*x*) is generated by G based on raw data *x*. The label of *G*(*x*) is 0 representing the fake input data. In step 3, we combinate D and G, and the parameters in D are frozen. *G*(*x*) is fed into D with label 1, and thus G tries to generate data that is close to true data to fool D in this process. G will update its parameters in this step. In three steps, raw data *x* is paired with the input data fed into D to improve the performance. The loss function in the network refers to [26], which can be shown as

$$L_{cGAN}(G,D) = E_{x,y}[log\, D\,(x,y)] + E_x\left[log\left(1 - D\left(\left(x, G(x)\right)\right)\right)\right], \quad (4.4)$$

$$L_{L1}(G) = \mathrm{E}_{x,y}[\|y - G(x)\|_1], \quad (4.5)$$

$$G* = arg\min_G \max_D L_{cGAN}(G,D) + \lambda L_{L1}(G), \quad (4.6)$$

where x, y, and $G(x)$ are raw, reference, and generated signals as mentioned. L_{cGAN} is the conditional GAN loss. L_{L1} is the Manhattan distance between reference and generated samples, which ensures that G is also trained to be close to the ground truth instead of only fooling D. Total loss G^* mixes the conditional GAN loss L_{cGAN} and the traditional Manhattan distance loss L_{L1} with weight λ.

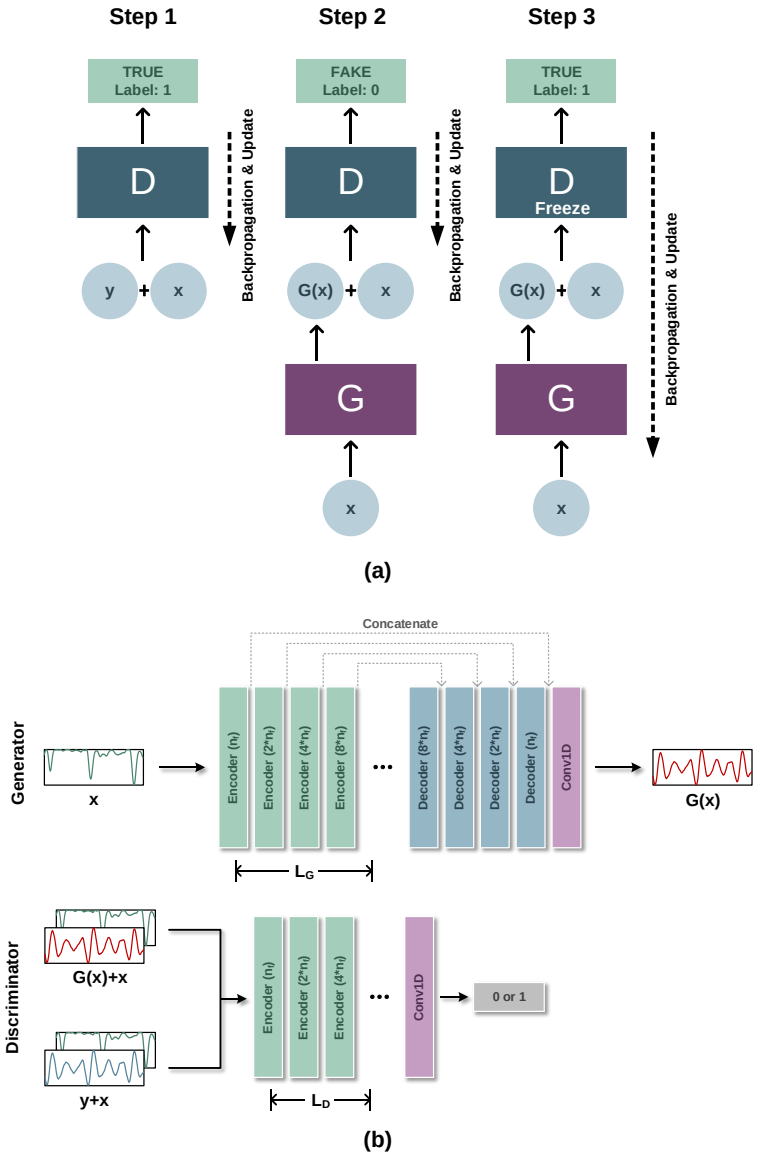

Fig. 4.2. (a) Training process of GAN. (b) Architecture of the BCG reconstruction algorithm.

The architecture of the BCG reconstruction algorithm is shown in Fig. 4.2(b). The network structure of G is similar to that of the 1-D U-net. During the encoding step, the size of feature maps is compressed to half at each encoder block. The number of filter channels is double that of the previous encoder block, and the initial number is n_f. The encoder block consists of a 1-D strided convolutional layer with LeakyReLU activation function [110] followed by batch normalization. In the decoding stage, inversely, the size of the feature map doubles, and the channel halves at each symmetric decoder block. The skip connections are added between the symmetric layers in the encoding and decoding stages. Thus, the input size is equal to the output size, which is $N \times 1$. L_G represents the number of encoder blocks in G, which is related to the performance of G. The network of D is a convolutional PatchGAN classifier, which penalizes the input at the scale of patches and averages all results as output. The L_D is the number of encoder blocks in D and the strided convolutional layer can adjust the size of the patch. In the experiment, we investigated various combinations of different values of L_G and L_D to optimize the model.

4.4 Experiment setup and evaluation methods

To build the mapping model between raw and reference BCG signals, we packaged the mentioned two sensors together in a cushion, ensuring that raw and reference BCG signals can be detected simultaneously. In the data collection stage, the sensors are placed on a stable chair, and the subjects are asked to sit on it and keep still. The raw and reference signals from two

sensors will be collected simultaneously by the DAQ card (National Instrument, USB6001) with a sampling rate of 1000 Hz, and then transferred to the computer for further processing, as shown in Fig. 4.3. We collected data from multiple healthy participants for a two-week period to make the mapping model more resistant to small variations like distinct sitting postures.

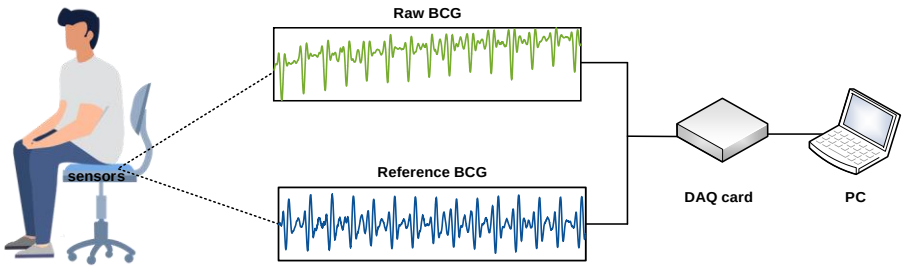

Fig. 4.3. The experiment setup.

Since BCG signals cannot be detected when the subject is moving, the useless segments of signals caused by body movement are removed simultaneously in both raw and reference signals. The sampling rate of signals is reduced to 500 Hz in order to limit the peak of memory usage during training. A high-pass filter is applied to raw signals to eliminate the baseline drift. Since there is a slight time delay between the raw and reference signals due to the different working mechanisms of sensors, manual time calibration is needed. In addition, the raw and reference signals are divided into segments of consistent length N = 2048 (4.096s duration) without overlapping and normalized to a range of -1 to 1. These data are used as a basic dataset to train and optimize the model.

In the model, the reconstructed performance is affected by several parameters. Three metrics are adopted to estimate the model and optimize

these parameters, including Pearson correlation coefficient (PCC), percent root mean square difference (PRD), and regression coefficient (b_x) [111]. PCC refers to the correlative degree between reconstructed and reference BCG signals, and a value of 1 indicates a strong positive correlation between the two signals. PRD represents the error between reconstructed and reference BCG signals and a smaller PRD means the higher performance of the reconstruction algorithm. Furthermore, b_x estimates the amplitude difference between the two BCG signals with a value closer to 1 being better. These metrics are shown in Eq. (4.7)-(4.9), where *N* is the number of samples, and G_x, *y* are reconstructed and reference BCG signals.

$$\text{PCC} = \frac{\sum_{n=1}^{N}\left(G_x(n) - \overline{G_x}\right)(y(n) - \overline{y})}{\sqrt{\sum_{n=1}^{N}\left(G_x(n) - \overline{G_x}\right)^2}\sqrt{\sum_{n=1}^{N}(y(n) - \overline{y})^2}}, \tag{4.7}$$

$$\text{PRD}\ (\%) = \sqrt{\frac{\sum_{n=1}^{N}\left(G_x(n) - y(n)\right)^2}{\sum_{n=1}^{N}\left(y(n)\right)^2}} \times 100, \tag{4.8}$$

$$b_x = \frac{\sum_{n=1}^{N} G_x(n)y(n)}{\sum_{n=1}^{N}\left(y(n)\right)^2}. \tag{4.9}$$

Furthermore, another measure adopted to assess the model is based on the reconstructed IJK complex in BCG signals. IJK complex, consisting of I, J, and K waves, is the most visually obvious part of BCG. The I, J, and K waves can be used to estimate important cardiovascular parameters. As shown in Fig. 4.4, we use I, J, K waves and I', J', K' waves to distinguish the IJK complex in the reference and reconstructed BCG signals. The MAE between J-J intervals and J'-J' intervals is adopted as one metric to evaluate the time error of the IBI. Meanwhile, we use the error between I, J, K waves

and I’, J’, K’ waves as the additional metrics to evaluate the time delay of the reconstructed BCG signals.

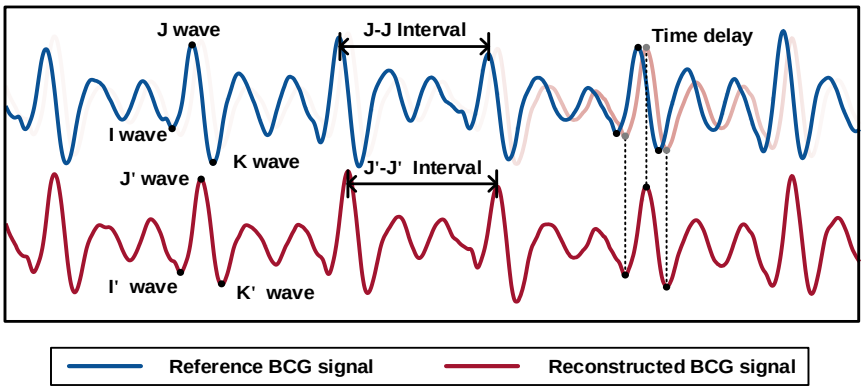

Fig. 4.4. I, J, K waves in the BCG signal.

In the basic dataset, the heartbeat patterns are regular and HRs mainly range from 60 to 100 bpm. However, the BCG signals may become complex in some special cases. For example, the HR may exceed 100 bpm in the post-exercise condition. To evaluate the performance of the model in different scenarios, we collected special BCG signals including sinus arrhythmia data and post-exercise data, which own irregular heartbeat patterns and variational IBI, respectively. The details of reconstruction results are shown as follows.

4.5 Result and discussion

In the training process, since D usually converges faster than G, it is hard for the GAN model to balance G and D. If so, the model may fail to learn. Therefore, a series of parameters are investigated to balance the performance between G and D networks during the adversarial process and get a high-quality BCG reconstruction result. According to the preliminary experiment,

some parameters are determined first. The kernel sizes of G and D networks are both 15 × 1, and the number of initial filter channel n_f in the first encoder block is 16. Adam with a learning rate of 0.0002 is chosen as the optimizer in both G and D networks. Mini-batch gradient descent is adopted, and the batch size is 32. Weight λ in Eq. (4.6) is set as 100.

In the following experiment, the collected 7256 BCG segments are randomly divided into the training set and the test set, the ratio of which is 8 to 2. The test set has not been used in the preliminary experiment. Since the training loss cannot directly reflect the training phase of the GAN model, we display a batch of generative signals at a certain iteration cycle and calculate mentioned metrics based on the test set to evaluate the training progress. We set different combinations of block numbers in the G and D and monitor the model performance. Mean PCC, PRD, b_x, and MAE between reconstructed and reference signals in the test set with different values of L_G and L_D are shown in Table 1. We find that increasing the L_G value enhances the performance of the model greatly, while the L_D value affects the performance less. The performance improves marginally when the L_G value is set to 8 and the size of the model grows dramatically. Therefore, we set the number of encoder and decoder block L_G as 7 in the G network, and L_D in the D network is set as 4.

Table. 4.1. Mean PCC, PRD, bx, and MAE in the test set with the combination of different numbers of blocks in G and D networks.

L_G	L_D	PCC	PRD (%)	b_x	MAE
4	3	0.915	38.879	0.888	0.117
	4	0.920	38.004	0.897	0.115
5	3	0.926	36.459	0.899	0.113
	4	0.930	35.658	0.908	0.110
6	3	0.945	31.490	0.910	0.098
	4	0.943	32.007	0.912	0.100
7	3	0.952	29.683	0.918	0.093
	4	0.952	29.875	0.920	0.094
8	3	0.953	29.936	0.918	0.095
	4	0.953	29.838	0.922	0.094

As mentioned, two metrics are developed to verify the correctness of the reconstructed IJK complex in BCG signals. In the test set, the MAE between J-J intervals of reference BCG signals and J'-J' intervals of reconstructed BCG signals is 3.24 ms. The scatterplot of reconstructed J'-J' intervals versus reference J-J intervals is shown in Fig. 4.5(a). In addition, Fig. 4.5(b) is the box plot about absolute errors of time delay between I, J, K waves and I', J', K' waves, the median of which are all 2 ms. A small minority of the IJK complex, which is not detected in the reconstructed and reference segments, are excluded from the statistics. The results show the reconstructed IJK complex is closed to the reference IJK complex.

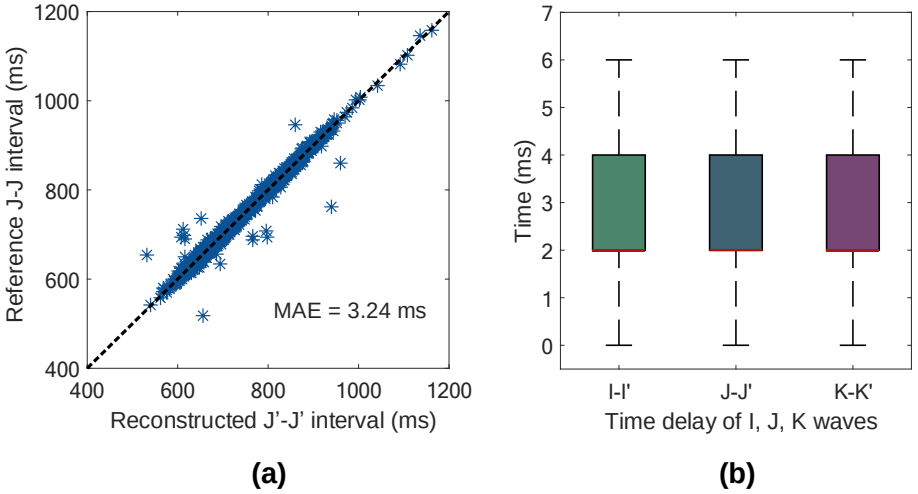

Fig. 4.5. (a) Scatterplot of reconstructed J'-J' intervals versus reference J-J intervals. (b) Box plot of absolute errors of time delay between I, J, K waves and I', J', K' waves.

Then, the heartbeat patterns in the raw BCG signals with varying degrees of distortion are demonstrated. Figure. 4.6 is four common types of heartbeat patterns in the raw BCG signals. The inset picture is the change curve of optical intensity with phase in the MZI, and space α, β, χ, δ are corresponding to positions where operating points are biased in Fig. 4.6(a) to (d), respectively. Among them, the green line in the first row represents raw BCG. Red and blue lines in the second row are the reconstructed BCG and reference BCG. In Fig. 4.6(a), the operating point is very close to the Q-point on the curve with a positive slope, and thus the raw signal is linearly positive with the reference BCG signal. As the operating point moves from space α to β, the raw signal has a nonlinearly positive correlation with the reference BCG signal, which results in signal distortion in Fig. 4.6(b). For Fig. 4.6(c), although the raw signal is linear with the reference BCG signal, it records reversal phase information, which is derived from the operating point being near the Q-point on the curve with a negative slope. Finally, the raw signal is

nonlinearly negative with the reference BCG signal as the operating point drift to space δ, as shown in Fig. 4.6(d). It can be found that in either case, the reconstructed BCG is very close to the reference signal, and PCC between the reconstructed and reference BCG signals in Fig. 4.6 are 0.974, 0.979, 0.980, and 0.976.

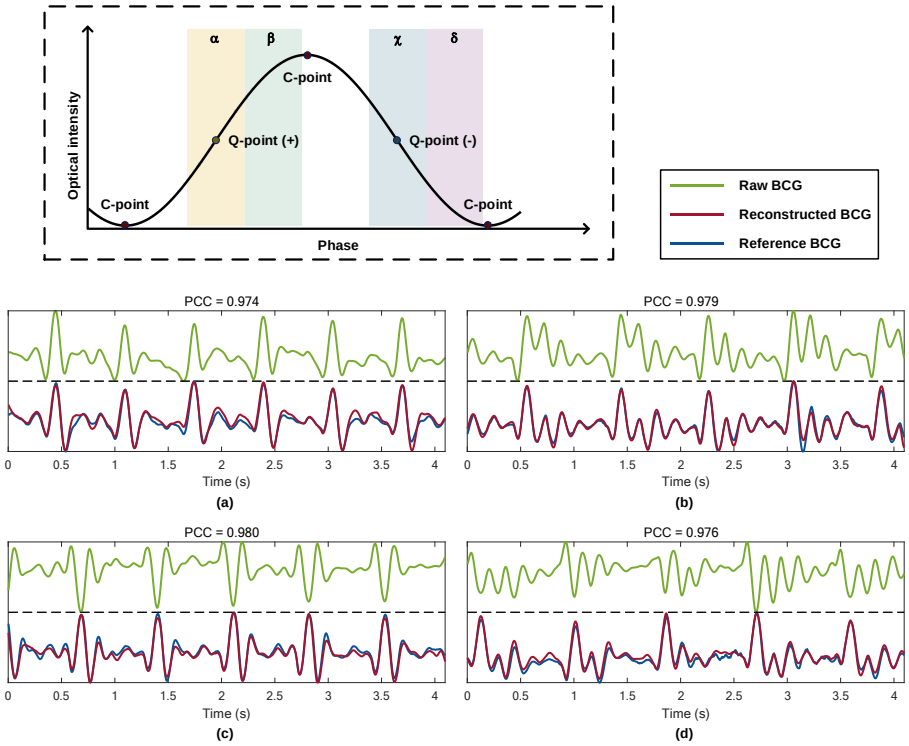

Fig. 4.6. Reconstructed BCG waveforms with different operating points in (a) to (d).

For the worst case, the pattern of the IJK complex in BCG signals is difficult to distinguish when the operating point drifts to the critical point (C-point in Fig. 4.6 inset picture), the waveforms of which are shown in Fig. 4.7. Based on the features of I, J, and K waves found in the raw signal, the mapping model can reconstruct the BCG signal. The PCCs of reconstructed BCG in Fig. 4.7 are 0.969 and 0.976, respectively. Furthermore, the BCG segments of subjects with different HRs are shown in Fig. 4.8(a) and (b). The

model maintains high performance for both faster HR (97 bpm) and slower HR (66 bpm), in which the PCCs are 0.990 and 0.979, respectively.

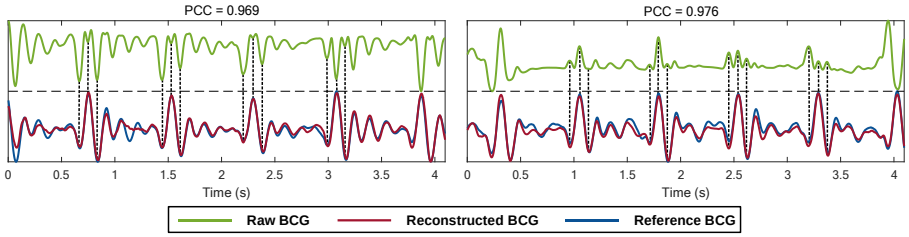

Fig. 4.7. Reconstructed BCG waveforms with poor quality of raw signals.

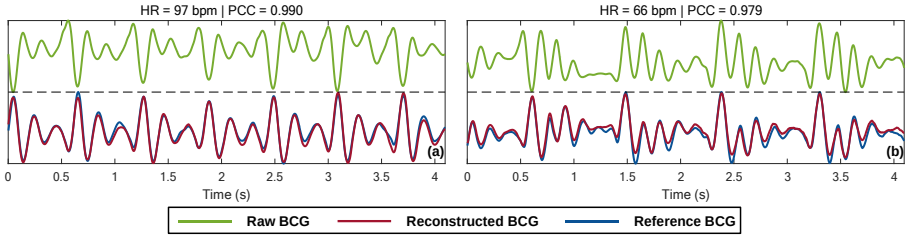

Fig. 4.8. Reconstructed BCG waveforms with different HRs: (a) HR is 97 bpm and (b) HR is 66 bpm.

The heartbeat patterns in the BCG change randomly with the drifting operating point. In addition, the number of heartbeat patterns in each segment depends on the HR of different subjects. Under such a complicated condition, the results show that the model has good adaptability to reconstruct BCG signals and the performance is satisfying, which means the BCG reconstruction algorithm can be used in further cardiac health analysis. Compared to the traditional modulation and demodulation methods, our method can reduce the hardware complexity in the system, which makes the sensor more portable. In further studies, we will try to reduce the complexity of the reconstruction algorithm. Moreover, to further validate the model, we

also present the reconstructed BCG of two special cases collected in different scenarios in the following two parts.

4.6 Special cases

Sinus arrhythmia refers to an irregular heartbeat pattern that happened in healthy people, especially the young [112]. The cause of sinus arrhythmia is that the sinoatrial node does not pace the heart at a regular rate. Respiration is a common cause of sinus arrhythmia, which is called respiratory sinus arrhythmia. The HR usually fluctuates in the process of breathing derived from the change in vagal tone during different respiratory phases. Therefore, respiratory sinus arrhythmia is a significant indicator related to cardiac vagal function.

In the experiment, we found that a few irregular heartbeat patterns are collected from one subject. Therefore, we made the subject wear an ECG monitor (SparkFun, AD8232) and sit on the sensor to collect ECG, raw BCG, and reference BCG simultaneously. Finally, we detected some heartbeat segments with sinus arrhythmia and fed them into the model. Part of the results is shown in Fig. 4.9, in which the red, blue and purple lines represent the reconstructed BCG, reference BCG, and ECG separately. The grey dotted boxes show the irregular heartbeat patterns in collected signals. According to the ECG patterns, the presented segments are identified as sinus arrhythmia. The PCC between the reconstructed and reference segments are 0.915 and 0.932 in Fig. 4.9. Although the PCC decreases a bit compared to that of the

normal BCG reconstructed segment, the reconstruction algorithm still works well.

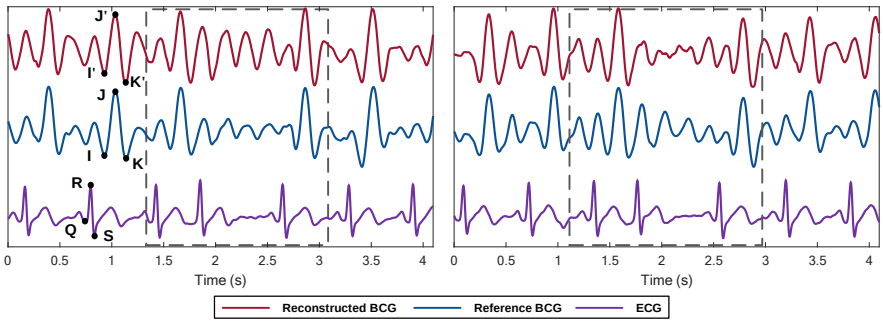

Fig. 4.9. Reconstructed BCG, reference BCG, and ECG segments with sinus arrhythmia.

HRV refers to the temporal variation between the time intervals of consecutive heartbeats, which originates from the autonomic nervous system of humans [113]. These temporal variations are in connection with a variety of physiological disorders, and thus HRV is a significant indicator to access physical condition, especially cardiac health. IBI, which is the time interval between individual heartbeats, is used to measure the HRV. Officially, the R-R interval time series in ECG is recommended as the reference IBI. Furthermore, the J-J interval time series in BCG has also been successfully validated as IBI for HRV analysis during post-exercise conditions [114].

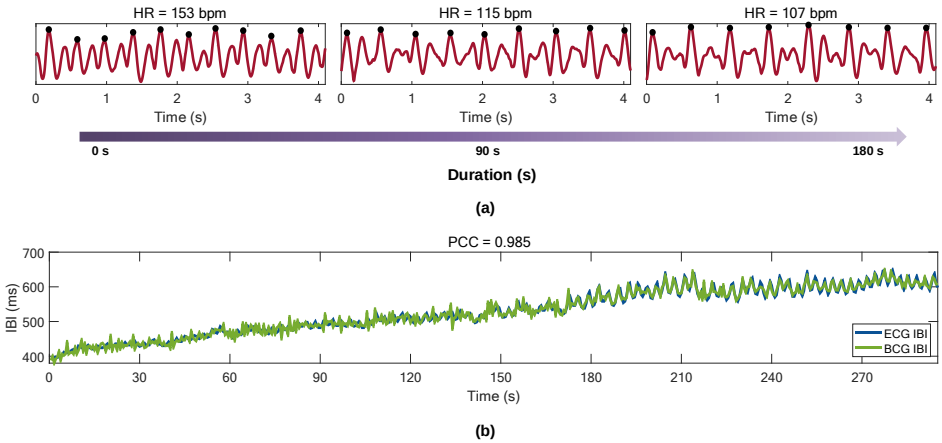

Fig. 4.10. The reconstructed post-exercise BCG segments during 3 minutes. (b) The post-exercise IBI variation of BCG and ECG during 5 minutes.

Exercise is a noninvasive method to alter the time interval of heartbeats and is widely used in HRV analysis experiments [115]. In our work, we conducted the experiment of post-exercise BCG signals collection to test the performance of the model in variational IBI reconstruction. During data collection, one subject whose BCG data were not included in the basic dataset, was asked to run for 3 minutes. After that, the post-exercise BCG and ECG signals were collected simultaneously for 5 minutes by the sensors. Totally, we collected 554 heartbeats, and among them, 551 heartbeats were successfully reconstructed. Three segments of reconstructed post-exercise BCG segments are shown in Fig. 4.10(a). It can be found that the HR drops gradually from 153 bpm to 107 bpm after 3 minutes. Figure. 4.10(b) shows the post-exercise IBI variation of BCG and ECG in 5 minutes, of which the R-R time interval in the ECG is used as the reference IBI. The PCC between the BCG IBI variation and ECG IBI variation is 0.985, which shows the reconstructed IBI variations are close to the reference values.

4.7 Summary

In this chapter, we have presented a BCG reconstruction algorithm based on the modified pix2pix GAN, which can retrieve BCG signals by solving signal fading problems in the MZI without using any additional hardware. This model greatly reduces the cost and complexity of the BCG monitoring system. The reconstructed BCG signals in the test data achieve satisfying results, of which the mean PCC, PRD, b_x, and MAE are 0.952, 29.875, 0.920, and 0.094, respectively. In addition, we collected special BCG data including sinus arrhythmia data and post-exercise data, and the model can reconstruct these BCG data in high performance. The BCG reconstruction algorithm creatively solves the signal fading problem in the interferometer, and it could be further applied in related applications, such as pulse waves reconstructed from the interferometer.

Chapter 5

Compressed sensing framework for ballistocardiography monitoring based on the optical fiber sensor

5.1 Introduction

Long-term and real-time services are essential for heartbeat monitoring whether in the clinic or at home. They can provide early detection of CVDs and avoid severe cardiovascular events. Benefiting from the development of information technology, vital signs sensors can be integrated with the internet of things (IoT) systems to monitor the physiological status, which is called the internet of medical things (IoMT) systems. The sensors can monitor the vital signs such as heartbeat, breathing, and temperature from users continuously and transmit these data to remote facilities for further analysis. However, long-term monitoring can produce a lot of data, and IoMT systems need to collect and store data from abundant sensors, which both results in high pressure on the transmission systems. Thus, it is necessary to develop signal compression algorithms for BCG signals.

CS is a new signal sampling technique, which can efficiently acquire signals with a fewer sampling rate and reconstruct the signals by utilizing its intrinsic sparsity [116]. The traditional Shannon sampling theorem requires a higher sampling, which results in the requirement of a larger data rate. CS overcomes this problem subjecting to certain conditions. Compared to other compression methods, CS moves the computational load from sensors to the receiving end, which is typically located on the Internet cloud with great computational resources. Reconstruction algorithms of CS can be carried out in the cloud, and thus reduces the hardware complexity and energy consumption of sensors with constrained resources. Benefiting from this, CS is widely used for data compression in IoT systems. In recent years, there are various research related to physiological signal compression based on CS. For example, Xiao et al. adopt an improved segmented weak OMP algorithm for compression and reconstruction of ECG and PPG [117]. Chen et al. propose a two-stage reconstruction method to recover heart sound signals [118]. However, there are few studies about BCG signal compression based on CS. Therefore, we prepare to design a CS framework for BCG signals based on the optical fiber sensor.

CS consists of data acquirement, compression, and reconstruction. In the first step, signals are obtained and compressed simultaneously through the sensing matrix at the sensing end, and then transmitted to the receiving end. Low computational complexity is needed since only a matrix multiplication is conducted at the sensing end. In the second step, different reconstruction algorithms are used to recover signals at the receiving end. Traditional

reconstruction algorithms can be broadly divided into three types: greedy algorithms, convex optimization algorithms, and Bayesian learning algorithms [119]. The principle of most traditional reconstruction algorithms is to search for the optimal solution iteratively according to prior knowledge. These algorithms are time-consuming and require an assumption about the structure of signals, which are not suitable for real-time performance. Therefore, fast algorithms are developed to reconstruct the compressed signals [120]. Currently, data-driven deep learning models have also been applied to address these problems, which can support real-time monitoring [121].

In this chapter, the principle of CS, as well as three key components including sparse representation, measurement matrices, and reconstruction algorithms are introduced. To verify the reconstruction performance in the BCG signals based on the traditional algorithms, several reconstruction algorithms including BP, OMP, and BSBL are applied. Finally, an end-to-end deep learning-based reconstruction method for reconstructing BCG signals is proposed. The results show that the deep learning model can perform well when the CR ranges from 50% to 95%.

5.2 Compressed sensing

5.2.1 Principle

The traditional signal sampling frequency should be subject to the Nyquist sampling theorem, which requires the sampling rate to be at least twice the highest frequency of the measurement signal to guarantee faithful

representation and reconstruction. However, this traditional signal acquisition technique has met some challenges. For example, in many situations, the frequency of measurement signals is so large that the DAQ cards cannot bearable. Even for signals with low frequency, such as heartbeat signals, the Nyquist sampling rate will produce a lot of redundant information, which increases the burden of wireless transmission.

CS is a novel signal acquisition technique, and it can reconstruct signals using a sampling rate far below the frequency of Nyquist sampling based on the sparsity of the detected signals. A basic noisy model can be given as

$$\boldsymbol{y} = \boldsymbol{\Phi x} + \boldsymbol{v}, \tag{5.1}$$

where $\boldsymbol{x} \in \mathbb{R}^{N\times 1}$ is the measurement signal and its dimension is N. $\boldsymbol{\Phi} \in \mathbb{R}^{M\times N}(M \ll N)$ is the measurement matrix, which is designed to linearly compress x. In the $\boldsymbol{\Phi}$, any M columns are linearly independent. $\boldsymbol{v}$ is the noise introduced by the CS system. In our case, $\boldsymbol{x}$ is the segment of obtained BCG signals from the optical fiber sensor. $\boldsymbol{y}$ is the compressed signal with the dimension of M and transmitted by the IoMT to the receiving end. Since $\boldsymbol{v}$ can be ignored in our case, the model can be reduced to

$$\boldsymbol{y} = \boldsymbol{\Phi x}. \tag{5.2}$$

For many measurements, most natural signals are not sparse in practice. The signal can be transformed into the sparse domain by some transform algorithms, such as Fourier transform and wavelet transform. Therefore, $\boldsymbol{x}$ can be described as

$$\boldsymbol{x} = \boldsymbol{\Psi\theta}, \tag{5.3}$$

where $\boldsymbol{\Psi} \in \mathbb{R}^{N\times N}$ is an orthonormal basis matrix of the selected transformed domain and $\boldsymbol{\theta}$ is a sparse vector with N dimension. For example, heartbeat signals can be expressed by a linear superposition of an orthonormal wavelet basis with S elements. The equation can be given by $\boldsymbol{x} \approx \sum_{k=1}^{S} \theta_k \, {\Psi_k}^2$, where $S \ll N$ and Ψ_k is the wavelet basis. Thus, Eq. (5.2) can be rewritten as

$$\boldsymbol{y} = \boldsymbol{\Phi\Psi\theta} = \boldsymbol{\Omega\theta}, \tag{5.4}$$

where $\boldsymbol{\Omega} \triangleq \boldsymbol{\Phi\Psi}$ is called a sensing matrix. As mentioned above, $\boldsymbol{\theta}$ is a sparse vector, and thus the CS algorithm can reconstruct $\boldsymbol{\theta}$ based on the $\boldsymbol{y}$ and $\boldsymbol{\Omega}$. Finally, $\boldsymbol{x}$ can be reconstructed by Eq. (5.3).

To ensure that the *S*-sparse vector θ can be efficiently reconstructed by $\boldsymbol{y}$ and $\boldsymbol{\Omega}$, the sensing matrix $\boldsymbol{\Omega}$ must satisfy the restricted isometry property (RIP),

$$(1 - \delta_S)\|\boldsymbol{\theta}\|_2 \leq \|\boldsymbol{\Omega\theta}\|_2 \leq (1 + \delta_S)\|\boldsymbol{\theta}\|_2, \tag{5.5}$$

for all *S*-sparse vectors $\boldsymbol{\theta}$. δ_S is the isometry constant and it must be not too close to 1. The RIP ensures that the most important *S* components of the original sparse signal $\boldsymbol{\theta}$ are recorded, and the energy of the original signal can be transferred to the sampled signal $\boldsymbol{y}$.

Since Eq. (5.4) is an underdetermined equation, it has infinitely many solutions. Among all the solutions, the sparsest solution is the desired reconstructed signal. Therefore, the problem of solving the equation $\boldsymbol{y} = \boldsymbol{\Phi x}$ can be transformed into the minimum 0-norm problem:

$$min\|\boldsymbol{\theta}\|_0 \quad \text{subject to} \quad \boldsymbol{\Omega\theta} = \boldsymbol{\Phi\Psi\theta} = \boldsymbol{y}. \tag{5.6}$$

Actually, the signal reconstruction issue in the CS is equivalent to the sparse decomposition problem, so the existing algorithms of sparse decomposition can be applied to the CS signal reconstruction.

CS theory mainly includes three parts: sparse representation of signals, design of the measurement matrices, and signal reconstruction algorithms.

5.2.2 Sparse representation

A signal is sparse in one domain when it comprises largely zero entries in that domain. For a sparse signal, zero entries can be effectively discarded, and the relevant signal information will not lose. The signal is considered to be *S*-sparse if it has *S* nonzero elements in a sparse signal. For a signal of length *N*, $N - S$ signal coefficients can be deleted while the significant information of the signal is preserved.

Most natural signals are not sparse in practice. Therefore, different transformation methods such as Fourier transform, discrete cosine transform (DCT), and wavelet transform are adopted to find out the features of the signal and represent them sparsely. Then, a set of basis in the transformed space is used to represent the signal, the decomposition coefficients of which show the degree of energy concentration or sparsity of the signal. The transformation of the signal in the orthogonal space $\boldsymbol{\Psi}$ can be expressed as $\boldsymbol{S} = \boldsymbol{\Psi}^T \boldsymbol{x}$. $\boldsymbol{S}$ is sparse when the formula can be satisfied:

$$\|\boldsymbol{S}\|_p = \left(\sum_i |s_i|^p \right)^{1/p} \leq R, \tag{5.7}$$

where $0 < P < 2$ and $R > 0$. How to find the best signal sparse representation is the key to CS theory and application. Using an appropriate

basis to represent the signal can guarantee the sparsity of the signal and also the accuracy of the reconstructed signals.

5.2.3 Measurement matrices

Random matrices, such as random matrices with independent and identically distributed, are universally appropriate choices for the measurement matrix. It is found that a simple pseudorandom design can be used to fabricate several efficient measurement matrices, which own low computational power and is suitable for embedding in the sensing end. Currently, there are some commonly used measurement matrices including random Gaussian matrix, random Bernoulli matrix, partial Hadamard matrix, and sparse random matrix.

1. Random Gaussian matrix

The random Gaussian matrix is the most extensively used measurement matrix. The distribution of each element in the matrix is independent of each other and satisfies the Gaussian distribution with the mean value of 0 and the variance of $1/M$. Therefore, the $M \times N$ matrix can be expressed as

$$\boldsymbol{\Phi}_{i,j} \sim N\left(0, \frac{1}{M}\right). \tag{5.8}$$

The RIP property of the Gaussian random matrix can be satisfied when M meets the following formula:

$$M \geq cS \log\left(\frac{N}{S}\right), \tag{5.9}$$

where c is a small constant and S is the sparsity of the original signal.

2. Random Bernoulli matrix

In a random Bernoulli matrix, each element is subject to the Bernoulli distribution, which can be shown as

$$\Phi_{i,j} = \begin{cases} +\frac{1}{M} & P = \frac{1}{2} \\ -\frac{1}{M} & P = \frac{1}{2} \end{cases} = \frac{1}{M} \begin{cases} +1 & P = \frac{1}{2} \\ -1 & P = \frac{1}{2} \end{cases}, \tag{5.10}$$

where P is the probability. As a discrete probability distribution, the random Bernoulli matrix realizes the randomness of the measurement matrix with great probability, thus satisfying the randomness of the process of CS. When M satisfies Eq. (5.9), it can satisfy RIP.

3. Partial Hadamard matrix

The partial Hadamard matrix is created by randomly selecting several rows from the Hadamard matrix. Hadamard matrix is an orthogonal square matrix, in which any two rows or columns of the matrix are orthogonal, and the determinant of the matrix is ± 1. The sum of squares of all elements in any row or column is equal to the order of the square matrix, which can be given by

$$\boldsymbol{A}\boldsymbol{A}^T = N\boldsymbol{E}, \tag{5.11}$$

where $\boldsymbol{A}$ is the Hadamard matrix and $\boldsymbol{A}^T$ is the transpose of $\boldsymbol{A}$. $\boldsymbol{E}$ is the identity matrix. N is the order of the matrix. For N^{th}-order Hadamard matrices, N needs to satisfy the following conditions,

$$N = 2^k, \tag{5.12}$$

where k is a positive integer. After the Hadamard matrix is constructed, random functions are used to extract M rows from N rows randomly, which is a partial Hadamard matrix.

4. Sparse random matrix

The sparse random matrix owns a simple structure, which makes it more suitable for hardware devices with limited computation. To obtain a sparse

random measurement matrix, an empty matrix with a dimension of $M \times N$ is built, and then L elements in each column are selected randomly to set to 1, and the remaining $M - L$ elements are set to 0.

5.2.4 Reconstruction algorithms

Signal reconstruction is to use the M-dimension measurement signal $\boldsymbol{y}$ and measurement matrix $\boldsymbol{\Phi}$ to reconstruct the N-dimension original signal $\boldsymbol{x}$ by a reconstruction algorithm. Currently, the widely used reconstruction algorithms in CS can be divided into convex optimization algorithms, greedy algorithms, and Bayesian learning algorithms, which are shown in the following.

1. Convex optimization algorithms

In Eq. (5.6), an optimal solution can be obtained only by giving all possible linear combinations of C_N^S positions of non-zero terms in $\boldsymbol{\theta}$. Therefore, the solution of Eq. (5.6) belongs to the NP-hard problem. The BP algorithm is a type of convex optimization algorithm [122], which converts the 0-norm problem into a simpler 1-norm minimum optimization problem. Therefore, Eq. (5.6) can be changed into

$$min\|\boldsymbol{\theta}\|_1 \quad \text{subject to} \quad \boldsymbol{\Omega\theta} = \boldsymbol{\Phi\Psi\theta} = \boldsymbol{y}. \tag{5.13}$$

Thus, the sparse signal reconstruction problem becomes a convex optimization problem.

2. Greedy algorithms

The 1-norm minimization algorithm is not the only method to find sparse solutions. Greedy algorithms, such as matching pursuit (MP) and OMP, have also been proposed to solve this problem [123]. These algorithms greatly save

calculation time and are easy to implement. We set $\boldsymbol{\Omega} = [\boldsymbol{b_1}, \boldsymbol{b_2}, \dots, \boldsymbol{b_N}]$, of which $\boldsymbol{b_i}$ is called as the basis or atoms. The algorithm first searches for $\boldsymbol{b_i}$ that has the maximum correlation with measurements $\boldsymbol{y}$. Then, in each iteration, it looks for $\boldsymbol{b_i}$ with maximum correlation with the current residual. The estimation of the signal vector is updated according to the index of $\boldsymbol{b_i}$ which has the highly correlation with the current residual. The vectors are updated iteratively until the set number of iterations is reached or the residual is less than the set threshold.

3. Bayesian learning algorithms

Most natural signals have a complex structure, and the block structure is one of the common structures in natural signals [124]. A sparse signal $\boldsymbol{x}$ with block structure can be considered as a collection of blocks, which can be shown as

$$\boldsymbol{x} = \left[x_1, \dots, x_{h1}, \dots, x_{h_{g-1}+1}, \dots, x_{h_g}\right]^T, \tag{5.14}$$

$$\begin{cases} \boldsymbol{x_1} = [x_1, \dots, x_{h1}]^T. \\ \dots \\ \boldsymbol{x_g} = \left[x_{h_{g-1}+1}, \dots, x_{h_g}\right]^T. \end{cases}$$

where $\boldsymbol{x_i} \in \mathbb{R}^{h_i \times 1}$, and $h_i (i = 1, \dots, g)$ are not necessarily identical. Only a few blocks in the sparse signal are nonzero. A signal with this block structure is defined as a block sparse signal. Utilizing this block structure can further improve the reconstruction result.

For a block sparse signal, the BSBL framework models each block $\boldsymbol{x_i} \in \mathbb{R}^{h_i \times 1}$ as a parameterized multivariate Gaussian distribution:

$$p(\boldsymbol{x_i}; \gamma_i; \mathbf{B}_i) \sim \mathcal{N}(0, \gamma_i \mathbf{B}_i), \;\; i = 1, \dots, g. \tag{5.15}$$

where γ_i is a non-negative parameter, which can control the block-sparsity of the signal. $\gamma_i = 0$ represents that the i^{th} block, $\boldsymbol{x_i}$, is a zero block. $\mathbf{B}_i \in \mathbb{R}^{h_i \times h_i}$ is a positive-definite matrix and it can capture the correlation structure of the block $\boldsymbol{x_i}$. Assuming that blocks are uncorrelated to one another, Eq. (5.15) can be rewritten as $p(\boldsymbol{x}) \sim \mathcal{N}(\mathbf{0}, \boldsymbol{\Sigma_0})$, where $\boldsymbol{\Sigma_0}$ is a block-diagonal matrix, in which the i^{th} principal block is equal to $\gamma_i \mathbf{B}_i$. The noise vector is assumed to follow the multivariate Gaussian distribution and it can be shown as $p(\mathbf{v}) \sim \mathcal{N}(\mathbf{0}, \lambda \mathbf{I})$, where λ is a positive scalar and $\mathbf{I}$ is an identity matrix. Therefore, the block sparse signal can be obtained by estimating all parameters of $\{\gamma_i \mathbf{B}_i\}_1^g$ and λ based on the maximum-a-posterior estimation, and it is commonly done with the Type-II maximum likelihood estimate method [125].

Three iterative algorithms have been proposed and derived to recover the signal, including the expectation-maximization method (BSBL-EM), the bound-optimization method (BSBL-BO), and a hybrid of BSBL and group-lasso type algorithms (BSBL-*l*1). The BSBL-BO has been applied to reconstruct the fetal ECG and achieve a great performance [126]. The algorithm can reconstruct the non-sparse signal by setting a γ_i -pruning threshold to a small value. In addition, BSBL-BO and other derived algorithms from [125] can explore and exploit the correlation structure in each block $\boldsymbol{x_i}$ by estimating the matrices $\mathbf{B}_i$, which further improves the reconstruction performance.

5.3 Performance evaluation of traditional reconstruction algorithms in BCG signals

5.3.1 Method

Currently, most research on CS for biomedical sequence signals is related to ECG, PPG, and EEG, while there are few works about the CS framework for BCG signals. Therefore, we first verify the CS performance on BCG based on several traditional reconstruction algorithms. In the experiment, the DCT is used to convert BCG signals into the sparse domain. The random sparse matrix is adopted as the measurement matrix. According to the different CRs, corresponding measurement matrices are designed, and two examples with CR of 50% and 80% are shown in Fig. 5.1.

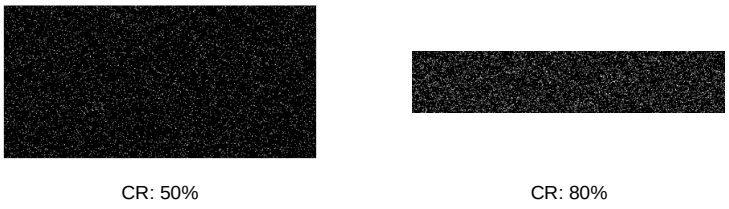

Fig. 5.1. Measurement matrices with CR of 50% and 80%.

To explore the performance of reconstruction algorithms in BCG signals, we have referred to different studies of reconstruction algorithms in the biomedical sequence signal mentioned before. Four kinds of commonly used reconstruction algorithms are chosen to investigate the reconstructed performance in BCG signals, which are BP, OMP, BSBL-BO, and BSBL-FM. As introduced in the last section, BP and OMP are based on the convex optimization method and the greedy algorithm, respectively. BSBL-BO and BSBL-FM are based on Bayesian learning algorithms. BSBL-BO uses the

bound-optimization method to minimize the cost function while BSBL-FM adopts the fast marginalized (FM) likelihood maximization method, which is a fast algorithm. The algorithms are all implemented in MATLAB, among which the CVX toolbox is used to solve the convex optimization issue.

The performance evaluation process of CS reconstruction algorithms consists of four steps: signal sparse representation, signal compression, signal reconstruction, and performance evaluation. Each step contains several sub-steps, and the workflow is shown in Fig. 5.2. In step 1, BCG data are converted into a sparse domain based on the DCT. In step 2, the measurement matrices based on the sparse random matrices with different values of CRs are used to sample the signal. In step 3, several reconstruction algorithms including BP, OMP, BSBL-BO, and BSBL-FM are used to recover compressed signals. In step 4, three metrics are adopted to evaluate the performance of reconstruction under different CRs.

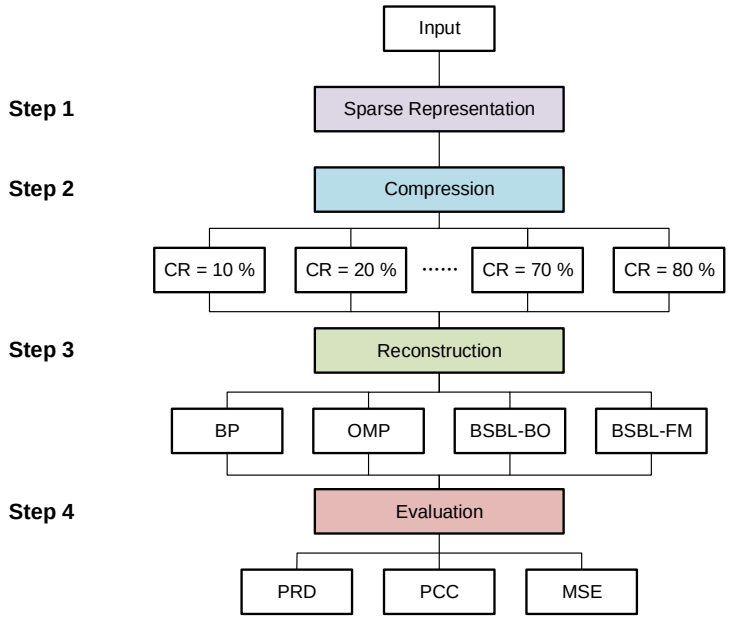

Fig. 5.2. The workflow of CS.

5.3.1 Evaluation method

CR is the measure of the decrease in data required to express a signal. For CS, it is a ratio between the lengths of the original and compressed signal vectors, which means that the measurement with a fewer dimension of M can accurately reconstruct the original signal. CR can be defined as

$$CR = \frac{N - M}{N} \times 100. \tag{5.16}$$

where N is the length of the original signal and M is the dimension of the compressed signal.

To evaluate the performance of reconstruction algorithms, we obtain compressed BCG signals with different CRs and use PRD, PCC, and MSE to evaluate the error between reconstruction signals and original signals.

5.3.2 Result and discussion

In this experiment, we collect 2874 segments of BCG signals from our MZI-based BCG monitor with a phase compensation system. Each segment has 512 sampling points, and the sampling rate is 250 Hz. The CR ranges from 10% to 90% and increases by a gradient of 10%. The average PRD, PCC, and MSE of each record recovered by four types of reconstruction algorithms under different CRs are shown in Fig.5.3. It can be found that BSBL-BO and BSBL-FM outperform other reconstruction algorithms. With the increase of CR from 10% to 80%, the PRD, PCC, and MSE of BSBL-BO and BSBL-FM change in an acceptable range. For BP and OMP, when the CR is low than 70%, they present good results. However, when the CR reaches 80%, the performance of reconstruction results dramatically decreases. The

reconstruction waveform of BP and OMP with the CR of 80% are shown in Fig. 5.4(a) and (b).

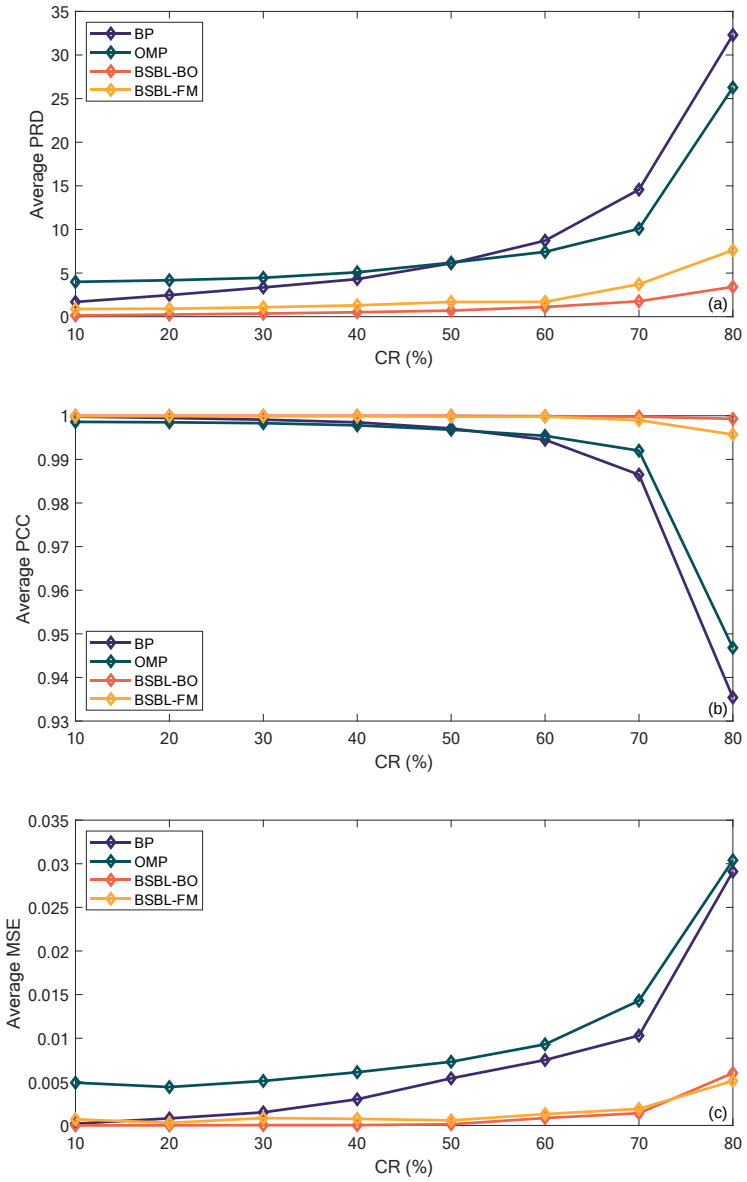

Fig. 5.3. The average (a) PRD, (b) PCC, and (c) MSE based on four types of reconstruction algorithms under different CRs.

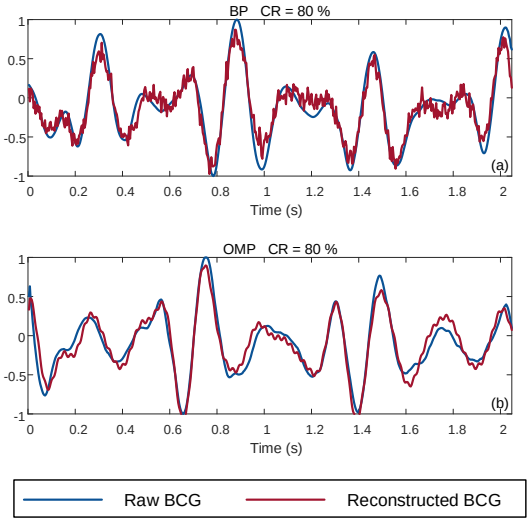

Fig. 5.4. Reconstruction results by (a) BP and (b) OMP under CR of 80%.

The reconstruction results of BSBL-BO and BSBL-FM under the CR of 80% are shown in Fig. 5.5(a) and (b), in which the BCG waveform can be recovered successfully by these two algorithms. Though the performance of BSBL-FM is slightly worse than that of BSBL-BO when CR ranges from 10% to 80%, the BSBL-FM is dozens of times fast than the BSBL-BO, which is more suitable for a real-time monitoring system. However, in the experiment, we found that when the CR increases up to 90% or more, the performance of these two algorithms deteriorates dramatically, especially BSBL-FM. The examples are shown in Fig. 5.6(a) and (b), where are the reconstruction results from BSBL-BO and BSBL-FM with CR equaling 93%. Therefore, to solve the problem in the CS signal reconstruction with a high CR, we propose to use an end-to-end deep learning model to reconstruct BCG signals.

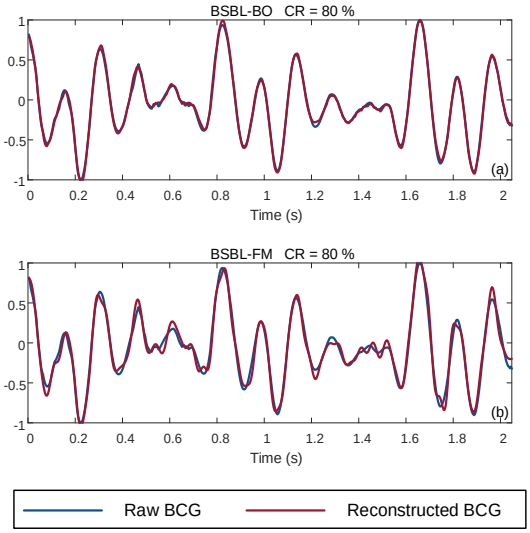

Fig. 5.5. Reconstruction results by (a) BSBL-BO and (b) BSBL-FM under CR of 80%.

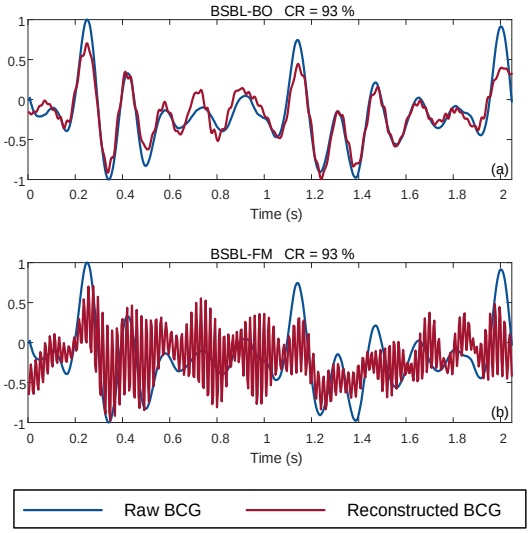

Fig. 5.6. Reconstruction results by (a) BSBL-BO and (b) BSBL-FM under CR of 93%.

5.4 Deep learning model-based reconstruction algorithms for BCG reconstruction with a high CR

5.4.1 Method

Traditional CS reconstruction algorithms are based on iteration and need more running time, which is not suitable for a real-time monitoring system. Though the fast reconstruction algorithm BSBL-FM can solve this problem,

its performance in the high CR, such as CR over 90%, is poor. Inspired by our previous works, we proposed to use an end-to-end deep learning model to reconstruct the compressed BCG signals. The compression and reconstruction process can be divided into two steps. In step 1, a sparse random matrix with a size of $M \times N$ is adopted as the measurement matrix to sample and compress BCG signals simultaneously. In step 2, an end-to-end deep learning model is used to reconstruct the compressed BCG signals.

The architecture of the deep learning model is shown in Fig. 5.7. It is an end-to-end model, which means that the compressed signals can be directly input into the model. The proposed deep learning model consists of an FCL and a modified U-net network. The FCL is used to map the compressed signal from M dimension to N dimension. The activation function of FCL is tanh, which outputs the value from -1 to 1. It can speed up the following training process and improve the accuracy of the model. The feature map with the size of $N \times 1$ is then fed into a modified U-net, which can reconstruct the BCG signals. The architecture of the U-net is modified from our previous work in chapter 3. We have conducted a series of experiments to optimize the hyper-parameters in the neural network. Compared to our previous network, we use a larger kernel size of 25×1 to extract features in the raised-dimension signals. The number of filters (n_f) is 64, which doubles at each down-sampling stage while halves at each up-sampling stage. The activation function in the 1-D convolutional layers is ReLU except for the last output layer, in which we do not use any activation function.

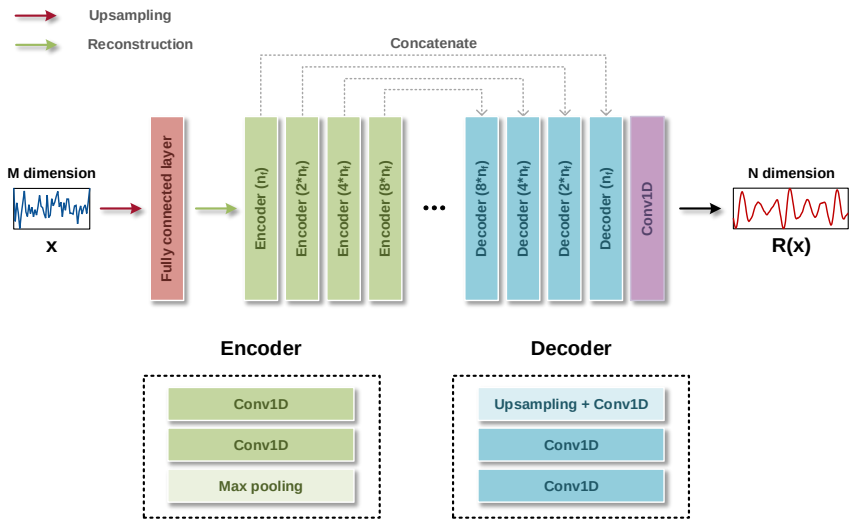

Fig. 5.7. The architecture of the CS reconstruction algorithm.

To train the network, we have collected 14370 segments from our MZI-based BCG monitor with a phase compensation system. Each segment owns 512 sampling points, and the sampling rate is 250 Hz. The ratio between the training, validation, and test sets is 6, 2, and 2. Adam optimization method [49] with default parameters (learning rate: 0.001, beta-1: 0.9, beta-2: 0.99) is used as the optimizer. MSE is used as the loss function, and mini-batch gradient descent is adopted, in which the batch size is 16.

5.4.2 Result and discussion

In the experiment, we first use BCG signals with the CR ranging from 50% to 90% to verify the reconstruction performance of the deep learning model. The average PRD, PCC, and MSE in the test data are shown in Fig. 5.8, in which results from BSBL-BO, and BSBL-FM are used as the reference. The CR increases from 50% to 90% here since the performances of traditional reconstruction algorithms are good enough in the low CR. When the CR is in the range of 50% to 70%, the performances of BSBL-BO and BSBL-FM are

slightly better than the proposed deep learning model, especially for the PRD. When the CR is large than 80%, the performance of BSBL-BO and BSBL-FM declines noticeably while the performance of the deep learning model is still good. In addition, the running time of the deep learning model is much shorter than that of BSBL-BO. In general, the proposed deep learning model can give satisfying results with the CR ranging from 50% to 90%.

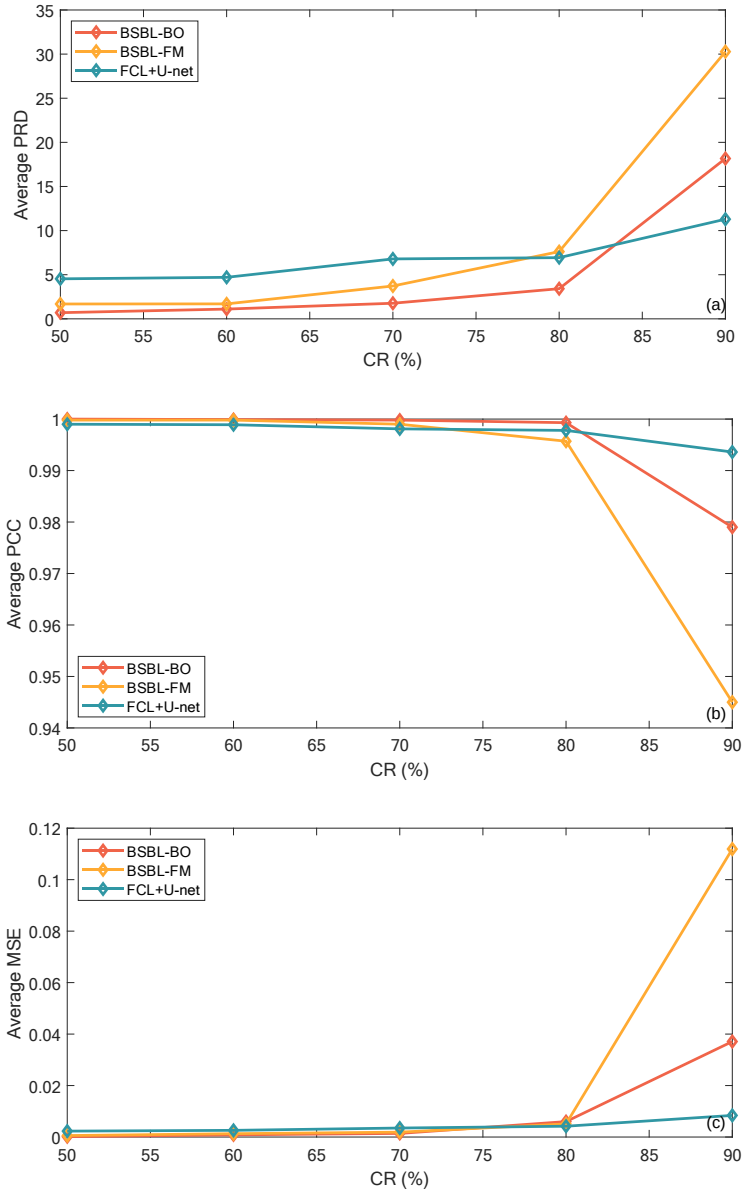

Fig. 5.8. The average PRD, PCC, and MSE in the test data by three types of reconstruction algorithms under different CRs.

The average PRD, PCC, and MSE of reconstruction results in the test set using the deep learning model with the CR exceeding 90% are shown in Table. 5.1. The comparison results using BSBL-BO and BSBL-FM are shown in Table 5.2. We only show the reconstruction results from BSBL-BO and BSBL-FM with CR ranging from 91% to 93% since the results are poor when CR is over 93%. It can be found that the deep learning model outperforms BSBL-BO and BSBL-FM in the high CR.

Table. 5.1. The average PRD, PCC, and MSE of reconstruction results in the test set using the deep learning model with the CR exceeding 90%.

CR	PRD	PCC	MSE
91%	12.542	0.992	0.007
92%	15.309	0.987	0.012
93%	20.193	0.978	0.018
94%	23.593	0.968	0.019
95%	28.284	0.954	0.034
96%	36.680	0.920	0.039

Table. 5.2. The average PRD, PCC, and MSE of reconstruction results in the test set using BSBL-BO and BSBL-FM with the CR exceeding 90%.

CR	BSBL-BO			BSBL-FM		
	PRD	PCC	MSE	PRD	PCC	MSE
91%	19.768	0.976	0.034	30.395	0.943	0.045
92%	27.679	0.951	0.106	32.256	0.939	0.170
93%	35.634	0.917	0.053	97.223	0.391	0.340

The reconstructive BCG waveforms using the deep learning model with CR from 91% to 96% are shown in Fig. 5.9(a) to (f). From these figures, we can find that though PCC reduces and the PRD/MSE increases with the

increase of CR, the IJK complex in the BCG can still be reconstructed. The change in evaluation indicators is mainly from the not-so-good recovery results of the non-IJK complex. It is quite different from the other cases based on traditional algorithms, in which the performance is poor for both the IJK complex and the non-IJK complex with a high CR. The IJK complex can be used in the HR and HRV calculation, which is more important than the other waves. The MAE of HR in the test data with CR increasing from 91% to 96% is shown in Table. 5.3. It can be found that with the CR below 95%, the MAE of HR is less than 1 bpm.

In addition, we use MSE as the loss function to train the neural network in this experiment. The model optimizes the parameters only depending on this metric. To further improve the result, we will attempt to design a combinative loss function to train the model.

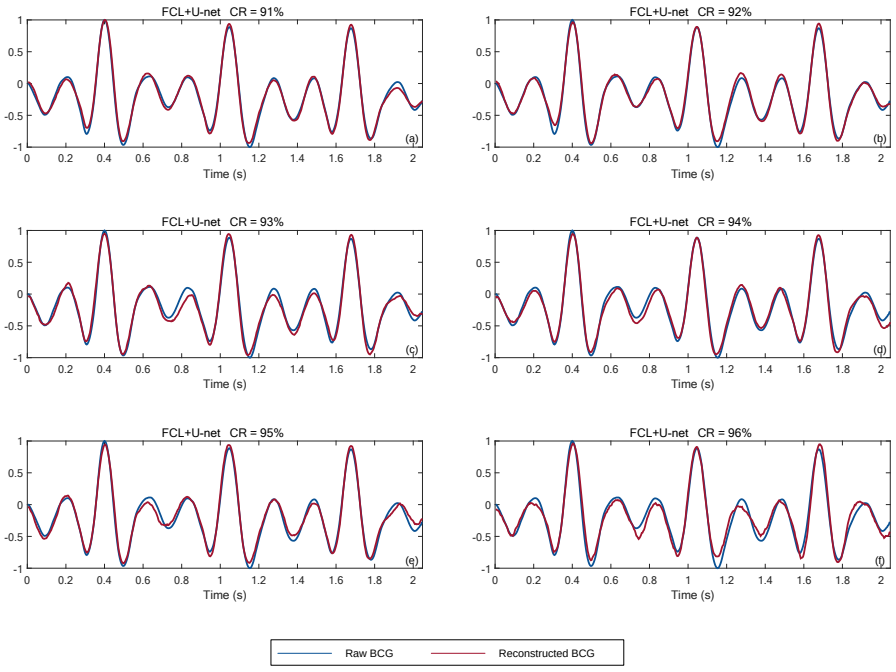

Fig. 5.9. The reconstruction results of deep learning model under different CRs: (a) 91%, (b) 92%, (c) 93%, (d) 94%, (e) 95%, and (f) 96%.

Table. 5.3. The MAE of HR in the test data with CR increasing from 91% to 96%.

CR	91%	92%	93%	94%	95%	96%
MAE/bpm	0.258	0.272	0.331	0.542	0.715	1.641

5.5 Summary

In this chapter, we propose a CS framework for BCG signals. Four types of traditional CS reconstruction algorithms, BP, OMP, BSBL-BO, and BSBL-FM are used to verify the reconstruction performance in the BCG signals with different CRs. Among them, BSBL-BO and BSBL-FM algorithms outperform BP and OMP algorithms. When CR is over 90%, the performances of traditional reconstruction algorithms decline significantly. Therefore, we proposed an end-to-end deep learning model to reconstruct BCG, which contains consists of an FCL and a modified U-net network The performance of the model is good when CR ranges from 50% to 90%. For the high CR exceeding 90%, though the performance is slightly degraded, the IJK complex in the BCG can be reconstructed and the MAE of HR is less than 1 bpm when the CR is below 95%.

Chapter 6

Conclusion and future works

6.1 Conclusion

In this thesis, we solve the signal fading problem in the optical fiber interferometer-based BCG monitoring system with a new type of phase shifter. Based on this BCG monitoring system, three deep learning algorithms including CNN, U-net, and pix2pix GAN are adopted to process the BCG signal and optimize the sensing system.

Firstly, we propose a new type of phase shifter, a moving-coil transducer, to compensate for the phase drift in the optical fiber interferometer-based BCG monitoring system. The proposed phase shifter maintains the optical fiber interferometer at Q-point with the aid of a PID controller, which solves the signal fading problem and high-quality BCG signals can be acquired. Compared to traditional phase modulation and demodulation schemes, such as 3×3 coupler and PGC interrogation schemes, our scheme owns the merits of low cost, easy integration, and fast response. The suggested BCG monitoring system can provide users with long-term, real-time and consistent

BCG monitoring, which has huge implications for future healthcare applications.

Secondly, we proposed two deep learning algorithms, CNN and U-net, to solve the issue of individual heartbeat segment extraction in the BCG signal. As the BCG signal is easy to be interfered with by the motion artifact and ambient noise during the measurement, effective individual heartbeat segments detection algorithm in the BCG signal is crucial for further HR analysis and CVDs diagnosis. We first use a CNN model to distinguish the induvial heartbeat segments, IJK complex, from the background (non-IJK complex), and body movement signals. The accuracy of the model in the test set is 98.3%, which shows that the network performs well on this classification task. Since this model needs a series of pre-processing works, which is time-consuming and cannot be implemented in a real-time BCG monitoring system, we propose an end-to-end algorithm to replace it. This end-to-end algorithm is based on a modified U-net, which can segment IJK complex, background, and body movement signals in a BCG segment. BCG signals from 7 healthy subjects are used to test the network, and the PA, MPA, and MIOU are 99.66%, 99.59%, and 99.18%. The MAE of the predicted IK interval is 1.75 ms. The results show that our proposed network owns good performance in the task of individual heartbeat segments extraction, and this end-to-end algorithm can be integrated into the real-time BCG monitoring system in the future.

Thirdly, we present a BCG reconstruction algorithm based on a modified pix2pix GAN, which can recover BCG signals by solving signal fading

problems in the interferometer without any additional phase modulation and demodulation devices. The cost and complexity of the BCG monitoring system are considerably reduced with this reconstruction algorithm-based scheme. In the test data, the reconstructed BCG signals produce satisfactory results, with mean PCC, PRD, bx, and MAE of 0.952, 29.875, 0.920, and 0.094, respectively. In addition, we have collected special BCG data including sinus arrhythmia and post-exercise samples, and the model can reconstruct these data with acceptable accuracy. The BCG reconstruction algorithm overcomes the signal fading problem in the interferometer in a novel way, and it could be used in other relevant applications as well, such as reconstructed pulse waves.

Finally, we propose to build a CS framework for the BCG signal. Four types of CS reconstruction algorithms, BP, OMP, BSBL-BO, and BSBL-FM are used to verify the reconstruction performance for BCG signals under different CRs. The BSBL-BO and BSBL-FM algorithms outperform the other two algorithms. Traditional reconstruction algorithms perform much worse when CR is large than 90%. As a result, we propose to develop an end-to-end model to reconstruct BCG, which contains an FCL and a modified U-net network. The performance of the model is good when CR increases from 50% to 90%. For the high CR over 90%, though the performance is slightly degraded, the IJK complex in the BCG can be reconstructed and the MAE of HR is less than 1 bpm when the CR is below 95%. For the CS scheme, only low computational complexity is needed at the sensing end and thus it can be applied in practical scenarios, such as a nursing house.

6.2 Future works

Based on the current monitoring system and research outcomes presented in this thesis, several extensive investigations about the application of deep learning models in BCG monitoring and the BCG signal processing are illustrated in this section.

1. The application of deep learning models in BCG monitoring.

As introduced in chapter 4, a modified pix2pix GAN is proposed to map BCG signals from an optical fiber MZI based on the intensity interrogation mode to reference BCG signals without signal fading problems. Among them, we use an MZI with a phase compensation system to collect reference signals. Reference BCG signals can also be obtained from the MZI with a 3×3 coupler interrogation scheme. Compared to the phase compensation scheme, the 3×3 coupler interrogation scheme can retain the respiration information in the BCG. A mapping model based on the deep learning model between the raw optical intensity and the demodulated result can be built to replace the complex hardware and algorithm in the 3×3 coupler interrogation scheme.

As introduced in chapter 5, a CS framework is built for the optical fiber interferometer-based BCG monitoring system. For high CRs, we propose a deep learning model to reconstruct BCG signals. MSE is adopted as the loss function to train the neural network in this experiment. The model optimizes the parameters only depending on this metric. To further improve the result, we can design a loss function to train the neural network, such as a loss function based on PCC. In addition, we prepare to use the sensor with a simpler structure, an MZI based on the intensity interrogation mode, as the

BCG monitor. To solve the signal fading problem in the intensity interrogation mode, we attempt to train the model based on that in chapter 5 by freezing the parameters in the previous layer to build a mapping model in the last few layers. This model can recover the compressed signal while solving the signal fading problem.

2. The application of deep learning models in BCG signal processing.

As introduced in section 1.5, the deep learning model can be used in various application scenarios, such as the detection of cardiovascular diseases, classification of sleep stages, and analysis of mental stress. Since HRV and respiration of subjects can be obtained by BCG, it can replace ECG in some of these application scenarios. For example, ECG can be used to classify the sleep stages based on HRV and respiration, and in this case, BCG may replace the function of ECG. Since BCG can be detected in a non-invasive and non-wearable way, it is more suitable for sleep monitoring compared to the ECG-based method, which gives the subject a comfortable monitoring environment.

Bibliography

[1] K, M. Namara, H. Alzubaidi, and J. K. Jackson, “Cardiovascular Disease as a Leading Cause of Death: How Are Pharmacists Getting Involved?” Integr. Pharm. Res. Pract. 8, 1-11 (2019).

[2] P. Kligfield, L. S. Gettes, J. J. Bailey, R. Childers, B. J. Deal, E. W. Hancock, G. V. Herpen, J. A. Kors, P. Macfarlane, D. M. Mirvis, O. Pahlm, P. Rautaharju, and G. S. Wagner, “Recommendations for the standardization and interpretation of the electrocardiogram: part I: the electrocardiogram and its technology a scientific statement from the American Heart Association Electrocardiography and Arrhythmias Committee, Council on Clinical Cardiology; the American College of Cardiology Foundation; and the Heart Rhythm Society endorsed by the International Society for Computerized Electrocardiology,” J. Am. Coll. Cardiol. 49(10), 1109-1127 (2007).

[3] S. A. Mascaro, and H. H. Asada, “Photoplethysmograph fingernail sensors for measuring finger forces without haptic obstruction,” IEEE Trans. Robot. Autom. 17(5), 698-708 (2001).

[4] O. T. Inan, P. F. Migeotte, K. S. Park, M. Etemadi, K. Tavakolian, R. Casanella, J. Zanetti, J. Tank, I. Funtova, G. K. Prisk, and M. D. Rienzo, “Ballistocardiography and seismocardiography: A review of recent advances,” IEEE J. Biomed. Health Inform. 19(4), 1414-1427 (2014).

[5] O. T. Inan, M. Etemadi, R. M. Wiard, L. Giovangrandi, and G. T. A. Kovacs, “Robust ballistocardiogram acquisition for home monitoring,” Physiol. Meas. 30(2), 169-185 (2009).

[6] J. Alametsä, A. Palomäki, and J. Viik, “Short and longer term repeatability of ballistocardiography in a sitting position with EMFi sensor,” Med. Biol. Eng. Comput. 49(8), 881-889 (2011).

[7] M. Liu, F. Jiang, H. Jiang, S. Ye, H. Chen, “Low-power, noninvasive measurement system for wearable ballistocardiography in sitting and standing positions,” Comput. Ind. 91, 24-32 (2017).

[8] M. A. Hassan, A. S. Malik, D. Fofi, N. M. Saad, Y. S. Ali, and F. Meriaudeau, “Video-based heartbeat rate measuring method using ballistocardiography,” IEEE Sens. J. 17(14), 4544-4557 (2017).

[9] O. Postolache, R. N. Madeira, P. S. Girão, and G. Postolache, “Microwave FMCW Doppler radar implementation for in-house pervasive health care system,” in IEEE International Workshop on Medical Measurements and Applications 2010, 47-52 (2010).

[10] C. Lu, J. Su, X. Dong, T. Sun and K. T. V. Grattan, “Simultaneous Measurement of Strain and Temperature With a Few-Mode Fiber-Based Sensor,” J. Light. Technol. 36(13), 2796-2802 (2018).

[11] H. Sun, S. Yang, X. Zhang, L. Yuan, Z. Yang, and M. Hu, “Simultaneous measurement of temperature and strain or temperature and curvature based on an optical fiber Mach–Zehnder interferometer,” Opt. Commun., 340, 39-43 (2015).

[12] X. Wu, X. Wang, S. Li, S. Huang, Q. Ge, and B. Yu, “Cantilever Fiber-Optic Accelerometer Based on Modal Interferometer,” IEEE Photonics Technol. Lett., 27(15), 1632-1635 (2015).

[13] H. Z. Yang, M. M. Ali, M. R. Islam, K-S. Lim, D. S. Gunawardena, and H. Ahmad, “Cladless few mode fiber grating sensor for simultaneous refractive index and temperature measurement,” Sensor Actuat. A-Phys. 228, 62-68 (2015).

[14] X. Yang, Z. Chen, C. S. M. Elvin, L. H. Y. Janice, S. H. Ng, J. T. Teo and R. Wu, “Textile Fiber Optic Microbend Sensor Used for Heartbeat and Respiration Monitoring,” IEEE Sens. J. 15(2), 757-761 (2015).

[15] Ł. Dziuda, M. Krej, and F. W. Skibniewski, “Fiber Bragg grating strain sensor incorporated to monitor patient vital signs during MRI,” IEEE Sens. J. 13(12), 4986-4991 (2013).

[16] R. G. Priest, “Analysis of Fiber Interferometer Utilizing 3 x 3 Fiber Coupler,” IEEE Trans. Microw. Theory Tech. 30(10), 1589-1591 (1982).

[17] D. A. Jackson, R. Priest, A. Dandridge, and A. B. Tveten, “Elimination of drift in a single-mode optical fiber interferometer using a piezoelectrically stretched coiled fiber,” Appl. Opt. 19, 2926-2929 (1980).

[18] Z. Ebrahimi, M. Loni, M. Daneshtalab, and A. Gharehbaghi, “A review on deep learning methods for ECG arrhythmia classification,” Expert Syst. Appl. 7, 100033 (2020).

[19] S. Chambon, M. N. Galtier, P. J. Arnal, G. Wainrib, and A. Gramfort, “A deep learning architecture for temporal sleep stage classification using multivariate and multimodal time series,” IEEE Trans. Neural Syst. Rehabilitation Eng. 26(4), 758-769 (2018).

[20] R. Katmah, F. Al-Shargie, U. Tariq, F. Babiloni, F. Al-Mughairbi, and H. Al-Nashash, “A Review on Mental Stress Assessment Methods Using EEG Signals,” Sensors, 21(15), 5043 (2021).

[21] J. W. Gordon, “Certain molar movements of the human body produced by the circulation of the blood,” J. Appl. Physiol. 11(Pt 3), 533-536 (1877).

[22] I. Starr, A. J. Rawson, H. A. Schroeder, and N. R. Joseph, “Studies on the estimation of cardiac output in man, and of abnormalities in cardiac function, from the heart’s recoil and the blood’s impacts; the ballistocardiogram,” Am. J. Physiol. 127(1), 1-28 (1939).

[23] C. S. Kim, S. L. Ober, M. S. Mcmurtry, B. A. Finegan, O. T. Inan, R. Mukkamala, and J. O. Hahn, “Ballistocardiogram: Mechanism and Potential for Unobtrusive Cardiovascular Health Monitoring,” Sci. Rep. 6, 31297 (2016).

[24] J. Williams, “Bridge Circuits: Marrying Gain and Balance,” Linear Technol. Appl. 43, 1-46 (1990).

[25] R. Gonzalez-Landaeta, O. Casas, and R. Pallas-Areny, “Heart rate detection from an electronic weighing scale,” Phys. Meas. 29(8), 979-988 (2008).

[26] J. H. Shin, K. M. Lee, and K. S. Park, “Non-constrained monitoring of systolic blood pressure on a weighing scale,” Phys. Meas. 30(7), 679-693 (2009).

[27] J. Alihanka, K. Vaahtoranta, and I. Saarikivi, “A new method for long-term monitoring of the ballistocardiogram, heart rate, and respiration,” Amer. J. Physiol. 240(5), R384–R392 (1981).

[28] A. Vehkaoja, S. Rajala, P. Kumpulainen, and J. Lekkala, “Correlation approach for the detection of the heartbeat intervals using force sensors placed under the bed posts,” J. Med. Eng. Technol. 37(5), 327-333 (2013).

[29] J. M. Kortelainen and J. Virkkala, “FFT averaging of multichannel BCG signals from bed mattress sensor to improve estimation of heart beat interval,” in 2007 29th annual international conference of the IEEE engineering in medicine and biology society, 6685-6688 (2007).

[30] J. Paalasmaa, M. Waris, H. Toivonen, L. Leppakorpi, and M. Partinen, “Unobtrusive online monitoring of sleep at home,” in 2012 annual international conference of the IEEE engineering in medicine and biology society, 3784-3788 (2012).

[31] F. Wang, M. Tanaka, and S. Chonan, “Development of a PVDF piezopolymer sensor for unconstrained in-sleep cardiorespiratory monitoring,” J. Intell. Mater. Syst. Struct. 14(3), 185-190 (2003).

[32] X. Zhu, W. Chen, T. Nemoto, Y. Kanemitsu, K. Kitamura, K. Yamakoshi, and D. Wei, “Real-time monitoring of respiration

rhythm and pulse rate during sleep," IEEE Trans. Biomed. Eng. 53(12), 2553-2563 (2006).

[33] J. Kortelainen, M. V. Gils, and J. Parkka, "Multichannel bed pressure sensor for sleep monitoring," in 2012 Computing in Cardiology, 313-316 (2012).

[34] M. Walter, B. Eilebrecht, T. Wartzek, and S. Leonhardt, "The smart car seat: Personalized monitoring of vital signs in automotive applications," Pers. Ubiquitous Comput. 15(7), 707-715 (2011).

[35] J. Alametsä, J. Viik, J. Alakare, A. Värri, and A. Palomäki, "Ballistocardiography in sitting and horizontal positions," Physiol. Meas. 29(9), 1071 (2008).

[36] K. C. Kao and G. A. Hockham, "Dielectric-fibre surface waveguides for optical frequencies," Proceedings of the Institution of Electrical Engineers 113, 1151-1158 (1966).

[37] N. Bai, E. Ip, Y.-K. Huang, E. Mateo, F. Yaman, M.-J. Li, S. Bickham, S. Ten, J. Liñares, C. Montero, V. Moreno, X. Prieto, V. Tse, K. Man Chung, A. P. T. Lau, H.-Y. Tam, C. Lu, Y. Luo, G.-D. Peng, G. Li, and T. Wang, "Mode-division multiplexed transmission with inline few-mode fiber amplifier," Optics Express 20, 2668 (2012)

[38] A. Mecozzi, C. Antonelli, and M. Shtaif, "Nonlinear propagation in multi-mode fibers in the strong coupling regime," Opt. Express, 20(11), 11673-11678 (2012).

[39] S. Inao, T. Sato, S. Sentsui, T. Kuroha, and Y. Nishimura, “Multicore optical fiber,” in Optical Fiber Communication Conference (OFC), WB1 (1979).

[40] T. A Birks, J. C. Knight, and P. S. J. Russell, “Endlessly single-mode photonic crystal fiber,” Opt. Lett., 22(13), 961-963 (1997).

[41] J. M. López-Higuera and L. R. Cobo, A. Q. Incera, and A. Cobo, “Fiber Optic Sensors in Structural Health Monitoring,” J. Light. Technol. 29(4), 587-608 (2011).

[42] N. Zeng, C. Z. Shi, M. Zhang, L. W. Wang, Y. B. Liao, and S. R. Lai, “A 3-component fiber-optic accelerometer for well logging,” Opt. Commun., 234, 153-162 (2004).

[43] S. Šprager, D. Donlagić, and D. Zazula, “Monitoring of basic human vital functions using optical interferometer,” in IEEE 10th International conference signal processing proceedings, 1738-1741 (2010).

[44] L. Duan, P. Zhang, M. Tang, R. Wang, Z. Zhao, S. Fu, L. Gan, B. Zhu, W. Tong, D. Liu, and P. P. Shum, “Heterogeneous all-solid multicore fiber based multipath Michelson interferometer for high temperature sensing,” Opt. Express, 24(18), 20210-20218 (2016).

[45] L. Dziuda, M. Krej, and F. W. Skibniewski, “Fiber Bragg Grating Strain Sensor Incorporated to Monitor Patient Vital Signs During MRI,” IEEE Sens. J. 13(12), 4986-4991 (2013).

[46] S. K. Yao and C. K. Asawa, “Fiber optical intensity sensors”, IEEE J. Sel. Areas Commun. 1(3), 562-575 (1983).

[47] N. Lagakos, J. H. Cole, and J. A. Bucaro, “Microbend fiber-optic sensor,” Appl. Opt. 26(11), 2171-2180 (1987).

[48] H. Golnabi, “Design and operation of a fiber optic sensor for liquid level detection,” Opt. Lasers Eng. 41(5), 801-812 (2004).

[49] Y. Zhu, Z. Huang, F. Shen, and A. Wang, “Sapphire-fiber-based white-light interferometric sensor for high-temperature measurements,” Opt. Lett. 30(7), 711-713 (2005).

[50] J. Jung, H. Nam, B. Lee, J. O. Byun, and N. S. Kim, “Fiber Bragg grating temperature sensor with controllable sensitivity,” Appl. Opt. 38(13), 2752-2754 (1999).

[51] M. Imai, T. Ohashi, and Y. Ohtsuka, “Fiber-optic Michelson interferometer using an optical power divider,” Opt. Lett. 5(10), 418-420 (1980).

[52] G. B. Hocker, “Fiber-optic sensing of pressure and temperature,” Appl. Opt. 18(9), 1445-1448 (1979).

[53] T. Yoshino, K. Kurosawa, K. Itoh, and T. Ose, “Fiberr-Optic Fabry-Perot Interferometer and Its Sensor Applications,” IEEE J. Quantum Electron. 18(10), 1624-1633 (1982).

[54] W.S. McCulloch and W. Pitts, “A logical calculus of the ideas immanent in nervous activity,” Bull. Math. Biol. 5(4), 115-137 (1943).

[55] F. Rosenblatt, “Principles of Neurodynamics: Perceptrons and the Theory of Brain Mechanisms,” New York: Spartan Books, (1962).

[56] D. E. Rumelhart, G. E. Hinton, and J. L. McClelland, “A general framework for parallel distributed processing,” Parallel distributed processing: Explorations in the microstructure of cognition, 1, 45-76 (1986).

[57] G. E. Hinton, S. Osindero, and Y. W, “Teh. A fast learning algorithm for deep belief nets,” Neural Comput. 18(7), 1527-1554 (2006).

[58] X. Glorot, A. Bordes, and Y. Bengio, “Deep sparse rectifier neural networks,” in Proceedings of the fourteenth international conference on artificial intelligence and statistics, 315-323 (2011).

[59] A. Krizhevsky, I. Sutskever, and, G. E. Hinton, “Imagenet classification with deep convolutional neural networks,” in Advances in neural information processing systems, 25 (2012).

[60] Y. LeCun, B. Boser, J. S. Denker, D. Henderson, R. E. Howard, W. Hubbard, and L. D. Jackel, “Backpropagation applied to handwritten zip code recognition. Neural computation,” 1(4), 541-551 (1989).

[61] Y. LeCun, L. Bottou, Y. Bengio, and P. Haffner, “Gradient-based learning applied to document recognition,” Proc. IEEE, 86(11), 2278-2324 (1998).

[62] D. Wang, X. Wang, and S. Lv, “An overview of end-to-end automatic speech recognition,” Symmetry, 11(8), 1018 (2019).

[63] S. Yang, Y. Wang, and X. Chu, “A survey of deep learning techniques for neural machine translation,” arXiv, 2002.07526 (2020).

[64] M. Qi, J. Qin, A. Li, Y. Wang, J. Luo, and L. V. Gool, “stagnet: An attentive semantic rnn for group activity recognition,” in Proceedings of the European Conference on Computer Vision (ECCV), 101-117 (2018).

[65] A. Y. Hannun, P. Rajpurkar, M. Haghpanahi, G. H. Tison, C. Bourn, M. P. Turakhia, and A. Y. Ng, “Cardiologist-level arrhythmia detection and classification in ambulatory electrocardiograms using a deep neural network,” Nat. Med. 25(1), 65-69 (2019).

[66] S. S. Xu, M. W. Mak, and C. C. Cheung, “Towards end-to-end ECG classification with raw signal extraction and deep neural networks,” IEEE J. Biomed. Health Inform. 23(4), 1574-1584 (2018).

[67] J. V. Rundo, and R. Downey III, “Polysomnography. Handbook of clinical neurology,” 160, 381-392 (2019).

[68] O. Yildirim, U. B. Baloglu, and U. R. Acharya, “A deep learning model for automated sleep stages classification using PSG signals,” Int. J. Environ. Res. Public Health, 16(4), 599 (2019).

[69] Q. Li, Q. Li, C. Liu, S. P. Shashikumar, S. Nemati, and G. D. Clifford, “Deep learning in the cross-time frequency domain for sleep staging from a single-lead electrocardiogram,” Physiol. Meas. 39(12), 124005 (2018).

[70] U. R. Acharya, S. L. Oh, Y. Hagiwara, J. H. Tan, H. Adeli, and D. P. Subha, “Automated EEG-based screening of depression using deep convolutional neural network,” Comput. Methods Programs Biomed. 161, 103-113 (2018).

[71] Y. Mohan, S. S. Chee, D. K. P. Xin, and L. P. Foong, “Artificial neural network for classification of depressive and normal in EEG,” in 2016 IEEE EMBS conference on biomedical engineering and sciences (IECBES), 286-290 (2016).

[72] Z. Chen, J. Hu, and C. Yu, “Fiber senor for long-range and biomedical measurements,” in 2013 12th International Conference on Optical Communications and Networks (ICOCN), 1-4 (2013).

[73] C. Yu, W. Xu, N. Zhang, and C. Yu, “Non-invasive smart health monitoring system based on optical fiber interferometers,” in International Conference on Optical Communications and Networks (ICOCN), 1-3 (2017).

[74] F. Tan, S. Chen, W. Lyu, Z. Liu, C. Yu, C. Lu, and H. Y. Tam, “Non-invasive human vital signs monitoring based on twin-core optical fiber sensors,” Biomed. Opt. Express, 10(11), 5940-5952 (2019).

[75] S. Chen, Z. Huang, F. Tan, T. Yang, J. Tu, and C. Yu, “Non-invasive smart monitoring system based on multi-core fiber optic interferometers,” in 2018 Asia Communications and Photonics Conference (ACP), 1-3, (2018).

[76] S. Sprager, and D. Zazula, “Detection of heartbeat and respiration from optical interferometric signal by using wavelet transform,” Comput. Methods Programs Biomed. 111(1), 41-51 (2013).

[77] J. Qu, Y. Shen, W. Xu, F. Tan, C. Yu, and C. Yu, “Non-invasive Vital Signs Monitoring Based on Polarization Maintaining Fiber and

Sagnac Interferometer", in OptoElectronics and Communications Conference (OECC), 8817846 (2019).

[78] S. Chen, Z. Huang, F. Tan, T. Yang, J. Tu, and C. Yu, "Vital signs monitoring using Few-mode fiber-based sensors," in 2018 Photonics Asia, 1-7 (2018).

[79] F. Tan, W. Lyu, S. Chen, Z. Liu, and C. Yu, "Contactless vital signs monitoring based on few-mode and multi-core fibers," Opto-Electron. Adv. 3(5), 05190034 (2020).

[80] W. Lyu, W. Xu, F. Yang, S. Chen, F. Tan, and C. Yu, "Non-invasive Measurement for Cardiac Variations Using a Fiber Optic Sensor," IEEE Photon. Technol. Lett. 33(18), 990-993 (2021).

[81] F. Yang F, W. Lyu, C. Pan, S. Yan, F. Tan, S. Chen, and C. Yu, "Contactless vital signs monitoring based on optical fiber Mach-Zehnder interferometer aided with passive homodyne demodulation methods," in Asia Communications and Photonics Conference (ACP), M4A. 79 (2020).

[82] A. Dandridge, A. B. Tveten, and T. G. Giallorenzi, "Homodyne Demodulation Scheme for Fiber Optic Sensors Using Phase Generated Carrier," IEEE Trans. Microw. Theory Tech. 30, 1635 (1982).

[83] K. H. Ang, G. Chong and Y. Li, "PID control system analysis, design, and technology," IEEE Trans. Control Syst. Technol. 13(4), 559-576 (2005).

[84] J. H. Shin, B. H. Choi, Y. G. Lim, D. U. Jeong, and K. S. Park, "Automatic ballistocardiogram (BCG) beat detection using a template matching approach," in 2008 30th Annual International Conference of the IEEE Engineering in Medicine and Biology Society, 1144-1146 (2008).

[85] S.-T. Choe, and W.-D. Cho, "Simplified real-time heartbeat detection in ballistocardiography using a dispersion-maximum method," Biomed. Res. 28(9), (2017).

[86] C. Brüser, K. Stadlthanner, S. D. Waele, and S. Leonhardt, "Adaptive Beat-to-Beat Heart Rate Estimation in Ballistocardiograms," IEEE Trans. Inform. Technol. Biomed. 15(5), 778-786 (2011).

[87] C. Brüser, M. D. H. Zink, S. Winter, P. Schauerte, and S. Leonhardt, "A feasibility study on the automatic detection of atrial fibrillation using an unobtrusive bed-mounted sensor," in 2011 Computing in Cardiology, 13-16 (2011).

[88] H. Lu, H. Zhang, Z. Lin, and N. S. Huat, (2018, July). "A Novel Deep Learning based Neural Network for Heartbeat Detection in Ballistocardiograph," In 40th Annual International Conference of the IEEE Engineering in Medicine and Biology Society (EMBC), 2563-2566 (2018).

[89] Y. Wei, W. Xia, M. Lin, J. Huang, B. Ni, J. Dong, Y. Zhao, and S. Yan, "HCP: A Flexible CNN Framework for Multi-Label Image

Classification," IEEE Trans. Pattern Anal. Mach. Intell. 38(9), 1901-1907 (2016).

[90] X. Fu, J. Huang, X. Ding, Y. Liao, and J. Paisley, "Clearing the Skies: A Deep Network Architecture for Single-Image Rain Removal," IEEE Trans. Image Process. 26(6), 2944-2956 (2017).

[91] S.Whiting, S. Moreland, J. Costello, G. Colopy, and C. McCann, "Recognising Cardiac Abnormalities in Wearable Device Photoplethysmography (PPG) with Deep Learning," arXiv, 1807.04077 (2018).

[92] M. Kachuee, S. Fazeli and M. Sarrafzadeh, "ECG Heartbeat Classification: A Deep Transferable Representation," in 2018 IEEE International Conference on Healthcare Informatics (ICHI), 443-444 (2018).

[93] M. Lin, Q. Chen, and S. Yan, "Network in network," arXiv, 1312.4400 (2013).

[94] D. P. Kingma, and J. Ba, "Adam: A method for stochastic optimization," arXiv, 1412.6980 (2014).

[95] O. Ronneberger, P. Fischer, and T. Brox, "U-Net: Convolutional Networks for Biomedical Image Segmentation," arXiv, In International Conference on Medical image computing and computer-assisted intervention, 234-241 (2015).

[96] E. Shelhamer, J. Long, and T. Darrell, "Fully Convolutional Networks for Semantic Segmentation," IEEE Trans. on Pattern Anal. Mach. Intell. 39(4), 640-651 (2017).

[97] S. Chen, F. Tan, W. Lyu, and C. Yu, “Ballistocardiography monitoring system based on optical fiber interferometer aided with heartbeat segmentation algorithm,” Biomed. Opt. Express 11(10), 5458-5469, (2020).

[98] W. Rawat, and Z. Wang, Z, “Deep convolutional neural networks for image classification: A comprehensive review,” Neural Comput. 29(9), 2352-2449 (2017).

[99] Q. Wang, Y. Zhang, G. Chen, Z. Chen, and H. I. Hee, “Assessment of heart rate and respiratory rate for perioperative infants based on ELC model,” IEEE Sens. J. 21(12), 13685-13694 (2021).

[100] S. Tahir, I. Sadek, and B. Abdulrazak, “A CNN-ELM-Based Method for Ballistocardiogram Classification in a Clinical Environment,” in 2021 IEEE Canadian Conference on Electrical and Computer Engineering (CCECE), 1-6 (2021).

[101] C. Zhu, E. A. Chan, Y. Wang, W. Peng, R. Guo, B. Zhang, C. Soci, and Y. Chong, “Image reconstruction through a multimode fiber with a simple neural network architecture,” Sci. Rep. 11(1), 1-10, (2021).

[102] N. Borhani, E. Kakkava, C. Moser, and D. Psaltis, “Learning to see through multimode fibers,” Optica, 5(8), 960-966 (2018).

[103] Z. Yu, Z. Ju, X. Zhang, Z. Meng, F. Yin, and K. Xu, “High-speed multimode fiber imaging system based on conditional generative adversarial network,” Chin. Opt. Lett. 19(8), 081101 (2021).

[104] Y. An, L. Huang, J. Li, J. Leng, L. Yang, and P. Zhou, “Learning to decompose the modes in few-mode fibers with deep convolutional neural network,” Opt. Express, 27(7), 10127-10137 (2019).

[105] S. Rothe, Q. Zhang, N. Koukourakis, and J. Czarske, “Intensity-only mode decomposition on multimode fibers using a densely connected convolutional network,” J. Light. Technol. 39(6), 1672-1679 (2021).

[106] S. Rothe, Q. Zhang, N. Koukourakis, and J. W. Czarske, “Deep learning for computational mode decomposition in optical fibers,” Appl. Sci., 10(4), 1367. (2020).

[107] I. J. Goodfellow, J. Pouget-Abadie, M. Mirza, B. Xu, D. Warde-Farley, S. Ozairy, A. Courville, and Y. Bengio, “Generative Adversarial Nets,” arXiv, 1406.2661 (2014).

[108] P. Isola, J.-Y. Zhu, T. Zhou, and A. A. Efros, “Image-to-Image Translation with Conditional Adversarial Networks,” in 2017 Proceedings of the IEEE conference on computer vision and pattern recognition, 1125-1134 (2017).

[109] M. Mirza, and S. Osindero, “Conditional Generative Adversarial Nets,” arXiv, 1411.1784 (2014).

[110] B. Xu, N. Wang, T. Chen, and M. Li, “Empirical evaluation of rectified activations in convolutional network,” arXiv, 1505.00853 (2015).

[111] J. Lee, K. Oh, B. Kim, and, S. K. Yoo, “Synthesis of electrocardiogram V-lead signals from limb-lead measurement

using R-peak aligned generative adversarial network," IEEE J. Biomed. Health Inform. 24(5), 1265-1275 (2019).

[112] G. G. Berntson, J. T. Cacioppo, and K. S. Quigley, "Respiratory sinus arrhythmia: autonomic origins, physiological mechanisms, and psychophysiological implications," Psychophysiology, 30(2), 183-196 (1993).

[113] J. Sztajzel, "Heart rate variability: a noninvasive electrocardiographic method to measure the autonomic nervous system," Swiss Med. Wkly. 134(35-36), 514-522 (2004).

[114] A. J. Camm, M. Malik, J. T. Bigger, G. Breithardt, S. Cerutti, R. J. Cohen, P. Coumel, E. L. Fallen, H. L. Kennedy, R. E. Kleiger, L. Federico, M. Alberto, A. J. Moss, J. N. Rottman, G. Schmidt, P. J. Schwartz, and D. H. Singer, "Heart rate variability. Standards of measurement, physiological interpretation, and clinical use. Task Force of the European Society of Cardiology and the North American Society of Pacing and electrophysiology," Eur. Heart J. 17(3), 354–381 (1996).

[115] M. Javorka, I. Zila, T. Balhárek, and K. Javorka, "Heart rate recovery after exercise: relations to heart rate variability and complexity. Brazilian Journal of Medical and Biological Research," 35(8), 991-1000 (2002).

[116] D. L. Donoho, "Compressed sensing," IEEE Trans. Inf. Theory, 52(4), 1289–1306 (2006).

[117] J. Xiao, F. Hu, Q. Shao, and S. Li, “A low-complexity compressed sensing reconstruction method for heart signal biometric recognition,” Sensors, 19(23), 5330 (2019).

[118] J. Chen, S. Sun, L. B. Zhang, B. Yang, and W. Wang, “Compressed sensing framework for heart sound acquisition in internet of medical things,” IEEE Trans. Industr. Inform. 18(3), 2000-2009 (2021).

[119] E. C. Marques, N. Maciel, L. Naviner, H. Cai, and J. Yang, “A review of sparse recovery algorithms,” IEEE access, 7, 1300-1322 (2018).

[120] B. Liu, Z. Zhang, G. Xu, H. Fan, and Q. Fu, “Energy efficient telemonitoring of physiological signals via compressed sensing: A fast algorithm and power consumption evaluation,” Biomed. Signal Process Control, 11, 80-88 (2014).

[121] H. Zhang, Z. Dong, Z. Wang, L. Guo, and Z. Wang, “CSNet: A deep learning approach for ECG compressed sensing,” Biomed. Signal Process Control, 70, 103065 (2021).

[122] R. Liu, M. Shu, and C. Chen, “ECG signal denoising and reconstruction based on basis pursuit,” Appl. Sci. 11(4), 1591 (2021).

[123] J. A. Tropp, and A. C. Gilbert, “Signal recovery from random measurements via orthogonal matching pursuit,” IEEE Trans. Inf. Theory, 53(12), 4655-4666 (2007).

[124] M. E. Tipping, “Sparse Bayesian learning and the relevance vector machine,” J. Mach. Learn. Res., 1, 211–244 2001.

[125] Z. Zhang, and B. D. Rao, “Extension of SBL algorithms for the recovery of block sparse signals with intra-block correlation,” IEEE Trans. Signal Process. 61(8), 2009-2015 (2013).

[126] Z. Zhang, T. P. Jung, S. Makeig, and B. D. Rao, “Compressed sensing for energy-efficient wireless telemonitoring of noninvasive fetal ECG via block sparse Bayesian learning,” IEEE. Trans. Biomed. Eng. 60(2), 300-309 (2012).